Delft Cold Neutron Source Flow Modeling

A flow simulation study for the Cold Neutron Source to be built at the Reactor Institute Delft, using the commercially available code ANSYS Fluent.

A.J. de Blécourt

RID, July 2015

In partial fulfillment of the requirements for the degree of

Bachelor of Science
in Applied Physics

At Delft University of Technology

Supervisor
Dr. M. Rohde

Thesis Committee
Dr. ir. M. Rohde
Prof. dr. ir. C. R. Kleijn

Delft University of Technology
Faculty of Applied Sciences

Abstract

The HOR (Hoger Onderwijs Reactor or Higher Education Reactor) at the Reactor Institute Delft (RID) is used primarily as a source of neutrons, which in turn are used in scattering and attenuation experiments. These neutrons are relatively high in energy and the energies of the neutrons have a relatively broad spectrum. The neutrons are to be cooled by moderation by hydrogen in a so-called cold neutron source, in order to narrow the spectrum and lower the energy. This achieves a higher accuracy in the experiments conducted using the neutrons.

The RID issued a worldwide tender for the design of a cold neutron source, to which by the KHC consortium –a consortium of Hyundai and the Korean Atomic Energy Research institute- has responded with a design. The design proposed by KHC involves a natural convection driven loop of saturated hydrogen. The flow patterns in the moderator cell are poorly known but they are of great importance, since mainly the void fraction will negatively affect the moderation of the neutrons. This thesis focuses on modeling the flow inside the vessel.

Using ANSYS Fluent, the flow was modeled for a range of inlet conditions and mass flows. Velocity plots are used to investigate the flow in more detail. The void fraction dependence on the mass flow rate and other model parameters is determined.

Fairly simple models are used in combination with a relatively coarse mesh, therefore the results obtained should not be interpreted as highly accurate but as a first insight in the flow and the processes of influence.

The average void fraction in the moderator cell turns out to be quite high at 79% in the specified design, which has a hydrogen mass flow rate of 2 g/s. Increasing the mass flow rate shows to greatly reduce the average void fraction to 53% at triple the design flow rate.

Some parameters of influence are still unknown, making an experimental study highly recommended. The model used to simulate mass transfer needs an unknown input parameter specifying the fraction of vapor molecules hitting the bubble surface that is absorbed into the liquid, called the attenuation coefficient, which manifests in the evaporation and condensation frequencies *K*. Varying this parameter shows to influence the void fraction significantly, where values between 67% and 93% are obtained for values between 0.01 and 10. Because of the large range of possible values of *K*, further research in determining the value of this parameter is recommended in order to increase the accuracy of simulations using this model.

Table of Contents

1 Introduction

This thesis is aimed at gaining a better understanding of the flow in the cold neutron source that is to be built at the facility of the Reactor Institute Delft (RID). RID has issued a worldwide tender, to which a consortium of the Korean Atomic Energy Research Institute (KAERI) and Hyundai, the KAERI Hyundai Consortium (KHC), has responded with a design including a two phase hydrogen loop. Making use of Computational Fluid Dynamics (CFD) in the form of the commercially available code ANSYS Fluent, the flow is modeled to investigate the velocity field and the void fraction distribution. The latter property of the flow is of great importance, because RID is concerned that it may rise to high levels in certain areas, decreasing neutron moderation. Thus, finding the void fraction distribution in the moderator cell is the main objective in this thesis.

1.1 The OYSTER Project

The reactor at TU Delft is the only academic research reactor in the Netherlands. The main purpose of the reactor is to produce neutrons, which is why the thermal output is relatively low when compared to commercial reactors (2 MW instead of about 1.4 GW at the Borssele nuclear power station [1]). The neutrons are used in scattering experiments in the experimental hall adjacent to the reactor building, while samples can also be irradiated by placing them inside the reactor basin near the core through a dedicated system of feed tubes. Figure 1.1 shows the reactor hall (right) and the adjacent experimental hall (left) [2]. The image shows the reactor basin inside the reactor hall, as well as the beam tubes going from the reactor core to the experimental hall. The chimney is part of the reactor hall ventilation system.

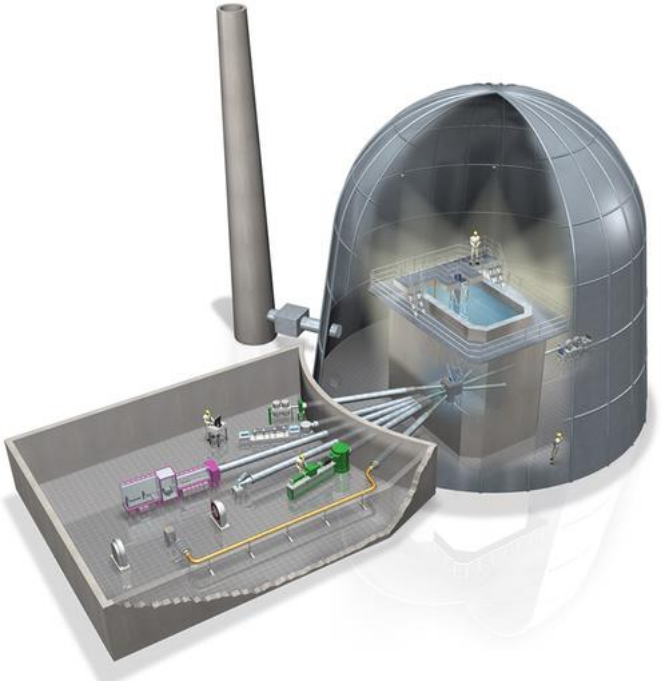

Figure 1.1: reactor hall with adjacent experimental hall

The OYSTER project (Optimized Yield for Science, Technology, and Education of Radiation) is aimed at increasing the scientific capability of the RID. This will be achieved by implementing a cold neutron source and adding new measurement instruments. The option of increasing the thermal power to 3 MW is being investigated as well, as this will increase the total neutron production. With all

measures combined, RID will be able to perform a 100 times more measurements or a 100 times more accurate measurements than is currently possible in a given timeframe [3].

1.2 Cold Neutrons

Neutrons produced in fission reactions have a broad spectrum of energies. Through collisions with core materials and coolant, they reach thermal equilibrium with the moderator material. In the most common type of nuclear reactors, this is the coolant as well. This is the case at RID, where water is used. The result of this moderation is that the peak in the neutron energy spectrum shifts to the energy which corresponds to the water temperature, which is roughly 40°C. The neutron temperature is a measure of the neutron velocity. In equations, this is formulated as follows

$$E = \frac{1}{2} m v^2 = \frac{3}{2} k_B T \tag{1.1}$$

where E denotes the average neutron energy, m the neutron mass, v the most probable neutron velocity, k_B the Boltzmann constant and T the neutron temperature. Here, the neutrons are considered an ideal monatomic gas. From the formula, it becomes evident that lowering the neutron energy implies lowering the speed and the temperature. Using a neutron mass of 1.675E-27 kg and a value of 1.381E-23 J/K for the Boltzmann's constant k_B [4] gives a velocity v of about 2.8 km/s at 313 K (40°C). Note that, in general, neutrons do not all have the same energy, but a whole spectrum of neutron energies is present; equation 1.1 relates the average neutron temperature to the average kinetic energy of the neutrons.

Thermal energy is usually determined by the average kinetic energy of randomly moving particles. In the case of neutron beams, however, the particles are not moving randomly but more or less in the same direction. Neutrons are difficult to steer in beams, because they have no electric charge like positrons or electrons, and cannot be focused by regular lenses like photons. They are also difficult to detect, because they interact only with the nuclei rather than with the electron shell, again because of the absence of charge.

Neutrons are transported in neutron guides, which are hollow tubes with their inside surface coated with a material that reflects neutrons. Sending neutrons through such a tube confines them to the inside of this tube if they are reflected or absorbed whenever they reach the tubes inner surface. Neutrons that are not absorbed are transported through the tube via a series of reflections off the tube walls.

Slow or 'cold' neutrons are easier to steer, which manifests in the critical angle. This is the minimal angle of incidence at which neutrons are totally reflected without being absorbed, where the angle of incidence is the angle between the normal of the surface and the velocity vector of the incoming neutron. It can be shown that the critical angle decreases as the neutron wavelength increases [5, 6]. This makes it possible to make the bends in a neutron guide sharper for neutrons of larger wavelength without losing too many neutrons as a result of absorption in the neutron guide due to an angle of incidence that is smaller than the critical angle. Please note that in this context, the glancing angle or grazing angle is often used instead of the angle of incidence; it is the complement to the angle of incidence and therefore it decreases whenever the angle of incidence increases and vice versa. Thus, the angle of incidence equals 90° minus the glancing angle.

Cold neutrons are also easier to detect, because most materials interact more readily with slow moving neutrons than with fast ones. This manifests in a larger neutron cross section σ; for every kind of reaction, neutron energy and nucleus type, σ may vary. Equation 1.2 shows how the cross section σ influences the interaction rate R, which is the number of neutron-nucleus interactions per unit volume and time. N denotes the number density of the nuclei while $v(\mathbf{r})$ is the velocity of the neutrons and $n(\mathbf{r})$ is the number density of the neutrons, both as a function of position. [7]

$$R = \sigma N v(\mathrm{r}) n(\mathrm{r}) \tag{1.2}$$

A higher interaction rate also means one needs less neutrons to perform a given measurement, enabling more (or more precise) measurements in a given timeframe with the same amount of neutrons. Furthermore, because slower neutrons have a larger wavelength, they are more suitable for investigating larger structures. The wavelength is given by the de Broglie relation [7]

$$\lambda = \frac{h}{mv} \tag{1.3}$$

where h is Planck's constant and λ is the neutron wavelength. Using a velocity of 2.8 km/s, as was calculated from equation 1.1, and h=6.626E-34 Js [4], the neutron wavelength is 1.4 Å at 40°C, which is on the order of magnitude of the spacing between atoms. Lowering the neutron temperature by a factor 12 to 26 K instead of 313 K (40°C) decreases neutron speed by a factor of √12 through equation 1.1. Equation 1.3 shows that this increases the neutron wavelength by a factor of √12, which is about 3.5. The neutron wavelength at 26 K will therefore be 4.9 Å at 26 K.

To cool down the thermal neutrons coming from the reactor, a cold medium can be placed between the reactor and the beam tube. The neutrons will move through the cold medium, collide with the nuclei and transfer energy. The energy of the neutrons will decrease, whereas the energy of the medium's particles will increase. In short, the neutrons will cool down and the medium will heat up. The assembly used for cooling down the neutrons is called a cold neutron source (CNS), even though the physical source of the neutrons is the reactor core while the CNS is merely the apparatus that cools them down.

1.3 Cold Neutron Sources

Cold neutron sources require that the neutrons interact readily with the medium nuclei, without being absorbed too much. In other words, the scattering cross section must be large, whereas the absorption cross-section must be small. Furthermore, the mass of the nuclei should be as close to the mass of the neutrons as possible, in order to reach maximum momentum transfer. This means the nuclei should be as light as possible. Because of this, hydrogen or deuterium are probable choices as a moderator material. While deuterium has a lower absorption cross section, hydrogen is lighter and therefore requires less collisions with the neutrons to slow them down. Furthermore, hydrogen has a much better availability than deuterium, which is the most important reason to choose hydrogen in most practical applications. Hydrogen is used in the design for the CNS at the subject of this thesis.

The hydrogen flows into a moderator cell, where the neutrons move through it, depositing energy. The heated hydrogen is then removed from the moderator cell, cooled down in a heat exchanger, and fed back into the moderator cell. Typical hydrogen temperatures range from 20K to 30K. When it is assumed that the moderator is big enough in order for the neutrons achieve near thermal

equilibrium with the moderator material, the neutron speed reduces to about 550 meters per second. Since this is a factor 4 decrease in velocity when compared to thermal neutrons, the energy is decreased by a factor 4^2=16. Since the most probable neutron speed is a factor 4 smaller, the most probable wavelength is a factor 4 larger for cold neutrons.

1.4 Two Phase versus Supercritical

The hydrogen is supplied to the moderator cell in the liquid or supercritical phase. If it starts to boil inside the moderator cell by heat transfer from neutrons, it is called a two phase hydrogen loop, since two phases, i.e. gas and liquid, are present. If it remains liquid in the entire system, it is a single phase liquid hydrogen loop. A system where the hydrogen is supercritical throughout the system, i.e. above it's critical temperature and pressure, is called a supercritical hydrogen loop. The critical conditions for hydrogen are a temperature of 33.3 K and a pressure of 12.8 atm. [9]. A disadvantage of a supercritical system is that the critical pressure is quite high, which requires a very strong hydrogen containment vessel.

1.4.1Two Phase

The two phase system has the advantage that a lot of heat can be removed by the evaporation alone; the evaporation enthalpy is a factor 41 larger than the enthalpy change liquid hydrogen liquid hydrogen experiences when heating up by 1 K [2]. This implies that relatively small temperature gradients of the hydrogen suffice to remove the heat from the moderator cell, decreasing thermal stress on the moderator cell material.

The downside is, however, that because of the presence of gas in the moderator cell, the hydrogen density varies sharply as a function of the void fraction, which is the fraction of the volume that is occupied by gaseous hydrogen. The moderation depends strongly on the density, since less nuclei present means less interaction of neutrons with nuclei, which results in less moderation and cooling of the neutrons. The result can be a spatially and temporally highly inhomogeneous neutron moderation, if the void fraction varies locally and temporally. Temporal variation could occur if, for instance, large bubbles form which migrate through the moderator cell.

1.4.2 Supercritical

This is where the supercritical system comes in, because there are no gas bubbles present in the moderator cell, resulting in a much smoother density profile. The density dependence on the temperature highly depends on the temperature for supercritical fluids; if the fluid is close to the critical conditions, the density varies sharply when the temperature is changed, while it changes less with temperature at conditions further from the critical point. The density never varies as much with temperature as in a saturated system, however, because a clear phase transition is absent in supercritical fluids.

Even though there is no sharp phase transition in supercritical fluids, there is a peak in the heat capacity at the temperature where one would expect a phase change in normal liquids/gases. This peak becomes less sharp and broader as the system is taken further above critical conditions.

The temperature dependence of the thermal expansion coefficient allows one to tune the fluid to suit one's needs; if the fluid is kept close to the critical point, the density and heat capacity profiles resemble those of a saturated gas/liquid mixture, giving a high sensitivity to temperature changes, providing the system with a highly self-regulating behavior. The mechanism here is that a rise in

temperature causes a density drop, which induces a decrease in moderation, since there are less hydrogen cores present in a given volume for the neutrons to collide with. This decreases the heat source, countering the temperature rise that caused the decrease in density in the first place. Moving the operating conditions further from the critical point decreases this effect.

1.5 Thermosiphon versus Forced Convection

The hydrogen flow can be driven by two mechanisms: one is a forced convection loop, with a pump to force the hydrogen flow, the other is a natural convection loop, where the flow is driven by density differences induced by heating of the hydrogen.

The advantage of the natural circulation system is that there is no need for a pump, which reduces the costs and maintenance downtime of the system significantly. However, in the forced convection system, the pump can be used to regulate the flow, making the system easier to control. Also, employing a natural circulation loop places some constraints on the design; the height difference must be sufficient to provide adequate natural circulation, and the overall flow resistance cannot be too high, for otherwise the flow would not be sufficient to remove the heat from the moderator cell at the desired operating conditions (void fraction, hydrogen temperature and pressure). The design process itself is more complicated as well, because detailed flow calculations and simulations have to be performed to ensure that the circulation is sufficient.

1.6 Goal and Outline

1.6.1 Goal

The main goal of this thesis is to find the void fraction distribution inside the moderator cell as designed by KHC. A better understanding of the flow field is achieved by starting with single phase simulations and by investigating the velocity field.

1.6.2 Outline

A single phase system is investigated to gain a first insight in the flow. Simulations are performed for various stages of the KHC design, for various flow conditions (section 4.1). The velocity characteristics are investigated in more detail (section 5.1.2). The two phase system is investigated for the most advanced design only, where the velocity characteristics are again investigated (section 5.2.1). Here, the influence of the mass flow rate on the void fraction distribution is also investigated (section 5.2.2), as well as the influence of the attenuation coefficient (section 5.2.3), which is the fraction of vapor molecules reaching the bubble surface that are absorbed into the liquid. In the models used, this parameter manifests as the evaporation/condensation frequency, which is further elaborated upon in section 4.2.2.

2 CNS Design Proposal

2.1 Moderator Cell Geometry

KHC (the Korean Atomic Energy Research Institute KAERI & Hyundai Consortium) has proposed a design for a cold neutron source to be built at the facility of the Reactor Institute Delft (RID). The design is for a natural convection two phase hydrogen system. The moderator cell consists of a cylindrical shell, with another, slightly smaller, shell placed inside it concentrically. Both shells have a closed off bottom, and since the inner shell has a smaller diameter and length than the outer one, there is a space between the shells. At the back of the cell (the front end is the reactor side, the back end is the beam tube side), both shells are placed against a common back plate. This configuration results in a cup shaped cavity in between the shells, in which the hydrogen will flow.

2.2 Operation Principles

Supply and removal of hydrogen to the moderator cell is done by a concentric pair of tubes, which is attached at the top of the moderator cell near the back end. The inner tube supplies liquid hydrogen, the outer tube removes a mixture of liquid and gaseous hydrogen. The inner tube is slightly longer, making it protrude into the cup shaped cavity (this protrusion does not show clearly in the figures in this chapter, since these are conceptual images rather than definitive design drawings). This allows the system to be started passively, without any pumps, as hydrogen expands as it heats up and tends to rise to the top of the cell, where it will preferably be removed by the outer tube, since its inlet is positioned higher than the outlet of the inner tube. A cross section of the cell is given in figure 2.1. A more elaborate depiction of the in pool assembly is shown in figure 2.3.

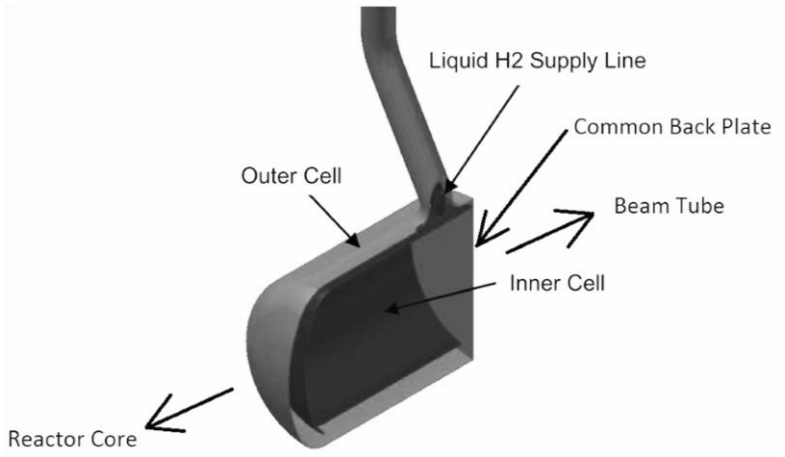

Figure 2.1: cross section of moderator cell design.

In the preliminary design, the inner shell was open at the bottom. This meant that the inner volume of the inner shell was also part of the flow domain (this is shown more clearly in figure 2.2). This has consequences for the system behavior, mainly during startup. When the system is still cold, the moderator cell is filled with liquid hydrogen. As the reactor is turned on, hydrogen starts to heat up and evaporate; the hydrogen heats up by a volumetric heat source consisting of the heat deposited by neutron moderation and by a surface heat source by heating of the moderator cell itself, mainly by gamma radiation energy being absorbed into the aluminum. Since the gaseous hydrogen inside the inner shell tends to rise but cannot rise any further once it has reached the top of this shell, gaseous hydrogen collects inside the inner shell. There will exist some level of liquid hydrogen inside

the inner shell, above which only gaseous hydrogen is present, at which the system stabilizes. This level will vary depending on reactor power and flow conditions and is believed to be a stabilizing factor.

A dynamic equilibrium will exist between gaseous hydrogen condensing along the inner side of the inner cell, and liquid hydrogen at the liquid hydrogen level evaporating inside the inner shell. A natural circulation of gas rising in the center and cooling down along the inner side of the inner shell will occur, since hydrogen gas is heated up by neutron moderation and cooled down by contact with the shell, which is in thermal contact with the saturated mixture in the cavity between the shells. A cross section of the cell is given in figure 2.2. the beryllium block is used to shield the moderator cell from the gamma radiation to some degree. This is done because the gamma radiation reaching the moderator cell deposits heat into the hydrogen, increasing the amount of heat to be removed from the cell, without contributing to the neutron flux in the output neutron beam.

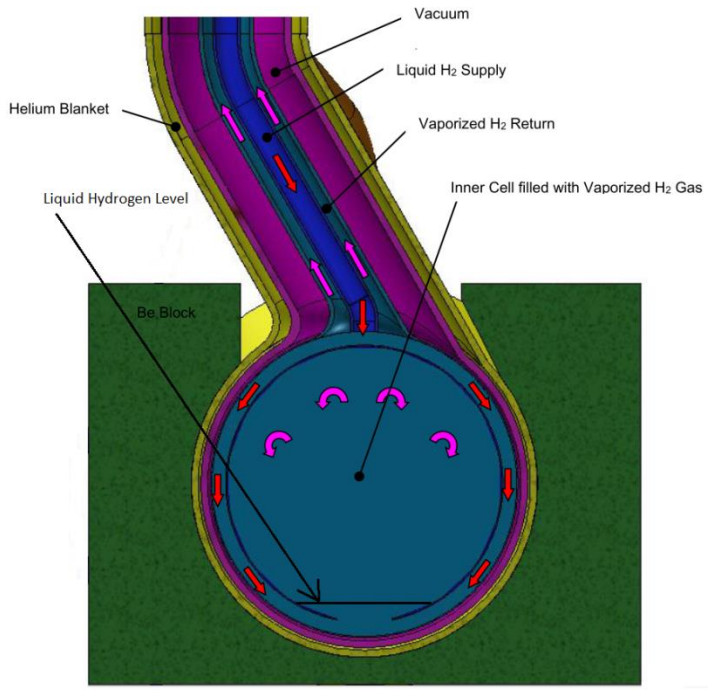

Figure 2.2: cross section of the preliminary design of the moderator cell, with open inner cavity. The helium containment vessel is colored yellow, the vacuum shell is purple, the outer moderator cell is light blue and the inner moderator cell is dark blue.

2.3 In-Pool Assembly

The moderator cell and hydrogen removal tube are encased in another shell with a vacuum layer in between, which in turn is encased in a helium layer with another shell encasing the whole system. These boundaries serve to ensure proper thermal insulation from the reactor coolant and the rest of the environment and as a hydrogen containment in the case of leaks of the moderator cell. They also protect the system from outside influences. The full in-pool assembly is shown in figure 2.3, clearly showing the opening in the inner cavity, the inner and outer tube for hydrogen supply and removal and the multiple boundary system. The water drain tube is used to drain the water from the cavity between the moderator cell and the neutron beam tube (the latter is not shown in the figure) after installation. The water that is initially in that cavity is reactor coolant water, which is enclosed in the

cavity upon installation because the reactor pool is full of water at the time of installation. As the water is drained, the cavity is filled with helium through the helium supply tube for the water drain. This helium is then removed by the vacuum pump. In stand-by mode, the moderator cell is filled with helium instead of hydrogen. This is what the helium gas supply tube is for. This mode of operation is not discussed further in this thesis.

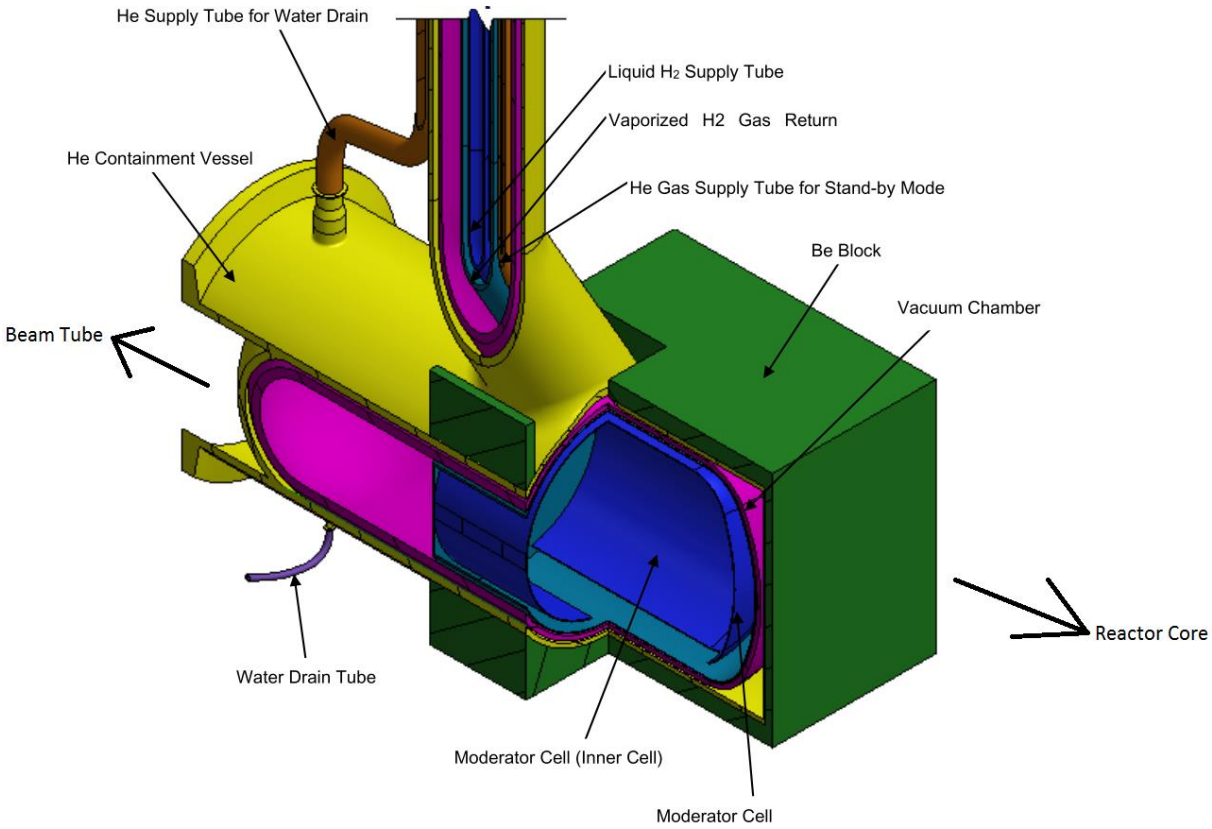

Figure 2.3: cutout vies of the bottom part of in the pool assembly. The moderator cell is shown in blue, the vacuum shell is shown in purple and the helium containment vessel is shown in yellow, as in figure 2.2.

The design is as of yet not definitive, so some lengths are not yet determined. An overview of spatial dimensions used in the calculations can be found in Appendix A. The system is designed to be at saturation condition at 1.5 bar, giving a saturation temperature of 21.7 K [9]. The mass flow specified by KHC is 2 g/s. This value and both figures in this chapter stem from the design proposal by KHC [10].

2.4 Advanced Design

KHC revised their design during the research period of this thesis, changing some spatial dimensions and later on fully closing the inner shell, making the inside vacuum. This substantially decreased the complexity of heat and material flows as well as startup behavior. However, no new estimates were done by KHC with regard to the mass flow and the heat load. Figure 2.4 shows the same view as figure 2.2, only with the inner cavity of the moderator cell evacuated. The open inner cavity is used in the single phase simulations, while the evacuated inner cavity is used in the two phase simulations. The switch to the advanced design is done because the design changed in the course of the thesis work.

It could be expected that the heat load would drop as the inner cavity is evacuated, since there is no more gaseous hydrogen present in this cavity to absorb heat. The natural circulation of this gas ,

depicted in figure 2.2, ceases, and the buffering effect of the variable liquid hydrogen level is lost as well. However, the inner moderator cell would have to be much stronger in order to withstand the pressure difference between the vacuum in the inner cavity and the hydrogen in the moderator cell which is at 1.5 bar. This would require a heavier inner moderator cell, which contains more aluminum, which therefore might absorb substantially more heat from gamma radiation, increasing the heat load on the hydrogen. The mounting points of the inner cell, which are not depicted in the figures nor concerned in the simulations performed in this thesis, would have to be stronger as well, possibly influencing the flow because they would be bulkier or more numerous.

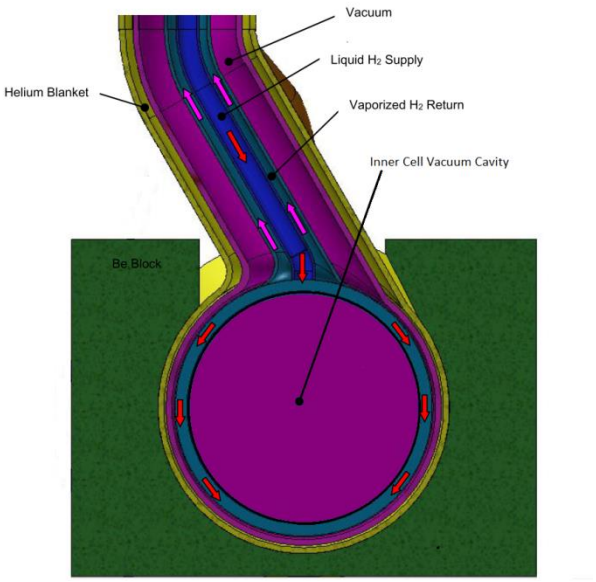

Figure 2.4: cross section of the advanced design of the moderator cell, with evacuated inner cavity

3 Simulation Preparations

Before starting a simulation, it is important to know what is to be calculated and what the relevant parameters are. In this thesis, the main objective is to find the void fraction distribution throughout the moderator cell. To achieve this, many parameters need to be calculated, in order to be able to specify the right conditions for the simulation. The Reynolds number, for example, governs the turbulence regime of the flow, while the pressure difference between inlet and outlet of the cell determines the driving force of the flow. The heat flow into the hydrogen consists of several components, which need to be specified as well.

3.1 Rough Calculations

As is the case with most CFD analyses, preliminary calculations have to be performed in order to gain a first insight in the flow. As computational resources are limited, it is also essential to know which parameters may be neglected in order to reduce the complexity of the simulation, lowering the computational effort without losing too much accuracy.

3.1.1 Reynolds Number

The Reynolds number is an important factor in flow calculations, since it determines whether a flow is turbulent or not and if it is, which flow regime is most likely. In general, the Reynolds number is defined as

$$\mathrm{Re} = \frac{\rho v_{average} D}{\mu} \tag{3.1}$$

Where ρ is the density of the medium, $v_{average}$ is the average velocity, D is a characteristic length and μ is the dynamic viscosity of the medium.

Inlet and Outlet Tubes

The Reynolds number in the inlet and outlet tubes is determined with the average velocity in the tube, which is obtained by dividing the mass flow (2 g/s as specified by KHC) by the surface area of the tube and the density of the medium, according to equation 3.2, φ_m is the mass flux, A_{tube} is the cross sectional surface area of the tube perpendicular to the flow and ρ_{H2} is the average hydrogen density in the tube.

$$v_{average} = \frac{\varphi_m}{A_{tube}\rho_{H2}} \tag{3.2}$$

In this case, the characteristic length D to be used in equation 3.1 is the hydraulic diameter, which is the inner tube diameter for the inlet tube and the difference between the inner and outer tube diameters for the outlet tube.

As a first estimate, 100% gas is assumed in the outlet tube, since gas rises to the top of the moderator cell, where it is removed from the moderator cell through the outlet tube. This gas is assumed to be fully condensed in the condenser, so 100% liquid is assumed in the inlet tube.

In reality, some gas from the moderator cell might enter the inlet tube, bubbling up against the downward stream of liquid hydrogen if the buoyancy force of the bubbles is strong enough to

overcome the drag force of the liquid hydrogen flowing downward. Also, if the phase separation in the moderator cell is not complete, some liquid hydrogen may be removed from the moderator cell through the outlet tube. The former effect would increase flow resistance in the inlet tube, as the rising bubbles experience drag from the surrounding liquid inlet flow. Both effects would decrease the driving force of the flow, as the density difference between the inlet tube (down comer) and outlet tube (riser) is decreased; in the inlet tube, the average density is decreased while the average density is increased in the outlet tube.

If the mass flow rate is kept constant, these two effects don't influence the product of $v_{average}$ and $\rho=\rho_{H2}$, which can be seen by inserting equation 3.2 into equation 3.1; the density cancels out. The viscosity of gaseous hydrogen, however, is lower than that of liquid hydrogen, so the average viscosity in the outlet tube is increased if a liquid fraction exists in the outlet tube, lowering the Reynolds number in the outlet tube.

The qualitative analysis presented in the previous two paragraphs treats the medium as a homogenous mixture and does not include phase interactions between the phases. These generally increase drag, lowering the flow rate. Furthermore, bubbles may induce turbulence in the flow as liquid hydrogen needs to flow around them. It should be noted here that the model used to model the two phase behavior is the mixture model, which also treats the hydrogen as a homogenous mixture of gas and liquid. The mixture model is further discussed in section 4.2.

Assuming single phase flow in the inlet (liquid) and outlet (gas) tubes results in a Reynold number of approximately $1.3*10^4$ in the inlet tube and $8.7*10^3$ in the outlet tube when the values from Appendix A are used for the density and viscosity. This means the flow is turbulent in both tubes. This does not necessarily mean that the flow in the moderator cell is turbulent as well, because the flow has a much larger cross-sectional flow area, lowering the average fluid speed.

Moderator Cell

The Reynolds number in the moderator cell is difficult to estimate a priori, because the flow direction is not the same throughout the moderator cell. To get an idea of the average Reynolds number, an estimate is made that the flow in the lower half of the cell consists of saturated liquid flowing towards the reactor side of the cell and the flow in the top half of the cell consists of gas flowing towards the cell outlet. The moderator cell then operates as two half concentric tubes, being the lower half and the top half. These should not be confused with the pair of concentric tubes that form the inlet and outlet tubes. The hydraulic diameter D_h for a concentric tube is the difference in diameter between the inner and outer tube, in this case the inner and outer cell. The average flow speed can be calculated by dividing the overall volume flow rate by the flow surface, which is half of the cross section of the moderator cell. This calculation is given by equation 3.3, where v_{flow} gives the flow velocity, φ_m denotes the mass flow and D_1 and D_2 denote the inner and outer cell diameter respectively. The density is ρ, which should be the liquid density for the lower half of the cell and the gas density for the upper half of the cell. The extra factor of ½ in the denominator stems from the fact that for each flow direction, only half of the surface of the moderator cell is available.

$$v_{flow} = \frac{\frac{\varphi_m}{\rho}}{\frac{\pi}{4}(D_2^{\,2} - D_1^{\,2}) * \frac{1}{2}} \tag{3.3}$$

The Reynolds number is then calculated as

$$\mathrm{Re} = \frac{\rho v_{flow} D_h}{\mu} = \frac{\rho v_{flow}(D_2 - D_1)}{\mu} = \frac{\varphi_m (D_2 - D_1)}{\mu \frac{\pi}{4}(D_2^{\,2} - D_1^{\,2}) * \frac{1}{2}} = \frac{8\varphi_m}{\pi\mu(D_2 + D_1)} \tag{3.4}$$

Using an outer cell diameter of 0.221 m and an inner cell diameter of 0.199 m, as was the case in the advanced design (Appendix A), a mass flow rate of 2.0 g/s and liquid an gas viscosities as specified in Appendix A, gives Reynolds numbers of $1.0*10^3$ for the lower part and $7.5*10^3$ for the upper part.

These results imply laminar flow in the lower part and turbulent flow in the upper part of the moderator cell. This calculation, however, also assumes that the void fraction in the moderator cell is 50% on average, since half the cell is filled with liquid and half the cell is filled with gas in this calculation. The average void fraction throughout the moderator cell is expected to be much lower than 50% (as this is desirable for effective neutron moderation), and complete phase separation will likely only occur near the very top of the moderator cell as gas collects at the top of the cell. Here, the assumption is made that the inlet temperature of the hydrogen is sufficiently low that it only starts to boil inside the frontal volume, where it is heated by neutron radiation. If the inlet temperature of the hydrogen is too near to the boiling point, the hydrogen may start to boil prematurely, giving rise to a more spread out vapor source.

The Reynolds numbers obtained in this estimate are not likely to be very accurate, since the 50/50 distribution of gas and vapor and complete phase separation throughout the domain are not entirely realistic. For reasons of computational effort and simplicity, however, the flow in the moderator cell will be assumed to be laminar, because the Reynolds number as calculated for the lower part indicates laminar flow. In a later chapter, this assumption will be checked.

3.1.2 Total Heat Load

KHC and RID made estimates of the heat loads ([11] and [12], respectively), which are summarized in table 3.1. The causes for the difference between these two estimates are that both teams used a different reactor power. KHC used 3 MW, as opposed to 2 MW for RID. The cause of this lies in the fact that the original tender entailed an increase in reactor power from 2 MW to 3 MW, which was no longer incorporated in the final design. Also, the estimates were based on different comparative literature; KHC mainly based it on their own experience, while RID used other examples. Early simulations performed in this thesis used the KHC estimate, while in further simulations the RID estimate is used.

Estimated Nuclear Heat Load (W)	KHC	RID
Hydrogen	250	162
Moderator Cell	291	162

Table 3.1: nuclear heat load estimates

All heat absorbed in the vacuum shell and the helium containment vessel is assumed to be removed by the reactor coolant. Note that the heat load on the hydrogen is mainly from neutron radiation, while the aluminum is mainly heated by gamma rays. This is a result of the different cross sections for different kinds of radiation for different materials.

From table 3.1, the maximum amount of hydrogen vapor production per second ($Prod_{vap}$ in units g/s) can be calculated with equation 3.5, by dividing the total nuclear heat load power (P_Q in units W) to be removed by the hydrogen by the latent heat of hydrogen (Δh_{vap} in units J/g) at the design conditions.

$$\mathrm{Prod}_{vap} = \frac{P_Q}{\Delta h_{vap}} \tag{3.5}$$

The latent heat is 889,52 J/mol, which equals 441,23 J/g when divided by the molar mass of hydrogen (2.016 g/mol) [9]. This results in a vapor production of 1.23 g/s for the KHC estimates and 0.73 g/s for the RID estimates. This results in flow qualities of 0.37 and 0.62, respectively, as calculated by equation 3.6, with X the flow quality, $\varphi_{m,gas}$ the gas mass flow rate and $\varphi_{m,total}$ the total mass flow rate.

$$X = \frac{\varphi_{m,gas}}{\varphi_{m,total}} \tag{3.6}$$

Both vapor production rates are significantly lower than the 2 g/s mass flow rate that KHC specified, which means an amount of liquid hydrogen has to leave the moderator cell along with the produced vapor, since the vapor production rate is lower than the mass flow rate. This means the void fraction in the outlet tube cannot be 100%, as was assumed in section 3.1.1. It also implies that both phases are present at the cell outlet. This, in turn, means the top of the moderator cell is not occupied exclusively by gas (with the exception of the liquid coming into the moderator cell from the inlet), but by a mixture of gas and liquid. The Reynolds number calculated in section 3.1.1 for the top half of the cell is therefore invalid, as it was assumed the top half of the cell was filled by 100% gas.

Note that the calculated vapor production rate $Prod_{vap}$ is a maximum value; the entire nuclear heat load is used to evaporate the hydrogen, implying the incoming liquid is at saturation temperature, as is the outgoing gas. This implies the temperature of the hydrogen is the same everywhere in the moderator cell. If the hydrogen leaves the moderator cell at a higher temperature than at which it enters, a lower vapor production rate would be the result, because part of the energy would be needed to heat up the hydrogen instead of using the entire heat load to evaporate it.

3.1.3 Heat Sources

Heat comes into the hydrogen in multiple ways, as is schematically depicted in figures 3.1a and 3.1b. Figure 3.1a shows the heat flow for the system with an open inner cavity while figure 3.1b shows the heat flow for the system with a vacuum inner cavity. Here, the three boundary system is again visible; the liquid hydrogen (LH_2) and gaseous hydrogen (GH_2) mixture is enclosed by the moderator cell itself, the vacuum layer and the helium containment vessel.

Note that q_1'' is a surface heat source (units Wm^{-2}), while q_1''' is a volumetric heat source (units Wm^{-3}), as is the case for q_2'' and q_2'''.

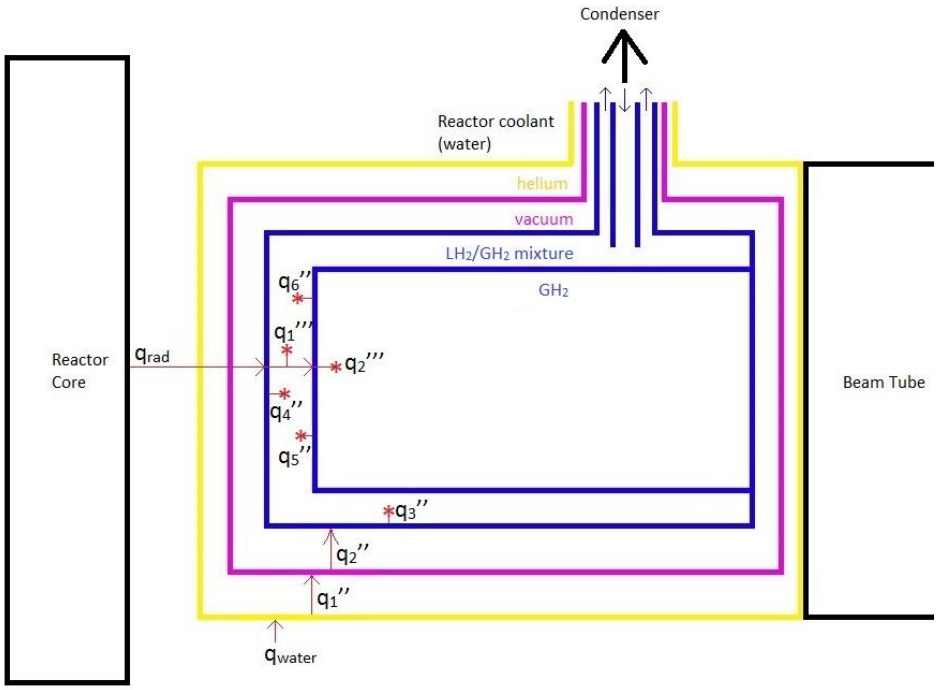

Figure 3.1a: heat flow schematic for an open inner cavity. The arrows indicate heating of structural components while the asterisks indicate heating of the hydrogen. Note that all heat must be removed by the LH_2/GH_2 mixture, since no other heat sinks are available. The heat sources are the radiation heat from the reactor core and heat from contact with the reactor coolant.

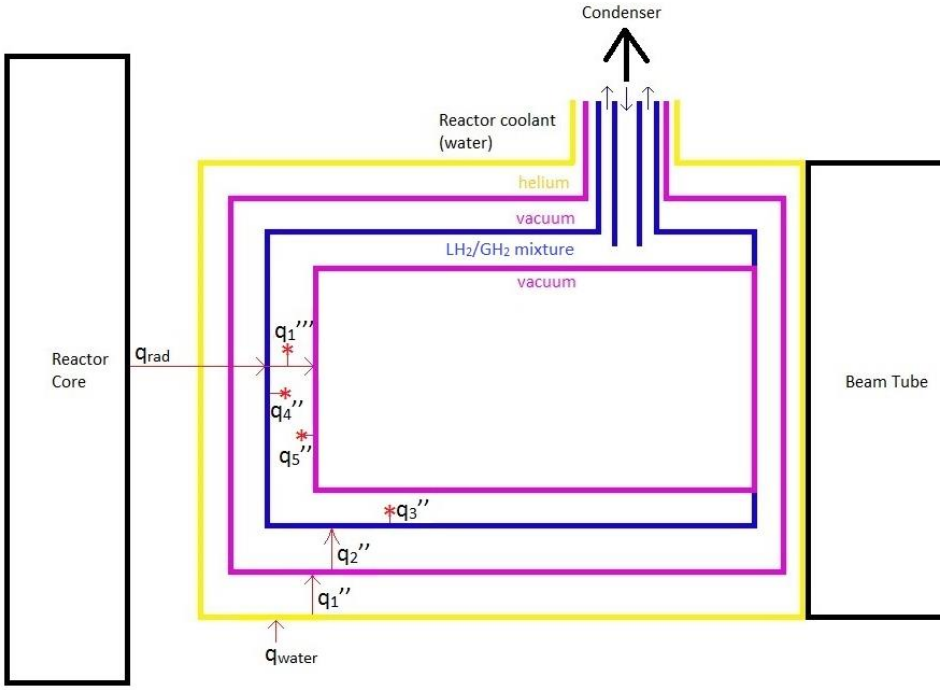

Figure 3.1b: heat flow schematic for a vacuum inner cavity. Note that the absence of heat sources q_2''' and q_6'' does not necessarily imply a lower total heat load; in order for the neutron moderation to remain the same for an evacuated inner cavity, the total heat load from neutron radiation should remain roughly the same, as the same amount of heat needs to be removed from the neutrons.

Nuclear Radiation

The main heat source for the liquid hydrogen is the radiative power coming from the reactor (q_{rad} with unit W in figures 3.1). This splits into a volumetric heating of the hydrogen, mainly by neutron radiation (q_1''' and q_2''') and surface heating of the aluminum moderator cell, mainly by gamma radiation (q_4'' and q_5''). In the case of an open inner cavity, the heat deposited in the hydrogen in this cavity is removed by the flowing LH_2/GH_2 mixture as well (q_6'' in figure 3.1a); this heat source is not present in a vacuum cavity design. the absence of heating of the hydrogen gas in the cavity does not necessarily mean that the total heat load is lower, however; in order for the neutron moderation to retain the same level as in figure 3.1a, the total amount of heat removed from the neutrons should be roughly the same for both figures. This would manifest in a larger value for q_1''', which can be achieved by lowering the average void fraction in the cell, for instance by decreasing the temperature of the incoming fluid or increasing the mass flow rate while retaining 100% liquid in the inlet.

Thermal Radiation

The moderator cell will also receive heat originating from radiation coming from the vacuum chamber surrounding it (q_2'' in figures 3.1). The vacuum chamber is in thermal contact with the reactor coolant via the helium layer (q_1'' in figures 3.1) and the helium containment vessel (q_{water}). The helium layer is very thin and both helium and the aluminum have a high thermal conductivity, so the vacuum chamber and helium containment vessel are assumed to have the same temperature as the reactor coolant (i.e. 40°C).

Because both the vacuum chamber and the helium containment vessel are at approximately the same fixed, known temperature (40°C), radiative heating of the vacuum chamber and the helium containment vessel is not likely to have a large influence; heat transfer to the moderator cell only depends on the temperature difference between the vacuum chamber and the moderator cell. Therefore, radiative heating of the vacuum chamber and the helium containment vessel is not incorporated in this analysis.

The heat source to the hydrogen due to the helium containment vessel being in contact with the reactor coolant is given by q_3'' in figures 3.1. The highest heat resistance in this path lies in the vacuum layer. To determine if this heat source is relevant, the equation for radiative heat transfer between two parallel plates is used [14]

$$P_{rad} = \frac{A\varepsilon_1\varepsilon_2}{\varepsilon_1 + \varepsilon_2 - \varepsilon_1\varepsilon_2}\sigma(T_1^4 - T_2^4) \tag{3.7}$$

The parallel plate approximation is chosen, because the gap between the moderator cell and the vacuum shell around it is small compared to the diameter of the moderator cell. P_{rad} is the transferred radiative power from the vacuum containment vessel to the moderator cell, A is the surface of one of the plates (the moderator cell in this case), ε_1 and ε_2 are the emissivity coefficients for the two surfaces respectively while T_1 and T_2 are the temperatures and σ is the Stefan Boltzmann constant (which has a value of $5.67*10^{-8}$ $Js^{-1}m^{-2}K^{-4}$). A typical value for the emissivity coefficient of polished aluminum is 0.1, albeit slightly high to be on the safe side when calculating an upper value for the radiative heat transfer. At the dimensions for the advanced design of the moderator cell (Appendix A), the surface of the moderator cell is about 0.24 square meters. This results in a power

of 7W for the moderator cell, which is negligible when compared to the total heat load. In effect, this means that q_{water}, q_1'', q_2'' and q_3'' are not incorporated in the simulations.

3.1.4 Driving Force

In the simulations where the flow is determined by the pressure difference between cell inlet and outlet, this pressure difference has to be calculated. The pressure difference is comprised of the hydrostatic pressure difference between the inlet and outlet tubes, the pressure loss as a result of friction in the inlet and outlet tubes and the pressure loss in the condenser, following equation 3.8.

$$\Delta p_{Cell} = \Delta p_h - p_{loss,cond} - p_{friction,tubes} \tag{3.8}$$

Here, Δp_{Cell} is the pressure difference between the inlet and the outlet of the moderator cel, Δp_h is the hydrostatic pressure difference between the inlet and outlet tubes, $p_{loss,cond}$ is the pressure loss in the condenser and $p_{friction,tubes}$ is the pressure loss due to friction in the tubes. In equation 3.8, all quantities used are absolute values; the minuses in the equation account for the fact that the last two terms on the right are loss terms while the first term is a source term for Δp_{Cell}. When the flow is in steady state, Δp_{Cell} will equal the pressure loss due to friction in the moderator cell. In other words, the flow rate will be at a value where the hydrostatic pressure difference Δp_h that drives the flow equals the sum of all friction terms.

The maximum difference in hydrostatic pressure occurs when the riser is filled with gas and the down comer is filled with liquid. This can be formulated as follows

$$\Delta p_h = g * h * (\rho_l - \rho_g) \tag{3.9}$$

Where g is the gravitational acceleration, h is the height of the fluid column (i.e. 3 m, which is the length of the inlet and outlet tubes in the KHC designs) and ρ_l and ρ_g are the liquid and gas densities of hydrogen, respectively (see Appendix A). This leads to a maximum pressure difference of 1984 Pa. As it has been established in the previous section that the void fraction in the riser will not be 100%, the hydrostatic pressure difference will be lower than what was calculated above, because the average density difference between the fluid in the riser and the down comer will be smaller. The void fraction in the riser can be incorporated in equation 3.9 by modifying the density in the riser, which is simply ρ_g in equation 3.9.

$$\Delta p_h = g * h * (\rho_l - (\rho_g * \alpha + \rho_l * (1 - \alpha)) \tag{3.10}$$

Which can be simplified to

$$\Delta p_h = g * h * (\rho_l - \rho_g) * \alpha \tag{3.11}$$

In the above equations, α denotes the average void fraction in the riser.

3.1.5 Friction

The power dissipated as a result of friction is generally negligible in flow problems, as is the case in this design. The following equation gives this power [13, pp. 58]

$$A_f = \sum_i (4 * \frac{f}{2} * < v >^2 \frac{L}{D_h}) \quad (3.12)$$

Here, A_f is the power dissipated per unit mass (units J/kg), f is the fanning friction factor, $<v>$ is the average speed of the medium, L is the length of the pipe and D_h is the hydraulic diameter. The summation is done over the two concentric pipes. The friction factor f is chosen at 0.02, which is the highest it can get for tubes at Reynolds numbers above 2000 [13, pp. 84], and the inlet and outlet tube diameters and length are as stated in Appendix A. The average speed is again determined by dividing the mass flow rate φ_m (2 g/s) by the cross sectional area of the pipe A and the density of the medium ρ. In the riser, a void fraction of 100% is assumed to achieve maximum speed, in order to calculate the maximum energy loss due to friction. The result of this calculation is an energy dissipation of 0.15 J/kg in the inlet tube and 0.49 J/kg in the outlet tube. Adding up these numbers and multiplying them by the mass flow rate gives a dissipation of 1.3 mW. This is negligible when compared to the heat load estimates given in table 3.1, as was to be expected. Equation 3.13 shows this calculation, where the first term is for the down comer (the inner tube) and the second term is for the riser (the outer tube).

$$A_f = 4 * \frac{f}{2} * \left(\frac{\varphi_m}{A_{in} * \rho_l} \right)^2 \frac{L}{D_{in}} + 4 * \frac{f}{2} * \left(\frac{\varphi_m}{A_{out} * \rho_g} \right)^2 \frac{L}{D_{out} - D_{in}} \quad (3.13)$$

Multiplying the energy dissipation per kg (A_f) by the density of the medium (liquid hydrogen for the inlet, gaseous hydrogen for the outlet) and adding up the results (eq. 3.14) gives a total pressure loss due to friction (ΔP_f) of 11.63 Pa in the tubes, of which 10.71 Pa is in the riser and 0.92 Pa is in the down comer.

$$\Delta P_f = A_{f,inlet} * \rho_{liquid} + A_{f,outlet} * \rho_{gas} \quad (3.14)$$

These are negligible quantities when compared to the difference in hydrostatic pressure between the riser and the down comer (unless the void fraction in the riser approaches zero).

It should be noted that the pressure loss in the condenser is not accounted for in this analysis, because the geometry of the hydrogen flow domain in the condenser is not well known yet. A significant pressure drop may occur, since a condenser generally has a large surface area with respect to the cross sectional flow area in order to achieve a high heat extraction capability, which may cause a high flow resistance due to wall friction.

3.2 Geometry and Mesh

3.2.1 Geometry

Both geometry and mesh were made in computational tools made by ANSYS. The geometry was simplified to a combination of cylinders without rounding the edges of these cylinders, in order to ease geometry and mesh generation. In the physical fabrication of the cell, the cylinder edges will be rounded, since this gives the cell more structural integrity when compared to unrounded edges. Comparing figures 2.1 and 2.3 with figure 3.2 shows this difference; in the design sketches in chapter 2, the edges at the reactor side of the cell are rounded, while they are not rounded in the

geometrical models used in this thesis. Note that in figure 2.1, the design sketch does not include rounding of the cylinder's edge at the beam tube side.

Two geometries were made, a first one with dimensions according to the preliminary design and a second one where a more advanced design by KHC was applied. In both cases, the inner cell was made fully closed in order to decrease the size of the flow domain. Since only steady state behavior was investigated, the liquid hydrogen level in the inner cavity will be constant, so this is a fair simplification. Graphic depictions of the flow domain are given in figures 3.2 and 3.3. The former is an outside view, while the latter shows the inner structure. Figure 3.4 highlights the frontal volume, where the volumetric heating of the hydrogen takes place, as well as the inlet surface (green, upper right), which can be seen to lie lower than the outlet surface (the larger circle around the inlet). The walls that seem to be in the flow domain in figures 3.3 and 3.4 are virtual and are placed there to aid in meshing, they are not flow obstructions of any kind.

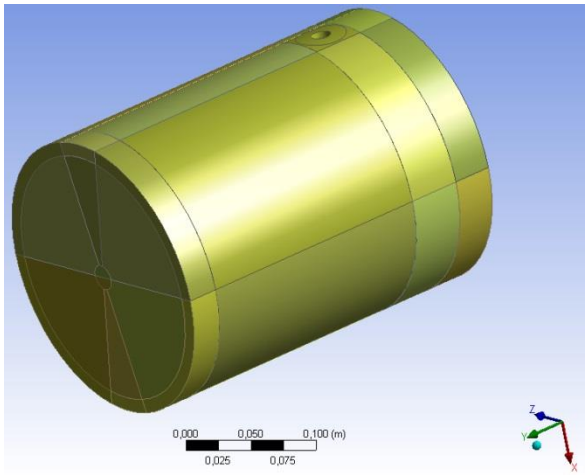

Figure 3.2: outside view of the flow domain.

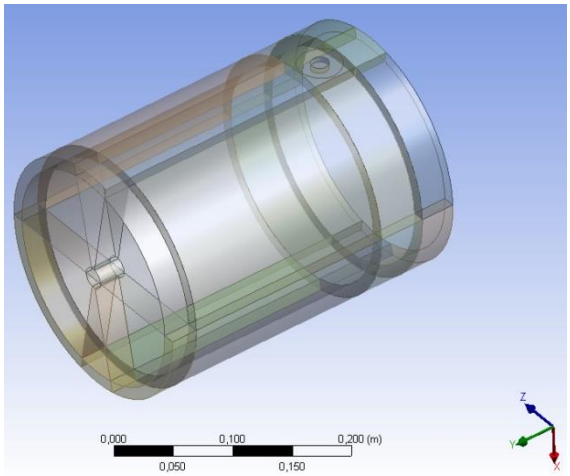

Figure 3.3 see through view of the flow domain.

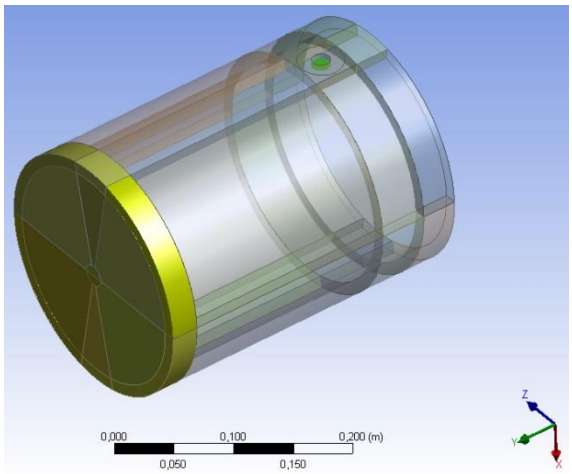

Figure 3.4: flow domain with the frontal volume and inlet highlighted in yellow and green respectively.

Some simulations were done with the hydrogen inlet and outlet pipes incorporated in the geometry and mesh, some were done without. Because the available license limits the amount of cells in the mesh to 512000, the mesh inside the moderator cell could be refined further when the pipes were not included.

3.2.2 Mesh

The mesh is made in a structured way, making it highly regular. Only at the areas at the center of each cylinder used to comprise the geometry, some irregularities occur, which is inherent to the method of meshing that is used.

The area where the inlet and outlet tubes enter the domain has much smaller grid cells. In this area, liquid hydrogen comes into the cell through the inlet and a two phase mixture leaves the cell through the outlet. This results in high velocity and void fraction gradients. For this reason, the mesh grid cells need to be smaller in this area to accommodate for the abrupt changes in flow variables in this area.

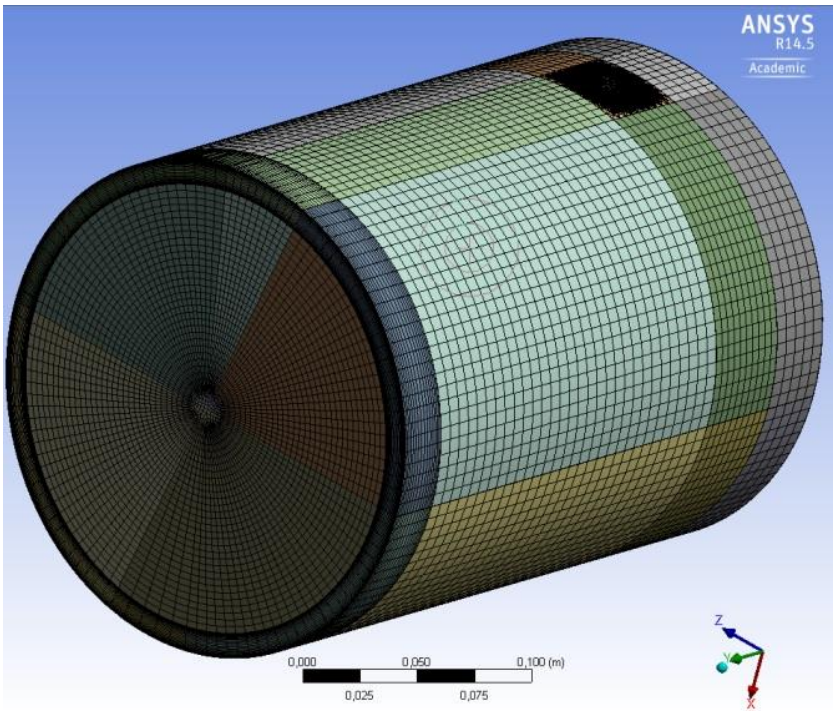

Figure 3.5: overall mesh. The darker area on the top right is where the inlet and outlet pipes are attached to the cell. The mesh is finer in this region to account for high velocity gradients due to counter flow at the inlet and outlet. The three arrows on the bottom right show which way the cell is oriented in the figure; the positive x-direction is downwards, the y-vector points in the direction of the reactor core.

Inflation Layers

The mesh for the case without inlet and outlet pipes is shown in figure 3.5. In the flow domain layer in between the shells, the cells near the walls are narrower than the cells in the middle. This is called an inflation layer, as the cells 'inflate' as they are further from the walls. The same is done for the frontal volume, where cells near the front and back walls of the frontal volume are smaller than ones that lie more towards the middle. This is done in order to better account for viscous effects near the walls as well as heat transfer from the front and back surfaces of the frontal volume, since the velocity and temperature gradients are expected to be large near the wall because of these effects. Figures 3.6 show a side cutout view of the moderator cell. Figure 3.6a gives an overview image and 3.6b gives a zoomed in image from the same angle, zoomed in on the top of the frontal volume, to show how the aforementioned inflation layers come together.

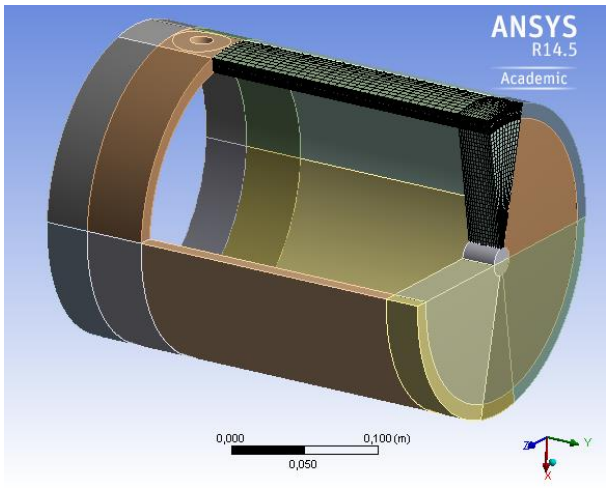

Figure 3.6a: cutout section of the moderator cell, showing the mesh of the inflation layers. Figure 3.6b shows the same point of view, zoomed in on the area at the outer edge of the frontal volume, where the inflation layers meet.

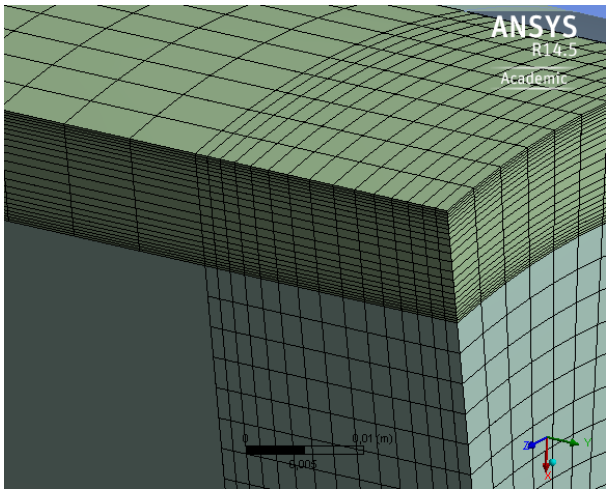

Figure 3.6b: cutout section of the moderator cell, zoomed in on the inflation layers. It is clearly seen that cells become smaller as they are closer to the walls of the inner and outer moderator cell shells, which is done to better account for viscous effect near the wall as well as heat transfer from the front and back walls of the frontal volume, which are heated by gamma radiation coming from the reactor core.

Inlet/Outlet Area

The dark area at the upper right in figure 3.5 is the inlet and outlet area, which is shown in greater detail in figure 3.7. this area is darker in figure 3.5, because the grid cells are smaller in this area than in the rest of the geometry, and each grid cell boundary is depicted as a black line.

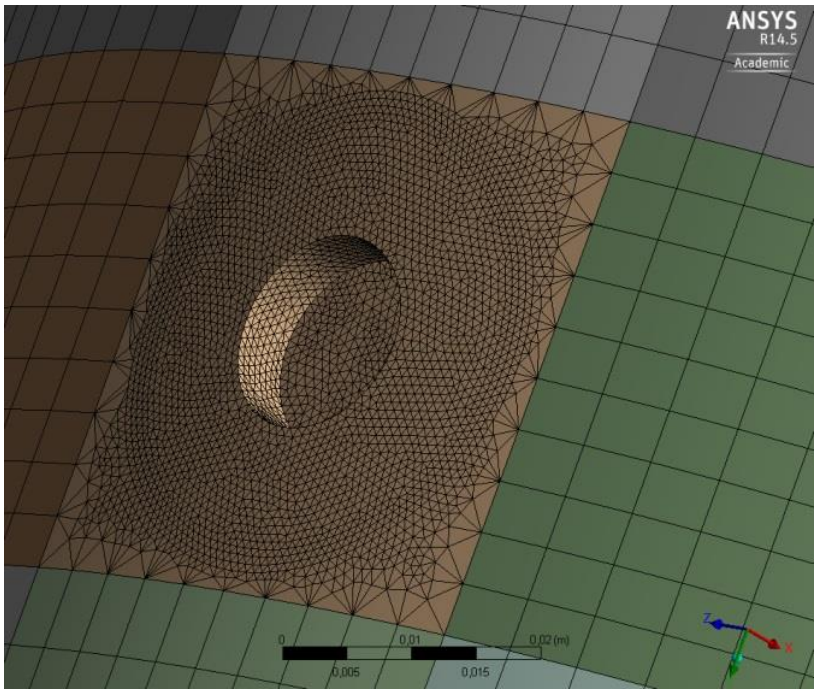

Figure 3.7: inlet and outlet mesh. The mesh is refined here to better account for large gradients in flow variables due to the close proximity of the inlet and outlet of the moderator cell. The protrusion of the inlet tube in the moderator cell is visible as a depression in the outer surface of the flow domain.

Preliminary Design Geometry

In this chapter, only the mesh for the advanced design is discussed, since the preliminary design is only used in some single phase simulations (SP1, SP2 and SP3A). The geometry of the preliminary

design is given in figure 3.8. The preliminary design has a much wider frontal volume (6 cm instead of 2.5 cm) and the inlet and outlet are placed closer to the back of the cell. The mesh is structured in a similar way as in the advanced design geometry.

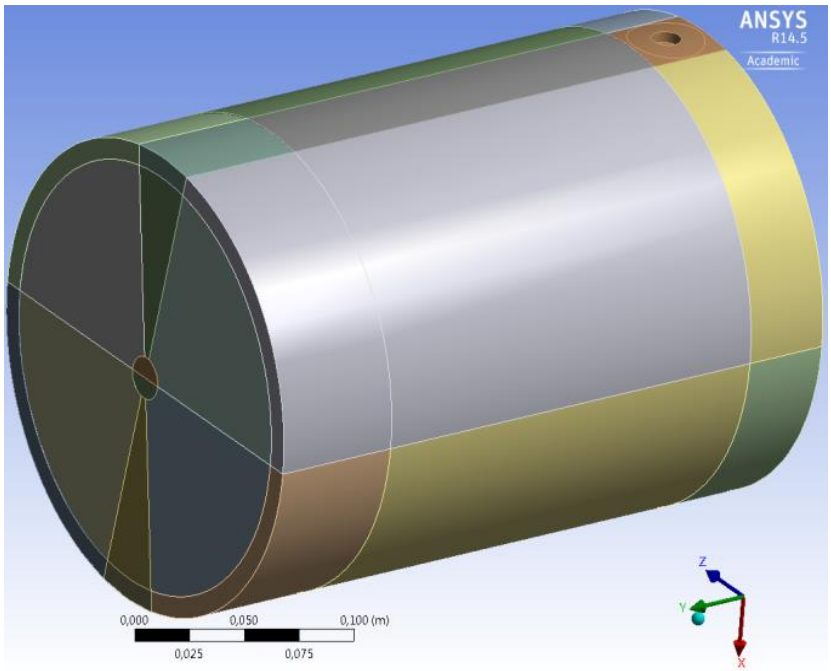

Figure 3.8: preliminary design geometry. This design has a much wider frontal volume and the inlet and outlet are placed closer to the back of the cell, as can be seen when this figure is compared to figure 3.2.

4 Flow Modeling

In this chapter, the setup of the simulations and the underlying models are discussed. Fluent offers many different models, and in this chapter, the choices of the models used are motivated. Oftentimes, a choice had to be made between accuracy and computational cost. As the computational resources were relatively limited, these choices generally prioritize computational simplicity.

4.1 Boundary Conditions

Only the flow domain is modeled, not the aluminum of the moderator cell. The heat load from the aluminum is modeled as a surface heat source on the two surfaces facing the reactor, with the distribution between the two estimated in concert with RID personnel. Heating from neutron moderation is modeled as a homogenous volumetric heating in the frontal volume and the inner gas cavity (if present). Again, a distribution between the two is estimated. The heat absorbed by the gas in the inner cavity is removed by the mixture flowing in the domain between the shells. This heat flow is modeled as a homogenous surface heating along the inner shell wall. This way, the processes inside the inner cavity did not have to be modeled directly. In simulations of the later design, i.e. with vacuum instead of the inner gas cavity, all neutron moderation heat is absorbed in the frontal volume.

4.2 Single Phase Flow

In multiphase computational fluid dynamics, it is useful to start with single phase simulations in order to better understand the flow. In this research, four single phase simulations were done: firstly, a hydrostatic pressure difference was applied between the inlet and outlet of the moderator cell of the preliminary design. We will refer to this simulation as SP1 (Single Phase simulation 1). The goal of this simulation was to get a feel for what order of magnitude a realistic mass flow would be and to see what the flow field would look like. Another simulation was done, where the natural convection was modeled (SP2). In this case, the supply and drain tubes were incorporated in the simulation, again using the preliminary design. This simulation was done to check whether the natural circulation would start correctly without forcing the flow. Thirdly, the mass flow was specified at 2 g/s, for the moderator cell only, to see what the flow field would look like if the mass flow was forced at the specified 2 g/s. This simulation is done for both the preliminary design (SP3A) and the advanced design geometry (SP3B).

The first two simulations (SP1 & SP2) represent the use design, the third simulation (SP3A & SP3B) is done for both the preliminary design and the advanced geometry with the gas filled cavity, both with the KHC heat load estimate. The setup of each of these simulations will be discussed in the following sections. Note that all single phase simulations use the KHC heat load estimates and a gas filled cavity, even SP3B which uses the geometry of the advanced design (narrower frontal volume). The reason here is that the design geometry was changed before the decision was made to evacuate the inner cavity. Table 4.2 shows an overview of all simulations performed in this thesis.

4.2.1 Specified Pressure Difference (SP1)

In the first case, the preliminary design was used, with the heat load estimates by KHC. It is a single phase, laminar simulation with the energy equation enabled to account for heat transfer and heating of the hydrogen. The material used is liquid hydrogen, the material properties used are listed in

Appendix A. The density is modeled as a linear function of the temperature to account for expansion with heating. The coefficients in the density equation are chosen as to represent a fit to the density profile of liquid hydrogen between 20 K and 21 K at a pressure of 1.5 bar, which has been linearly extrapolated to temperatures above the saturation temperature [9]. This results in a hydrogen density equation of the form

$$\rho_h = 95.01 - 1.186 * T \tag{4.1}$$

where ρ_h is the liquid hydrogen density in kgm^{-3} and T is the hydrogen temperature in K. The other properties of liquid hydrogen are from NIST [9] as well.

The mesh is divided into two cell zones, being the frontal volume and the rest of the volume (figure 3.4), so a volumetric heating can be applied over the frontal volume as shown in section 3.2. The volumetric heating density is calculated as

$$Q'''_{fv} = \frac{f_1 * Q_h}{V_f} \tag{4.2}$$

where Q'''_{fv} is the volumetric heat production density in Wm^{-3}, Q_h is the nuclear heat load from neutron moderation in the hydrogen in W, V_f is the volume of the frontal volume in m^3 and f_1 is a factor estimated as the fraction of Q_h that is absorbed in the frontal volume. The heat absorbed by the gas in the inner cavity is transferred to the hydrogen layer in between the inner and outer shells of the moderator cell. This is modeled as a uniform surface heating along the cylindrical part of the inner shell (i.e. without the top and bottom). The equation giving the surface heat flux is

$$Q''_{in} = \frac{(1 - f_1) * Q_h}{A_i} \tag{4.3}$$

where Q_{in}'' is the heat flux and A_i is the surface area of the cylindrical part of the inner shell.

The heat absorbed in the aluminum of the moderator cell is modeled as a uniform surface heat flux from the front and back walls of the frontal volume, with an estimated distribution given by f_2. The equations are

$$Q_f'' = \frac{f_2 * Q_{al}}{A_f} \tag{4.4}$$

and

$$Q_b'' = \frac{(1 - f_2) * Q_{al}}{A_b} \tag{4.5}$$

where Q_f'' and Q_b'' are the front and back wall heat fluxes, Q_{al} is the estimated heat load on the aluminum and A_f and A_b are the surfaces of the front and back walls respectively. Note that, although the frontal volume is a cylindrical slab, these surfaces are not the same, because the back wall has a slightly smaller diameter because it is part of the inner shell, while the front wall is part of the outer shell. The results of the above calculations are summarized in table 4.1. The heat load distribution

coefficients f_1 and f_2 are merely estimates, they should not be treated as absolute. They are arrived upon in concert with RID personnel. The influence of these parameters is not further investigated in this thesis.

Design	preliminary	advanced	
Heat Load Estimate	KHC	KHC	RID
Q_h (W)	250	250	162
Q_{al} (W)	291	291	162
V_f (m^3)	$2.3*10^{-3}$	$9.6*10^{-4}$	$9.6*10^{-4}$
A_i (m^2)	0.15	0.17	0.17
A_f (m^2)	0.038	0.038	0.038
A_b (m^2)	0.032	0.031	0.031
f_1	0.67	0.83	1
f_2	0.75	0.67	0.8
Q_{fv}''' (Wm^{-3})	$7.3*10^4$	$2.2*10^5$	$1.7*10^5$
Q_{in}'' (Wm^{-2})	$5.5*10^2$	$2.2*10^2$	0
Q_f'' (Wm^{-2})	$5.7*10^3$	$5.1*10^3$	$3.4*10^3$
Q_b'' (Wm^{-2})	$2.3*10^3$	$3.1*10^3$	$8.2*10^2$

Table 4.1: heat load calculations for both the preliminary and the advanced design, based on estimates as done by RID and KHC. The advanced design in combination with the advanced design geometry is only used for simulation SP3B. Note that the inner cavity is open in the KHC heat load estimate for the advanced design, which manifests in a nonzero Q_{in}''.

Note that the heat load on the inner cavity is zero in the advanced geometry with the RID estimate for the heat load, because in this case, the design with a vacuum inner cavity was considered. For this reason, f_1 is 1 in this case.

The under relaxation factors for pressure, momentum, density, body forces and energy are 0.4, 0.4, 0.8, 0.8 and 0.6 respectively. These are somewhat lower than the default factors to increase stability. Under relaxation factors limit the change in calculated variables from iteration to iteration, in order to increase numerical stability. This is discussed in more detail in section 4.4.2.

To check for convergence, the mass flow rate difference between inlet and outlet is monitored (this should be zero at convergence), as well as the static temperature at the outlet and averaged over the volume. Both temperatures should reach constant values.

The pressure at the inlet is specified at 1.50 bar, while the pressure at the outlet is specified at 1.49 bar. This is about the value of the hydrostatic pressure difference at an average void fraction of 50 % in the riser and 0% in the down comer, as calculated by equation 3.11.

4.2.2 Natural Circulation (SP2)

The second single phase simulation entails the simulation of the natural circulation. Here, the full length of the supply and drain tubes is incorporated in the model. This means a large amount of grid cells is needed to model the tubes, necessitating a less detailed mesh in the moderator cell itself because of the limit on the number of grid cells. The general setup equals that of the previous case (SP1), however the inlet and outlet are both placed at the top of both pipes. Pressure is specified as

1.5 bar at both inlet and outlet. The inlet is modeled as a pressure inlet while the outlet is modeled as a pressure outlet.

Because the mesh in this simulation is less fine overall than it is in the other simulations, slightly higher under relaxation factors can be used to speed up convergence. The under relaxation factors used are 0.5, 0.5, 0.9, 0.9, 0.9 in the same order as given above. These under relaxation factors were found to provide sufficient numerical stability while allowing for a reasonable convergence speed.

4.2.3 Specified Mass Flow (SP3A & SP3B)

The third single phase simulation, where the mass flow inlet condition was used, uses roughly the same setup as SP1, with the difference that it has a mass flow inlet condition of 2 g/s instead of a pressure difference between inlet and outlet. The total heat load and heat load distribution are the same as in the pressure inlet case, with the inner gas cavity heat load incorporated as well. Since this simulation is done for two different geometries, the volumetric heat load differs. For the advanced design, the volumetric heat production density in the frontal volume is much higher, because the frontal volume is smaller in the advanced design than it was in the preliminary design.

4.3 Two Phase Flow

In the two phase flow simulations, only the advanced design is used, modeling the moderator cell without the hydrogen inlet and outlet tubes, as in SP1 and SP3A&B. The inner cavity is evacuated in all two phase simulations and the RID heat load estimate is used. The multiphase model used is the so-called mixture model, which treats the fluid as a mixture of the two phases in thermal equilibrium with each other. The mixture model is elaborated upon in section 4.3.1 and Appendix B. The viscous model is again the laminar model. The hydrogen liquid and vapor properties from NIST [9] are used, these are summarized in Appendix A. The liquid hydrogen density is the same as in the single phase simulations while the gaseous hydrogen density is considered as constant at the saturation density, since the hydrogen is not expected to reach temperatures high above the saturation temperature at reasonable void (gas) fractions.

In all simulations, the inlet temperature is specified at 21.5 K. The exact value is not well known, however, since it depends on the condenser performance and the mass flow rate.

Two phase flow modeling is substantially more complicated than single phase flow modeling. Therefore, the model setup is more complicated as well. The multiphase model is the mixture model with slip velocity. The mass transfer model, which models the transfer of mass between the phases (in this case mainly evaporation from liquid to gas), is the evaporation-condensation model, where the saturation temperature is 21.7 K. The evaporation and condensation frequencies have to be specified as well. The evaporation and condensation frequencies govern (in part) how much of the superheated liquid/subcooled gas evaporates/condenses. These quantities are not well known a priori and are usually fine-tuned to match experimental results. Because no experimental results are available, the influence of these parameters is investigated. The evaporation-condensation model is discussed in more detail in section 4.3.2.

Two sets of two phase simulations were done: one set to examine the effect of the aforementioned evaporation/condensation frequency (TP1), and one set to determine the effect of varying the mass flow (TP2). Table 4.2 shows an overview of all simulations performed.

name	phase	driving mechanism	flow domain	geometry	inner cavity	heat load estimate
SP1	single	pressure difference	cell only	preliminary	open	KHC
SP2	single	natural convection	cell with pipes	preliminary	open	KHC
SP3A	single	specified mass flow	cell only	preliminary	open	KHC
SP3B	single	specified mass flow	cell only	advanced	open	KHC
TP1	two	specified mass flow	cell only	advanced	vacuum	KHC
TP2	two	specified mass flow	cell only	advanced	vacuum	RID

Table 4.2: overview of the simulations performed. Note that, for simulation SP3B, the advanced design geometry is used, although the inner cavity is open. The decision to close the inner cavity was taken after the single phase simulations were performed. The change in the heat load estimates is a result of progressive insight; the RID heat load estimates were not available yet at the time of the single phase simulations.

In TP1, the mass flow is specified at 2 g/s and the simulation is done for a range of evaporation and condensation frequencies. The heat load estimates of KHC were used since the RID estimates were not available at the time. The diameter of the secondary phase (in this case this denotes the diameter of hydrogen gas bubbles) is left at the default value of 10^{-5} m, since no better estimate was available. This implies a dispersed flow regime, with many small bubbles.

In TP2, the default value of 0.1 is chosen for the evaporation and condensation frequencies, since there is no further knowledge with regard to the evaporation/condensation frequency in this specific moderator cell design. A range of mass flows is applied to the inlet, in order to investigate the dependence of the void fraction on the mass flow.

Here, the heat load estimates of RID were used as they are deemed more appropriate when compared to similar setups [12]. After consulting with RID personnel, the diameter of the secondary phase is estimated at 10^{-3} m instead of 10^{-5} m due to progressive insight. This means the program assumes the hydrogen gas consists of bubbles of 1 mm in diameter. Again, the dispersed flow regime is assumed.

The bubble size could be of large influence on the flow field, since a large bubble size might induce a switch in flow regime from bubbly or dispersed flow to for instance churn or slug flow. Furthermore, large, migrating bubbles are undesirable because they may induce spatial and temporal transients in neutron moderation. Since a bubble has a much lower particle density than liquid, neutron moderation is much less effective in a bubble than it is in liquid. If the neutron beam passes through a (large) bubble, neutron moderation will be diminished in the area of the bubble, increasing the neutron temperature of neutrons that pass through the bubble. This will cause a hot spot in the neutron beam cross section, which can also move in time as the bubble moves through the fluid domain, perpendicularly to the neutron beam.

Further research into the actual two phase flow regime in this cold neutron source is therefore recommended. In this thesis, no research or calculations regarding the two phase flow regime were performed.

Even though all simulations were done with the laminar solver, it should be kept in mind that this may not be accurate for larger mass flow rates.

The solution methods are the same as for the single phase simulations, with the addition of the first order upwind scheme for the spatial discretization of the volume fraction. The under relaxation

factors are tuned for each simulation to ensure numerical stability while providing reasonable convergence speed. The stability criteria monitored are again the mass flow rate difference between inlet and outlet and the mixture static temperature at the inlet and the outlet. Furthermore, the average void fraction in the flow domain and the total vapor production are monitored.

4.3.1 Momentum Modeling

The mixture model is the simplest multiphase model available in Fluent. It treats the phases as interpenetrating, with a volume fraction between 0 and 1 for each phase in each cell, denoted by α_k for phase k. In the continuity equation, the mixture density ρ_m and the mass averaged velocity v_m are used. In the mixture model, these are determined by the following equations [15]

$$\vec{v}_m = \frac{\sum_{k=1}^{n} \alpha_k \rho_k \vec{v}_k}{\rho_m} \tag{4.6}$$

for the mass averaged velocity vector. The mixture velocity is thus a mass weighted average of the velocity of the phases. The mixture density ρ_m is determined as a volume weighted average according to

$$\rho_m = \sum_{k=1}^{n} \alpha_k \rho_k \tag{4.7}$$

Here, the summation is done over two phases, being the liquid and the gaseous hydrogen, so *k* is either 1 or 2 and *n* is 2. The mass continuity equation for the mixture then reduces to

$$\frac{\partial}{\partial t}(\rho_m) + \nabla \cdot (\rho_m \vec{v}_m) = 0 \tag{4.8}$$

In equation 4.8, the first term is the local density change, in this simulation as a result of expansion or contraction by heat transfer. The second term is the convective term, which gives the net mass flow per unit volume into the volume element.

The momentum equation for the mixture is achieved by summing the individual momentum equations for the phases. It can be formulated as follows [15]. This equation is more elaborated upon in Appendix B.

$$\frac{\partial}{\partial t}(\rho_m \vec{v}_m) + \nabla \cdot (\rho_m \vec{v}_m \vec{v}_m) = -\nabla p + \mu_m \nabla^2 \vec{v}_m + g\rho_m + \vec{F} - \nabla \cdot \left(\sum_{k=1}^{n} \alpha_k \rho_k \overrightarrow{v_{dr,k}} \overrightarrow{v_{dr,k}} \right) \tag{4.9}$$

The first term on the left in equation 4.9 is the local momentum change term, while the second term on the left is the momentum convection term. The right side consists of the forces that drive the momentum change; the first term is the pressure term, the second term is the viscous stress term, the third term the gravity term and the fourth term the additional body forces. The last term on the right compensates for the fact that the second term on the left really should be solved for each phase separately. The compensating term is needed because this term is nonlinear in the fluid velocity.

The mixture viscosity is modeled as

$$\mu_m = \sum_{k=1}^{n} \alpha_k \mu_k \tag{4.10}$$

The drift velocity for phase *k* is

$$\overrightarrow{v_{dr,k}} = \overrightarrow{v_k} - \overrightarrow{v_m} \tag{4.11}$$

Which is the velocity difference between the mixture velocity and the velocity of the individual phase.

The energy equation is formulated as follows

$$\frac{\partial}{\partial t}\sum_{k=1}^{n}(\alpha_k \rho_k E_k) + \nabla \cdot \sum_{k=1}^{n} \alpha_k \vec{v}_k \rho_k h_k^{*} = \nabla \cdot \sum_{k=1}^{n} \alpha_k k_k \nabla T + S_E \tag{4.12}$$

Here, h_k^{*} is the specific stagnation enthalpy for phase *k*, with

$$h_k^{*} = h_k + \frac{v_k^{2}}{2} \tag{4.13}$$

where h_k is the specific enthalpy of phase *k*. The thermal conductivity of phase *k* is given by k_k, *p* denotes the pressure and S_E includes the other volumetric heat sources, which is heat by neutron moderation in the simulations discussed in this thesis. The first term on the right hand side of equation 4.12 denotes the energy transfer due to conduction. The first term on the left side is the local stagnation internal energy change term.

In cells adjacent to a wall with a specified heat flux, as is the case in the performed simulations, an additional term exists in equation 4.12 which accounts for this. In turbulent flows, the summation on the right hand side of equation 4.12 has an additional term, being the turbulent conductivity. In general, this greatly increases lateral mixing of thermal energy. In the flow discussed in this thesis, this would expectedly influence the flow mainly in the frontal volume, where heat is coming from the walls as they heat up due to gamma radiation.

The terminal relative velocity, or the velocity difference between the two phases at equilibrium between the buoyancy force and drag force, is assumed to be reached within short time scales in the mixture model. It is calculated according to Schiller and Naumann [16]

$$\vec{v}_{pq} = \frac{\tau_p}{f_{drag}} \frac{\left(\rho_p - \rho_m\right)}{\rho_p} \overrightarrow{g_{eff}} \tag{4.14}$$

Here, *p* denotes the secondary (particulate) phase (gas bubbles) and *q* denotes the primary phase (liquid). The effective gravity vector of the mixture is denoted by $\overrightarrow{g_{eff}}$, this is the normal gravitational acceleration minus the mixture acceleration.

The particle relaxation time τ_p is a measure of how long it takes for a nonmoving particle to be accelerated to its terminal relative velocity v_{pq} [17]. The particle relaxation time is given by

$$\tau_p = \frac{\rho_p d_p{}^2}{18\mu_q} \tag{4.15}$$

Here, d_p is the diameter of the secondary phase (gas bubbles). This equation is a result of the drag coefficient given by Stokes law, which is valid for low Reynolds numbers, i.e. laminar flow, as is assumed in the simulations performed in this thesis [17].

$$C_D = \frac{24}{\mathrm{Re}} = \frac{24 * \mu_q}{\rho_q v_{pq} d_p} \tag{4.16}$$

The drag force is given by

$$F_{drag} = \frac{1}{2}\rho_q v_{pq}{}^2 C_D A \tag{4.17}$$

where *A* is the cross sectional area of the particles. Combining equations 4.16 and 4.17 and rewriting *A* as a function of the bubble diameter, we obtain

$$F_{drag} = 3\mu_q v_{pq} \pi d_p \tag{4.18}$$

The acceleration of the particle due to drag is then given by

$$a_{drag} = \frac{F_{drag}}{m_p} = \frac{3\mu_q v_{pq}\pi d_p}{\frac{1}{6}\rho_p \pi d_p{}^3} = \frac{18\mu_q v_{pq}}{\rho_p d_p{}^2} \tag{4.19}$$

The particle relaxation time is then given by

$$\tau = \frac{v_{pq}}{a_{drag}} = \frac{\rho_p d_p{}^2}{18\mu_q} \tag{4.20}$$

Which coincides with equation 4.15.

The effective gravity vector $\overrightarrow{g_{eff}}$, used in equation 4.14, is given by [15]

$$\overrightarrow{g_{eff}} = \vec{g} - (\vec{v}_m \cdot \nabla)\vec{v}_m - \frac{\overrightarrow{\partial v_m}}{\partial t} \tag{4.21}$$

Where the first term on the right hand side is the normal gravitational acceleration, the second term is the convective term of the acceleration and the last term is the local acceleration of the mixture. The effective gravity vector should be seen as the specific resulting force the particle experiences due to gravity and acceleration; if the local and convective terms of the acceleration sum to the gravitational acceleration, the gas bubble is in 'free fall', so it will not experience any resulting force resulting from mass in the sense that it seems weightless. Much like an astronaut orbiting earth, the acceleration vector matches the gravity vector, so he feels no gravity, he feels weightless. In this case, $\overrightarrow{g_{eff}}$ is zero. The effective gravity vector influences the direction and magnitude of the

buoyancy force acting on a gas bubble. The buoyancy force, in turn, determines the terminal relative velocity of a gas bubble.

Looking back at equation 4.14, we see that the relative velocity between the phases becomes zero if $\overrightarrow{g_{eff}}$ is zero. With the previous paragraph in mind, this can be explained the following way. If the effective gravity vector is zero, the fluid is essentially in freefall. Thus, the actual weight does not matter anymore (however, the mass still determines the inertia). This means that a gas bubble or particle in a liquid will not experience any buoyancy due to density differences between the phases, since both phases are essentially in freefall. If no buoyancy force is acting on a particle, the terminal relative velocity of that particle will be zero, since the drag force tends to reduce all relative velocity differences to zero.

The drag function f_{drag} used in equation 4.14 is a function of the Reynolds number, it can be calculated by a number of empirical models, however it was found that all available options except 'none' gave divergent results. This means f_{drag} is not calculated. As a result, the relative velocity difference between the phases is not actually calculated by Fluent. This means that the calculations shown in equations 4.14 through 4.21 are not performed. Therefore, there is no velocity difference between the phases in the simulations performed in this thesis. This means gas and liquid have the same velocity, so the drift velocity as calculated in equation 4.11 and used in equation 4.9 is zero, reducing equation 4.9 to

$$\frac{\partial}{\partial t}(\rho_m \vec{v}_m) + \nabla \cdot (\rho_m \vec{v}_m \vec{v}_m) = -\nabla p + \mu_m \nabla(\overrightarrow{\nabla v}_m + \nabla(\vec{v}_m{}^T)) + g\rho_m + \vec{F} \tag{4.22}$$

This essentially reduces the mixture model to a homogenous multiphase model. Since this is obviously detrimental to the realism of the outcomes of the simulations, further research including the drag function is required to get a realistic image of the flow.

4.3.2 Mass Transfer Modeling

To model the boiling process, the evaporation-condensation model is used. In this model, mass transfer is modeled as follows [15]

$$\dot{m}_{l\to g} = K_{evap} * \alpha_l \rho_l \frac{T_l - T_{sat}}{T_{sat}} \tag{4.23}$$

For evaporation at temperatures T_l above saturation and

$$\dot{m}_{g\to l} = -K_{cond} * \alpha_g \rho_g \frac{T_g - T_{sat}}{T_{sat}} \tag{4.24}$$

For condensation at temperatures T_g below saturation. The subscript *l* denotes the liquid phase while the subscript *g* denotes the gas phase. The liquid gas fraction α_l equals 1-α_g. Note that α_g is referred to as α in the rest of this thesis.

Equation 4.23 models the evaporation $\dot{m}_{l\to g}$, while equation 4.24 models the condensation $\dot{m}_{g\to l}$. Both $\dot{m}_{l\to g}$ and $\dot{m}_{g\to l}$ have units kgm^{-3}s^{-1}. The two *K* variables are called the evaporation and

condensation frequency, respectively. These variables are further elaborated upon in the following paragraphs.

The evaporation-condensation model is based on the Hertz Knudsen equation for the evaporation-condensation flux [18, 19]

$$F = \beta \sqrt{\frac{M}{2\pi R T_{sat}}} \left(P^* - P_{sat} \right) \tag{4.25}$$

This equation describes the flux (units kg/m^{2}s) of evaporating and condensing material as a function of the difference between the partial vapor pressure P^* on the gas side of the liquid-vapor interface and the saturation pressure P_{sat}, the saturation temperature T_{sat}, the molecular mass and the accommodation factor β. This last factor is the fraction of vapor molecules that sticks to the interface surface when hitting it. Thus, 1-β is the fraction of gas molecules that is reflected, not participating in the condensation process, but contributing to P^*. β approaches 1.0 at equilibrium conditions, but is generally not well known [15, 10, 19]. The difference between the vapor pressure and the saturation pressure can be obtained using the Clausius-Clapeyron equation, as long as both pressure and temperature are close to the saturation condition [15, 20, 21]

$$P^* - P_{sat} = -\frac{L}{T^* (v_g - v_l)} \left(T^* - T_{sat} \right) \tag{4.26}$$

Here, L is the latent heat, while v_g and v_l are the specific volume of the gas and liquid, respectively (this is just the inverse of the density). T^* is the vapor temperature. Using this relation in the Hertz Knudsen equation (4.25) yields

$$F = \beta \sqrt{\frac{M}{2\pi R T_{sat}}} L \left(\frac{\rho_l \rho_g}{\rho_l - \rho_g} \right) \left(\frac{T^* - T_{sat}}{T_{sat}} \right) \tag{4.27}$$

Where it is again assumed that the vapor temperature is close to the saturation temperature. The mixture model assumes the flow regime is dispersed, with a constant bubble diameter which has to be specified. This leads to an equation for the interfacial area per unit volume of [15]

$$\frac{A_i}{V} = \frac{6\alpha_g}{d} \tag{4.28}$$

where A_i is the interfacial area in a given volume V, α_g is the gas volume fraction in that grid cell and d is the bubble diameter. This equation is solved for each grid cell, giving the average interfacial area concentration within each grid cell. Equation 4.28 can be obtained by dividing the surface of a sphere of diameter d by its volume and multiplying by the gas volume fraction α_g.

The interfacial area concentration should be multiplied by F to obtain the volumetric source term for the gas phase, which results in

$$S_g = \frac{6}{d} \beta \sqrt{\frac{M}{2\pi R T_{sat}}} L \left(\frac{\rho_l}{\rho_l - \rho_g} \right) \left(\alpha_g \rho_g \frac{T^* - T_{sat}}{T_{sat}} \right) \tag{4.29}$$

Here, S_g is the source term for the gas phase with units $kgs^{-1}m^{-3}$. Comparing equations 4.23 and 4.29, it shows that K_{evap} is defined as

$$K_{evap} = \frac{6}{d}\beta\sqrt{\frac{M}{2\pi RT_{sat}}}L\left(\frac{\rho_l}{\rho_l - \rho_g}\right) \tag{4.30}$$

A similar derivation can be done for K_{cond}, which may theoretically result in a slightly different value for K_{cond}. Note that in the final expression and derivation, both β and d, which are not well known a priori, return. It is for this reason that it is recommended to fine tune K_{evap} to match experimental results. However, no experimental setup was available, so this is not actually done in this thesis. Instead, the influence of K_{evap} was investigated by running simulations for various values of K_{evap} (TP1).

4.4 Solution Methods

In this section, the methods used by the program to arrive at the solution are discussed. The program offers many different methods to solve the flow equations, and this section explains which ones have been chosen and the reasoning behind these choices.

4.4.1 Pressure Based Coupled Solver

Fluent gives the user the choice between a pressure based solver and a density based solver. Multiphase flows can only be modeled with the pressure based solver, so this one is chosen in this thesis. This solver has both coupled and segregated algorithms, which refers to the coupling of the momentum and continuity equations. In the segregated solvers, the momentum equations are solved before the continuity equation, while in the coupled solver, both are solved simultaneously. As a result, convergence is generally faster for the coupled solver, but the memory demand is higher as well, since more variables need to be stored. The coupled solver is chosen, because the available amount of memory was found to be sufficient and the convergence was better with this solver.

Figure 4.1 shows a schematic overview of the two algorithms in their most general form. The difference between the segregated solver and the coupled solver shows in the second and third step in the segregated solver; these are combined in one step the coupled solver. This also removes the need to update the pressure and velocity field, since the system of momentum and pressure based continuity equations are solved simultaneously.

In the simulations performed in this thesis, the flow is modeled as laminar, so turbulence is not considered. The mass flux is calculated for each cell face in the fourth/third step for the segregated/coupled algorithm, respectively.

In Fluent, interpolation schemes are used to calculate the values of flow variables at cell faces, because they are stored at the centers. For the pressure, the default standard scheme is used. This scheme makes a weighted average of the cell values of the two cells adjacent to the face, where the weight factors are the momentum equation coefficients. This scheme is computationally less costly than a staggered grid approach but renders acceptable results for most cases [15], when pressure variation between grid cells is smooth. Since the flow does not include large pressure gradients, this scheme is expected to suffice for the simulations performed in this thesis.

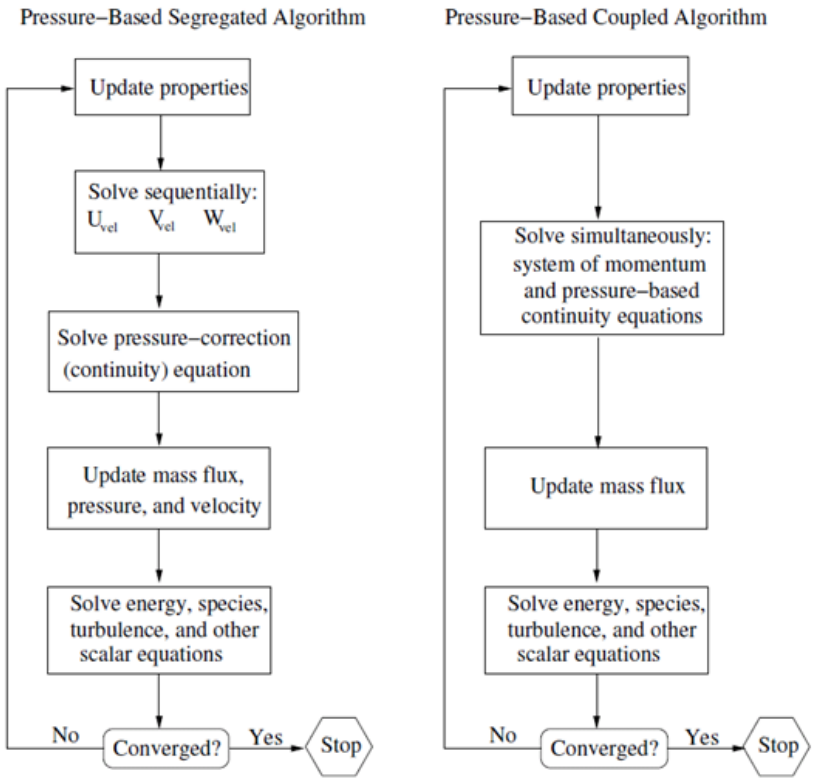

Figure 4.1: pressure based solver algorithms overview [15]. The coupled solver integrates the second and third step to speed up convergence, but this increases the memory demand since more equations need to be solved simultaneously; each variable has to be stored at the same time.

The momentum, energy and volume fraction (for the two phase simulations only) equations are spatially interpolated with the first order upwind scheme. This scheme uses the assumption that cell values hold throughout the entire cell, also on the faces. The face values are taken as the center value of the upstream cell. This scheme generally has the fastest convergence, although the accuracy for high gradients is not as high when compared the second order upwind scheme or other interpolation schemes.

The gradients of all flow variables are determined with the default least squares cell based scheme. This scheme assumes the values of the variables vary linearly. This scheme is of similar accuracy but computationally less expensive than the node based scheme, which calculates the gradient values on a face as the arithmetic average of the values at the nodes on the face.

4.4.2 Under Relaxation

Under relaxation factors are constants that stabilize the calculation by using part of the value calculated in the previous iteration in the value to be used for the next calculation. If φ is a variable and u is the under relaxation factor, this takes the following form [15]

$$\varphi_i = \varphi_{i-1} + u\Delta\varphi \tag{4.31}$$

Where $\Delta\varphi$ is the change in the variable φ as calculated by the program in the i^{th} iteration and u is the under relaxation factor, which is a number between 0 and 1. Setting u to 1 gives the full $\Delta\varphi$ as it was calculated, giving the fastest convergence. Note that a high under relaxation factor implies a low relaxation, because almost the whole change in the variable is used for the next iteration. Setting u to zero stops convergence entirely, because the flow variable cannot change between iterations.

A high under relaxation factor may induce numerical instability, because the value of φ may change too rapidly between iterations. Setting the under relaxation factor too low unnecessarily slows down convergence. The default values for the under relaxation values as set by Fluent are suitable for many cases, but for more complex flows, lower values are often needed to provide sufficient numerical stability. The value of the under relaxation factors does not influence the final solution, only the amount of iterations that is required to reach it.

4.4.3 Pseudo Transient Formulation

The pseudo transient formulation is a method of implicit under relaxation. It calculates a pseudo time step size, which is the relevant time scale, for each equation. For instance, for the momentum equation, this time step is calculated as the characteristic length divided by the maximum velocity in the domain. For the pressure equation, this expression is divided by the pressure change in the domain. The smallest time step is chosen as the time step to be applied to all equations, since the time step size within one iteration should be equal for each equation; otherwise, calculated values for different quantities in the next iteration would not occur in the same point in time [15].

The pseudo time step determines the size of the time step taken between iterations, thus the magnitude of the change in variables from iteration to iteration.

The advantage of pseudo transient under relaxation is that it adapts the under relaxation factor to the current solution. In the early iterations, the solution may be highly chaotic, causing high gradients and many irregularities that could potentially induce divergence. Here, the pseudo time step is small to increase stability. When the solution starts to become more regular and 'smoother' as more iterations are performed, the pseudo time step can increase, speeding up convergence.

To summarize, the advantage of the pseudo transient formulation is greatest for complex flow fields; the pseudo transient under relaxation is modified to suit the solution as the iterative process progresses. Therefore, for complex flow fields, where the initial solution differs greatly from the final solution, the advantage is greatest.

5 Simulation Results

In this chapter, the simulation results will be discussed. Various plots are used to gain a better insight in the flow, among which are velocity plots of the velocity magnitude and individual components, along lines as well as surfaces, in which cases contour plots are made. For the two phase simulations, the average void fraction in the frontal volume as well as the void fraction distribution is analyzed as well. Finally, the results are compared with another Cold Neutron Source at the National Institute of Standards in Technology at Boulder, Colorado.

5.1 Single Phase Results

The single phase simulations are performed for three different boundary conditions, being a set pressure difference between moderator cell inlet and outlet (SP1), a natural convection driven case where the inlet and outlet tubes were also modeled (SP2), and a set mass flow rate of 2 g/s, as specified by KHC (SP3A&B). All single phase simulations except SP3B use the preliminary design geometry and all use an open inner cavity.

5.1.1 Main Findings

The most noteworthy result of the single phase simulations is that the resulting mass flow in SP1 and SP2 (specified pressure difference and natural convection respectively, see table 4.2) is much higher than the specified 2 g/s. For SP1, the resulting mass flow is 34 g/s, while it is 13 g/s for SP2.

One would expect the mass flow rate to increase even further when two phase flow is incorporated, because the density difference between incoming and outflowing hydrogen greatly increases. However, friction effects between the two phases might counter this effect and may turn out to be stronger than the rise in driving force, actually resulting in a lower mass flow rate for the two phase simulation [22, pp. 490].

It should also be noted that the heat load estimates by KHC were used in these simulations, which are significantly higher than those found by RID (see table 4.1). For SP2, this explains partly why the mass flow is so high. In SP2, which models the natural convection, buoyancy forces drive the flow. These forces result from the temperature dependence of the hydrogen density. Increasing the heat source increases the hydrogen temperatures achieved in the frontal volume, lowering the average density in the frontal volume, increasing the buoyancy forces. This increases the mass flow rate.

An alternative way to view this effect, is that if the heat source is increased, more heat has to be removed from the moderator cell in order to maintain a steady state heat balance. Removing more heat from the moderator cell requires that the outflowing hydrogen has a larger enthalpy, or that more hydrogen flows out. In reality, it will be a little bit of both. An increase in the outflow of hydrogen directly results in a larger mass flow rate, as the mass of the content of the moderator cell is to remain constant in time in steady state operation.

In all simulations, the pressure loss due to friction in the condenser is not modeled. This loss could be substantial, which would cause the total pressure difference between the inlet and outlet of the moderator cell to be significantly smaller (see equation 3.8). This would decrease the mass flow in SP1 and SP2.

For all single phase simulations, the hydrogen temperature tends to rise to very high levels in some areas, which is to be expected, because the lack of evaporation greatly reduces the hydrogens ability to absorb heat at a given rise in hydrogen temperature. These high temperature values are unphysical, since hydrogen cannot reach those temperatures in the liquid state at the specified design pressure of 1.5 bar [9].

5.1.2 Plotting Method

To gain insight in the flow field, plots were made of various properties of the flow along a set of lines running through the frontal volume. These lines run vertically, which is parallel to the gravity vector and the supply and drain tubes (this is the x-direction in the model). Three lines are used, one near the front wall, one in the middle between the front and back wall and one near the back wall. The distance between the lines is one quarter of the frontal volume thickness, evenly distributing the lines. A schematic view of these lines in the volume is given in figure 5.1. The velocity at the bottom of the cell is investigated in a similar manner, with horizontal lines running along the bottom of the cell. The lines used are visible in figure 5.2, which also shows the lines from figure 5.1.

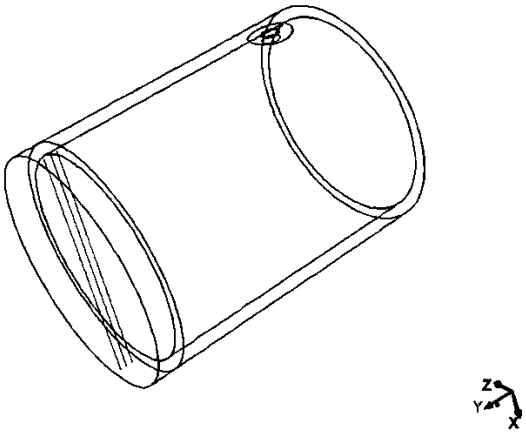

Figure 5.2: schematic image of the lines in the frontal volume along which various plots are made. There are three evenly spaced lines, running through the center of the frontal volume, at different distances from the front and back walls of the frontal volume. Again, the y-vector points towards the reactor core while the x-vector points downwards.

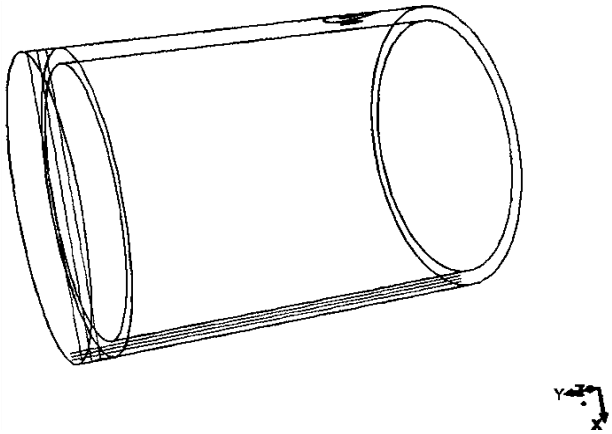

Figure 5.2: schematic image of the lines at the bottom of the moderator cell, which are used in figure 5.12. The lines from figure 5.1 are also visible in this figure. Again, there are three evenly spaced lines, at different distances from the inner and outer moderator cell walls.

In each plot hereafter, the dots are the values of the respective quantity for the mesh grid cell at the respective position. The higher density of dots around the middle is explained by the smaller grid cells near the center, which is a consequence of the way the mesh is made (see figure 3.5). In the chapter 3.2, this is seen as the small cylinder in the center of the frontal volume in figures 3.1 to 3.5. At the ends, the grid cells become smaller as well, because the line along which the plot has been made penetrates the outside layer of the flow domain, where the hydrogen flows between the inner and outer cells. The mesh (figures 3.6) clearly shows smaller grid cells here, which is done to better account for velocity gradients near the walls of the moderator cell.

5.1.3 Velocity Characteristics

First, plots of the velocity magnitude were made. These plots were made for all simulations, using the lines at z=0, as shown in figure 5.1. The results are given in figures 5.3 to 5.6. In each plot, the green dots represent the line at the reactor side of the frontal volume, the red dots represent the line running through the center and the black dots are from the line at the back.

The horizontal axis gives the x-coordinate of the cells, where a negative value represents the top of the moderator cell, and a positive value represents the bottom. This counter intuitive definition of the vertical position is a result of the way the geometry was built in the modeling program.

From the figures, it immediately shows that the overall velocity magnitude is highest in figure 5.3, which represents SP1. This makes sense, because this simulation has the highest mass flow rate (34 g/s).

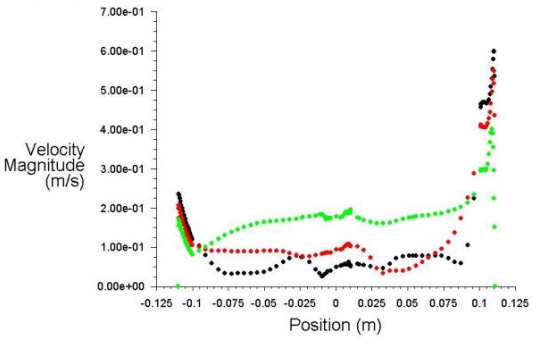

Figure 5.3: SP1 velocity magnitude in the frontal volume, along the lines shown in figure 5.1. The green dots represent the line closest to the inner cavity, the black dots represent the line closest to the reactor core (the front of the moderator cell) and the red dots stem from the line through the middle. The peaks at the edges are caused by the fact that the flow is mostly in the negative x-direction (upwards) and the flow cross section in the y,z-plane is smallest near the top and bottom of the frontal volume.

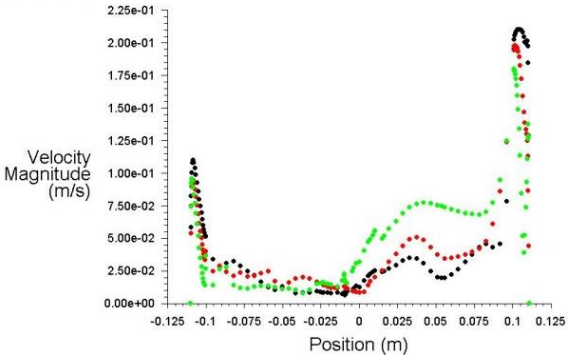

Figure 5.4: SP2 velocity magnitude in the frontal volume, along the lines shown in figure 5.1. The horizontal axis in these figures shows the position along the lines from figure 5.1, which is the x-coordinate. The top of the frontal volume is on the left, the bottom is on the right. The center is at x=0.

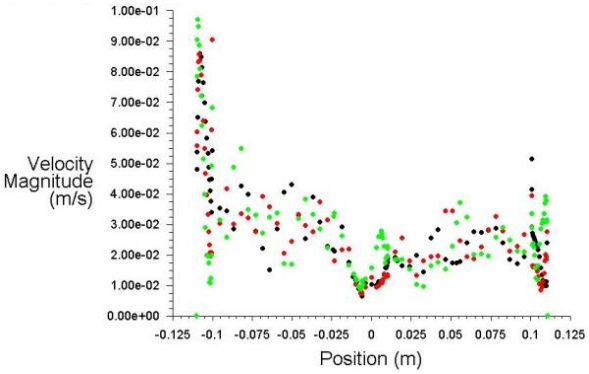

Figure 5.5: SP3A velocity magnitude along the lines from figure 5.1. Note that the flow velocities are much lower in figures 5.5 and 5.6 than in figures 5.3 and 5.4, which is due to the lower mass flow rate of simulations SP3A and SP3B when compared to SP1 and SP2.

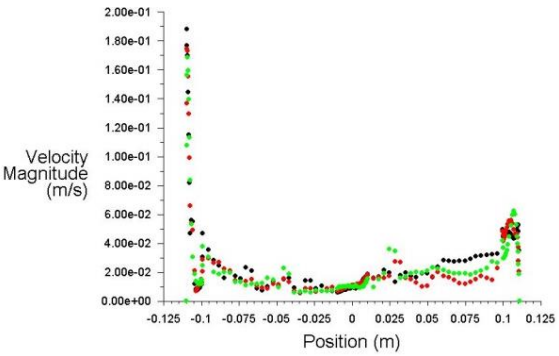

Figure 5.6: SP3B velocity magnitude along the lines from figure 5.1.

The Reynolds number in the frontal volume was calculated for each simulation, according to equation 5.1. The values used in this calculation and the results are given in table 5.1. The velocities and densities used are mass averaged values in the frontal volume, as calculated by Fluent ($\langle v \rangle$ and $\langle \rho \rangle$, respectively). The length scale used is the thickness of the frontal volume (D_{fv}) and the viscosity μ is the same for all cases, being the viscosity of liquid hydrogen at saturation conditions.

$$\mathrm{Re}_{fv} = \frac{\langle \rho \rangle \langle v \rangle D_{fv}}{\mu} \tag{5.1}$$

Table 5.1 shows relatively large Reynolds numbers for all single phase simulations, although the flow in the advanced geometry (simulation SP3B) is not very far off from laminar flow according to the Reynolds number. Nevertheless, the Reynolds numbers show that the laminar model was probably not accurate in modeling these flows, especially in the cases where the mass flow rate was not specified (figures 5.3 and 5.4, simulations SP1 and SP2). These cases had a much higher mass flow rate than was expected, which caused the density to rise as well, since the hydrogen did not rise in temperature very much due to the short time a hydrogen molecule spends in the moderator cell. Both these effects raise the Reyolds number considerably.

simulation	figure #	density (kg/m^3)	viscosity (kg/ms)	length (m)	velocity (m/s)	Re
SP1	5.3	67	$1.2006*10^{-5}$	0.06	0.11	$3.7*10^4$
SP2	5.4	65	$1.2006*10^{-5}$	0.06	0.042	$1.4*10^4$
SP3A	5.5	45	$1.2006*10^{-5}$	0.06	0.035	$7.9*10^3$
SP3B	5.6	51	$1.2006*10^{-5}$	0.025	0.032	$3.4*10^3$

Table 5.1: Reynolds number calculation. The density is taken as the mass weighted average density in the frontal volume, while the same is done for the velocity. The length scale used is the thickness of the frontal volume. Note that all Reynolds numbers indicate turbulent flow, which implies the laminar solving approach is not entirely valid for this application. Including turbulence would increase friction, reducing the mass flow rate and average velocity in SP1 and SP2, as the mass flow rate is not included in the boundary conditions in these simulations.

Figures 5.3 to 5.6 show relatively large velocities at the top and bottom of the cell. Figures 5.7 to 5.10 show that the y-velocity goes to large absolute values in these areas. The top and bottom are where the majority of the flow respectively leaves and enters the frontal volume, which implies flow in the y-direction. This is believed to be the main cause of the increase in velocity magnitude at the top and bottom of the cell.

In figures 5.7 to 5.10, the y-component of the velocities has been plotted, along the same vertical lines as in figures 5.3 to 5.6. Here, a positive y-component of the velocity means the fluid is moving towards the front of the frontal volume (parallel to the neutron beam tube), which is the reactor side of the moderator cell. This is expected at the bottom of the moderator cell, which is at large positive x-coordinates. The opposite is to be expected for large negative x (the top of the moderator cell). At x-coordinates that are relatively far from the top and bottom, the y-component of the velocity is expected to be around zero. Both these trends are indeed visible in figures 5.7 to 5.10.

Comparing the figures shows that figure 5.9 is much more irregular than the other three figures. In the aforementioned set of plots (figures 5.3 to 5.6), a similar statement could be made for figure 5.5. This leads to the presumption that the flow is more irregular in this case than in the other cases. It is speculated that this is due to the fact that the overall variation in velocity magnitude is lowest for this simulation, which means the pressure loss due to friction is low. The buoyancy forces, however, are not directly influenced by the velocity, so they become relatively more dominant at low average flow velocities, which changes the flow dynamics.

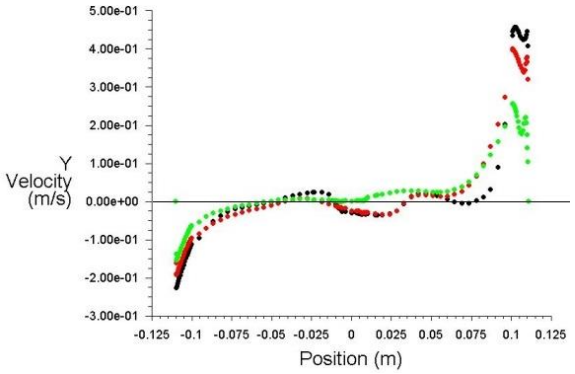

Figure 5.7: SP1 y-velocity in the frontal volume, along the lines from figure 5.1. Note that the y-velocity, which is the velocity parallel to the neutron beam, should be around zero for intermediate values of x (the coordinate parallel to the inlet and outlet tubes and the gravity vector). This is indeed the case in figures 5.7 to 5.10. Also note the generally positive y-velocities for large positive x and the negative y-velocities for large negative x, which means the fluid moves towards the reactor core at the bottom of the moderator cell (positive x) and away from it at the top of the moderator cell (negative x).

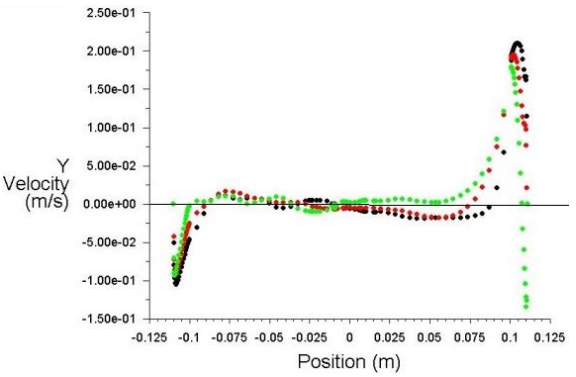

Figure 5.8: SP2 y-velocity in the frontal volume, along the lines from figure 5.1. The y-velocity is the component of the velocity that is parallel to the neutron beam, with the positive direction pointing towards the reactor.

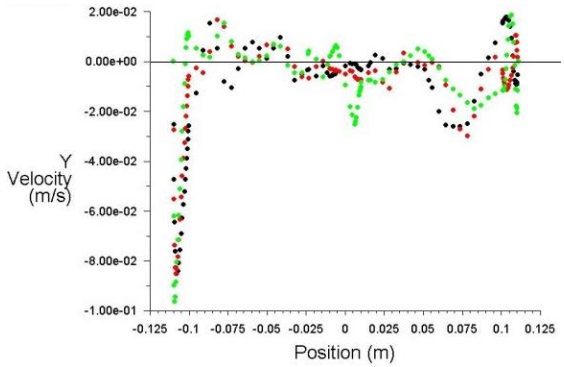

Figure 5.9: SP3A y-velocity.

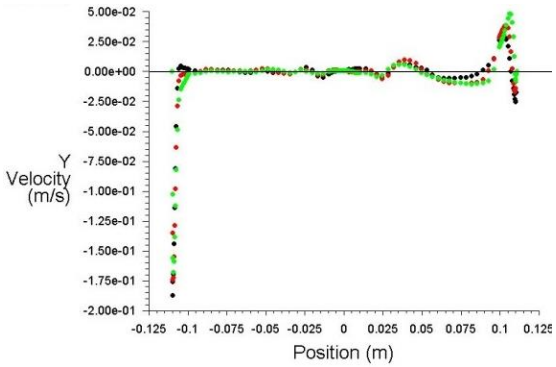

Figure 5.10: SP3B y-velocity. Note that the velocity magnitudes in this figure are significantly higher than in figure 5.9. The explanation behind this lies in the fact that the frontal volume is narrower in simulation SP3B than it is in SP3A, while the mass flow rate is equal.

It can be seen from the figures that the trends in the y-velocity (parallel to the neutron beam) outlined above are present in all simulations. However, at the very end of the positive x-axis (the bottom of the moderator cell), the y-velocity suddenly becomes negative (flow moves away from the reactor core) in figures 5.8, 5.9 and 5.10. A possible explanation is that the flow mainly enters the frontal volume from the lower part of the moderator cell. The hydrogen flows into the frontal volume and collides with the outer moderator shell at the front face of the cell. Here, the hydrogen spreads along this face, but hydrogen which flowed down along the face has nowhere to go but back in the negative y-direction. As a result, backflow would occur at this location. A schematic view of what this might look like is given in figure 5.11.

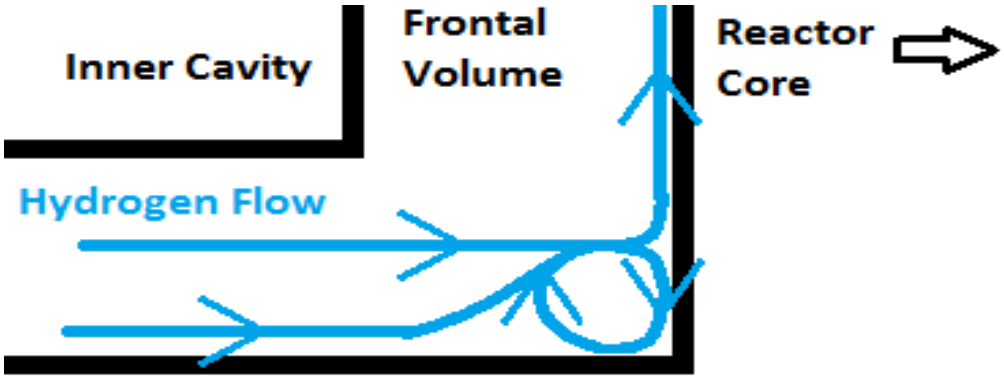

Figure 5.11: schematic depiction of vortex region at the bottom of the frontal volume. The figure shows a cross section of the moderator cell, zoomed in on the lower part of the frontal volume. The blue lines represent possible hydrogen streamlines, which show that hydrogen that is stopped by the frontal wall of the frontal volume spreads upwards and downwards. The downward flow must turn right upon reaching the bottom of the vessel, causing it to flow back, away from the reactor core. This hydrogen then meets hydrogen flowing into the frontal volume nearer to the bottom of the moderator cell, pushing both upwards. Since this schematic drawing only incorporates two incoming streamlines, the shape of the vortex differs from what is observed in figure 5.16. The upper streamline, that splits into an upward and downward part, is actually pushed upwards by the vortex, creating a roughly triangularly shaped cross section of the vortex.

To investigate the validity of this claim, plots are made of the y-velocity along a set of lines that run through the bottom of the moderator cell, as depicted in figure 5.2. The z-component of all lines is zero, so the lines run along the symmetry plane (which is the x,y-plane at z=0) of the moderator cell. A set of three lines is made, with one running through the middle of the space between the shells and the other two a quarter of the distance between the shells above and below, respectively. This is done for simulation SP3B only. This simulation bears the most resemblance to the two phase simulations (see table 4.2), because it is the only single phase simulation that uses the advanced geometry. Figure 5.12 shows this plot.

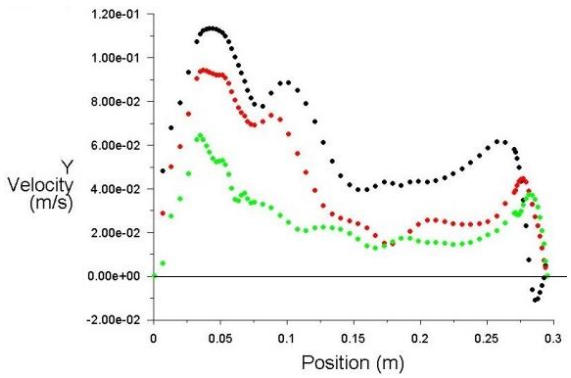

Figure 5.12: SP3B y-velocity near the bottom of the moderator cell. The black dots represent the lowest line, the red dots represent the middle line and the green dots represent the highest line. Note that the y-velocity becomes negative for large x for the black dots only, which means the fluid in the frontal volume moves away from the reactor core near the very bottom of the moderator cell, although the fluid generally moves toward the reactor core in the lower part of the moderator cell.

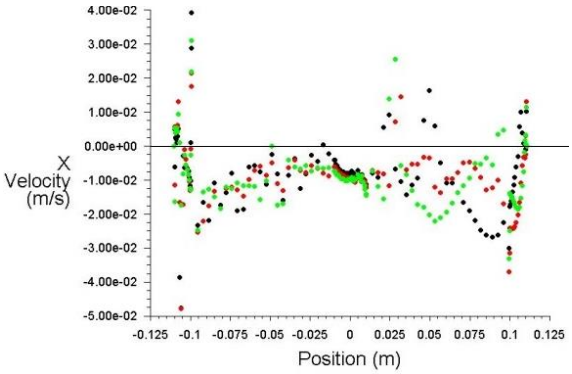

Figure 5.13: SP3B x-velocity in the frontal volume, along the lines from figure 5.1. Note that it becomes positive in certain areas, , implying downward flow.

In figure 5.12, the black dots represent the y-component of the velocity at 2.75 mm from the outer shell, the red dots are the results from the line in the middle, that is at 5.50 mm from the outer shell, and the green dots represent the line at 8.25 mm from the outer shell. A large y-coordinate

represents a close proximity to the reactor side of the vessel, so a positive y-component of the velocity means the fluid is moving towards the reactor end of the vessel. The black dots show that only very close to the bottom of the frontal volume, the fluid is flowing in the negative y-direction. This supports the given theory that a vortex like region occurs here. In order for a vortex to be present, the x-component of the velocity must also be pointing downwards (in the positive x-direction, that is); a vortex rotates in a plane, so two velocity vectors need to point in the direction opposite the trend. Figure 5.13 shows this is indeed the case: at large x, the x-velocity becomes positive. This indicates fluid moving downwards at the bottom of the cell.

Figures 5.14 and 5.15 show the vortex more clearly by means of contour plots of the x- and y-velocity on a cross section through the center of the moderator cell, in the x,y-plane. Not the entire cell is shown, only the frontal volume and part of the rest of the moderator cell. Figure 5.16 shows a vector plot of the lower right corner of these two plots, where the vortex is located.

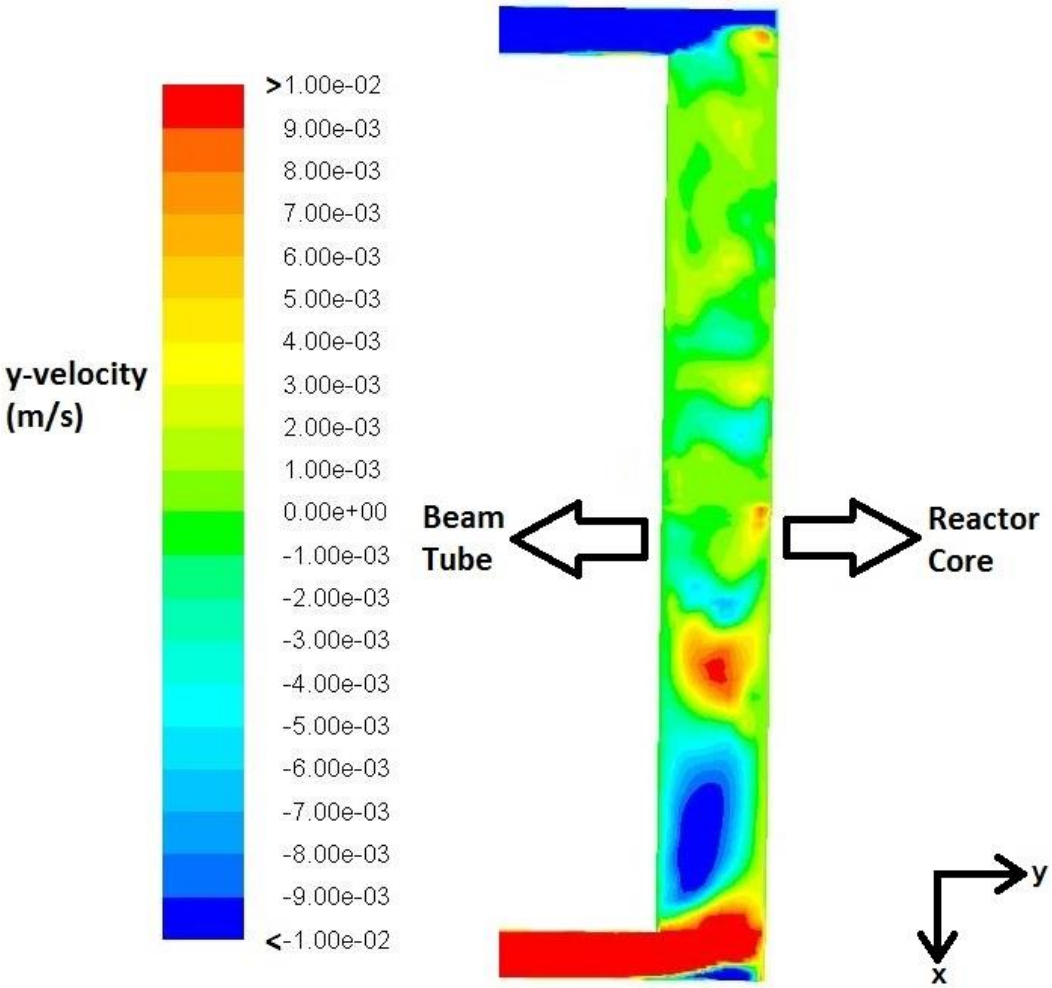

Figure 5.14: contours of y-velocity on the central cross section through the frontal volume. Red areas indicate positive y-velocities, which means the fluid flows towards the reactor, which is to the right in the figure. Blue areas indicate negative y-velocities, which means the fluid flows towards the beam tube, which is to the left in the figure. At the bottom right, a blue area is visible, surrounded by red. This indicates a region where the fluid moves away from the reactor core, even though most of the fluid in the lower part of the frontal volume moves towards the reactor core as it flows into the frontal volume with a positive y-velocity. Near the top right, a small orange area is observed, which means fluid moves towards the reactor core in that area, even though most of the fluid in the upper part of the frontal volume moves away from the reactor core as it flows out of the frontal volume with a negative y-velocity. Just above the inflow into the frontal volume, a large blue area is seenm which could indicate a vortex as well.

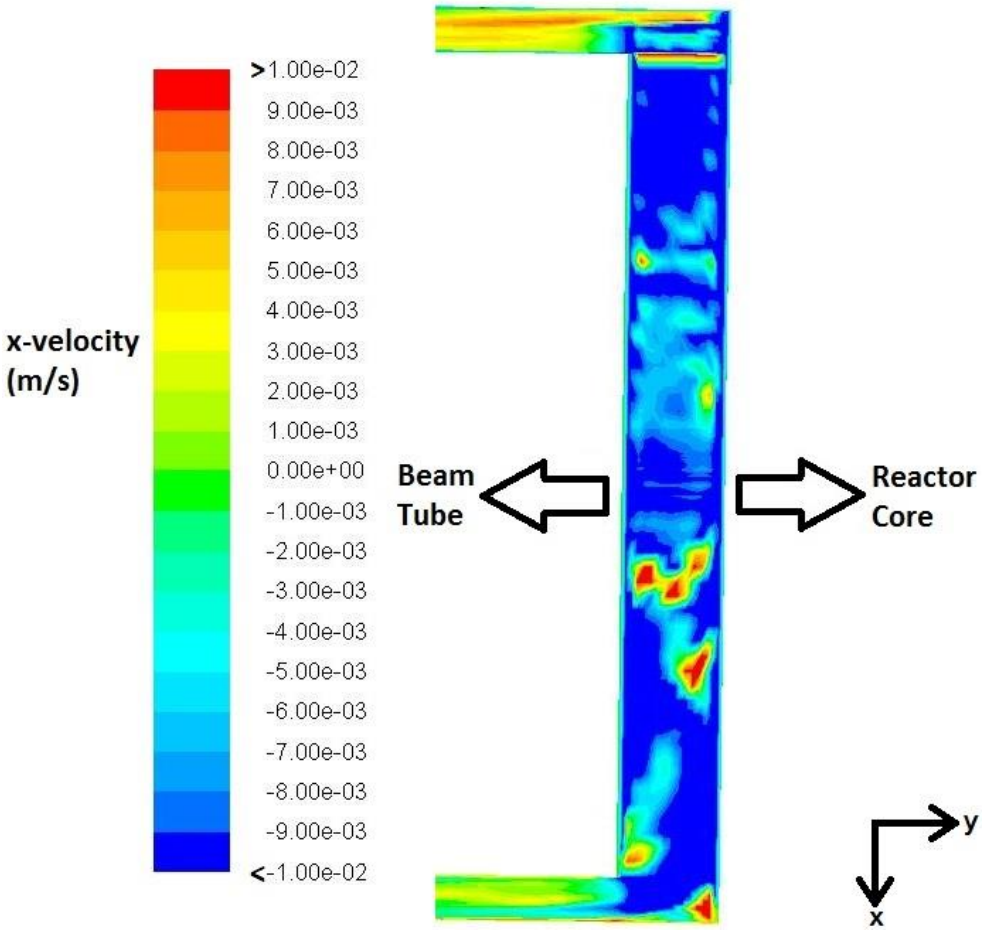

Figure 5.15: contours of x-velocity on the central cross section through the frontal volume. Red areas indicate positive x-velocities, which means the fluid is flowing downwards. Blue areas indicate negative x-velocities, which means the fluid is flowing upwards. Note that a red area can be seen in the lower right, which means the fluid is flowing downwards even though the general flow direction in the frontal volume is upwards. Combined with the blue area in the lower right corner of figure 5.14, this shows a vortex region in this area. Note also the small orange area just above the inflow into the frontal volume. Combined with the large blue area in figure 5.14 in this same location, this indicates a vortex region.

Furthermore, it is observed that the y-velocity of the flow is generally higher towards the bottom of the moderator cell. This is to be expected, as the fluid at the bottom is furthest from the fluid at the top of the moderator cell, which moves the other way, towards the outlet. Thus, a gradient in the y-velocity is to be expected, where the y-velocity ranges from having a negative value (fluid moving away from the reactor core) near the top of the vessel to a positive value (fluid moving towards the reactor core) near the bottom. This is depicted in figure 5.17, where a contour plot is made of the y-velocity.

Figure 5.17 shows that the y-component of the velocity is generally positive in the lower half of the cell, while it is generally negative in the upper half. This means the fluid moves towards the reactor in the lower part, rises in the frontal volume and moves back to the outlet in the upper part of the cell.

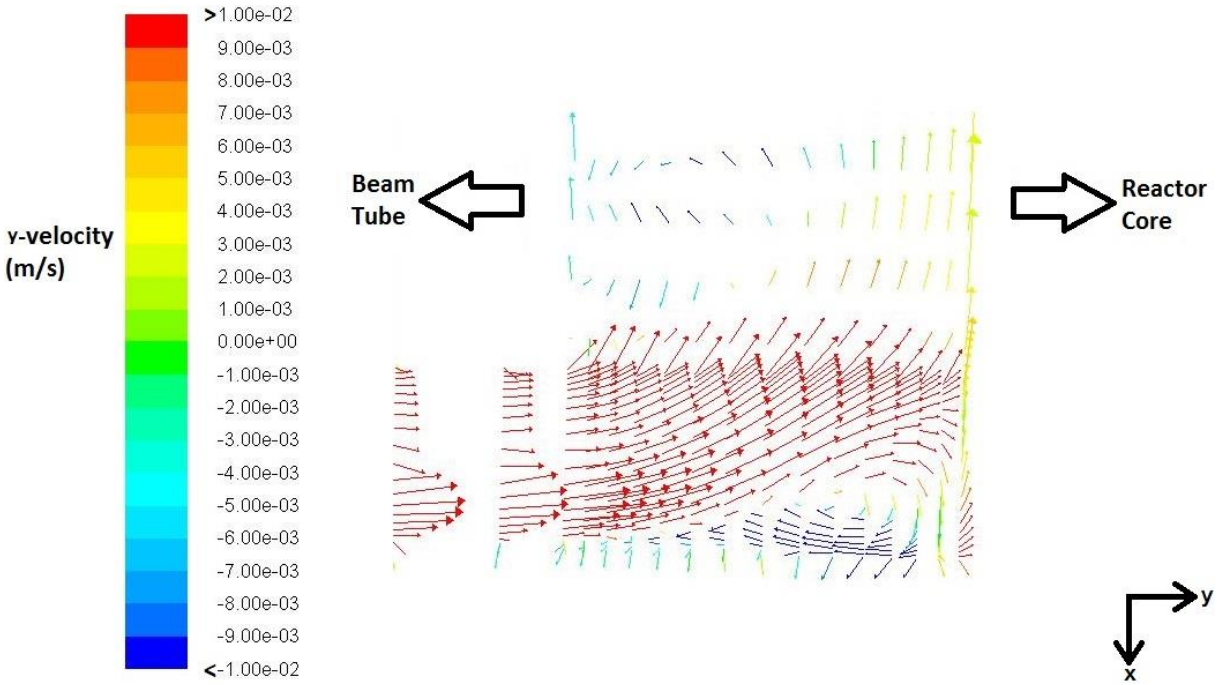

Figure 5.16: vector plot on the central cross section through the frontal volume, zoomed in on the lower right corner in figures 5.14 and 5.15. The vectors represent the flow direction, they are colored for the y-velocity. Note that the lower right area indeed shows a vortex, as is described above. The upper left in this figure faintly shows a vortex as well, which is indeed as expected from figured 5.14 and 5.15.

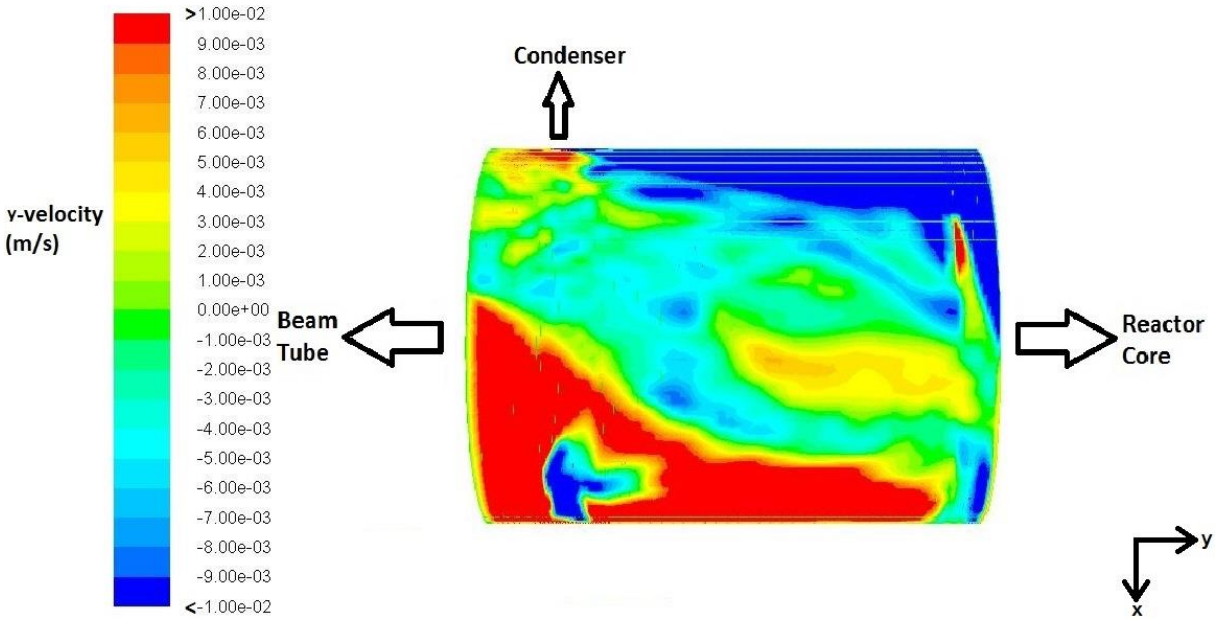

Figure 5.17: contour plot of y-velocity of the whole volume of the moderator cell. The cell is viewed from the side, so the contours are of the cells adjacent to the outer cell wall. A positive y-velocity means that the fluid moves towards the reactor core, which is to the right in this figure. Note that in the upper right, the fluid generally moves away from reactor core, while it generally moves towards reactor core in the lower left. The narrow, horizontal green lines in the upper area are artifacts, as are a the green dashes in the lower left area. Note the blue area in the lower left area; this is an area of leftward flow, surrounded by rightward flow. The middle right shows an orange/yellow area, surrounded by light blue, which indicates an area of rightward flow surrounded by leftward flow. Both of these areas might exist due to vortices or due to lack of convergence of the solution.

Now that sufficient insight is gained in the single phase flow, it is interesting to compare the flow with the two phase flow, which is discussed in the next section. The flow velocities would have a larger range in the two phase case, because the density differences are much larger. The absolute values of the velocities reached are also expected to be higher, because a larger volume has to be

removed from the cell at the same mass flow rate. All two phase simulations include use a set mass flow rate. The Reynolds number is defined as

$$\mathrm{Re} = \frac{\rho v D}{\mu} \tag{5.2}$$

And the mass flow rate φ_m is defined as

$$\varphi_m = vA\rho \tag{5.3}$$

Where A is the cross sectional area through which the fluid flows. Using equation 5.3 in equation 5.2 yields

$$\mathrm{Re} = \frac{\frac{\varphi_m}{A} D}{\mu} \tag{5.4}$$

Which shows that the Reynolds number depends on the mass flux φ_m/A only, not on v and ρ separately. Therefore, the net effect in the Reynolds number of the density decrease and the speed increase is expected to be zero, so typical Reynolds numbers should maximally increase by a factor of approximately 7.5 at equal mass flow rate, since this is the ratio between the viscosities of liquid and gaseous hydrogen (see Appendix A, table A.1; μ_l=1.2$*$10^{-5} kg/ms, μ_g=1.6$*$10^{-6}). The spatial separation between incoming and outgoing fluid should be more prominent as well because of this same increase in density difference.

5.2 Two Phase Results

In the two phase simulations TP1 and TP2, the influence of two variables is investigated. In TP2, the influence of the mass flow rate is investigated while in TP1, the influence of the evaporation and condensation frequency is investigated. The results of these simulations will be presented in a similar fashion as the single phase results. Since the main objective of the two phase simulation is to examine the void fraction distribution, plots of these values are used.

5.2.1 Velocity Characteristics

One trait that is present in both two phase simulations performed in this thesis, is that there is no difference in velocity between the two phases, even though the option ‘slip velocity’ was enabled. The slip velocity is not calculated because interphase drag is disabled in order to achieve numerical stability, as described in section 4.3.1. Thus, the mixture model is essentially reduced to a homogenous multiphase model, where both phases (gas and liquid) have the same velocity. To investigate the flow field, similar velocity plots were made as in the single phase simulations (figures 5.3-5.10). Firstly, the z-velocity is investigated in the frontal volume. This the velocity component perpendicular to both the neutron beam and the hydrogen inlet and outlet tubes. The z-velocity is of particular interest, because this should be zero along the center line of the frontal volume (i.e. at z=0) as the flow is symmetric. Figure 5.14 shows this plot. This and all other plots in this section are made for TP2 with a mass flow rate of 2 g/s, since this is the value for the mass flow rate as specified in the KHC design. The evaporation/condensation frequency is left at the default value in this section.

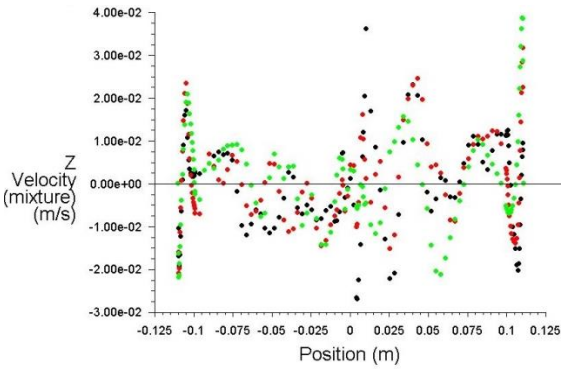

Figure 5.18: z-component (perpendicular to neutron beam and hydrogen inlet/outlet tubes) of the mixture velocity in the frontal volume along lines at z=0. Again, the green dots represent the frontmost line, the red dots represent the middle line and the black dots represent the line furthest from the reactor core.

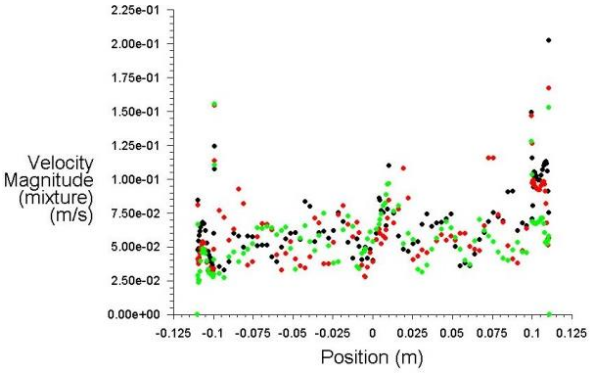

Figure 5.19: velocity magnitude at z=0. Note that the velocity magnitude is of comparable size to the z-velocity in some areas (see figure 5.18).

From figure 5.18, the z-velocity whows to be irregularly distributed. Comparing this graph to the velocity magnitude for this flow rate, as shown in figure 5.19, shows the z-component of the velocity is of significant size with respect to the velocity magnitude in some areas. This means the variation in z-velocity cannot be neglected, but has a significant impact on the flow field.

Examining figure 5.18 more closely shows that the z-component of the velocity reaches large negative values at the top (large negative x-component) and large positive values at bottom of the moderator cell (large positive x-component). This seems logical because the velocity magnitude in these areas is large as well, as can be seen in figure 5.19. However, around x=0 (the middle of the moderator cell in the vertical direction), the z-component at the back of the frontal volume (small y-coordinate i.e. furthest from the reactor core; the black dots) jumps to extreme values, which might indicate a vortex region. This is the region of the cell that has a relatively irregular mesh, as can be seen in figure 3.5. In a physically correct solution, however, the mesh should not influence the flow; the solution should be independent of the mesh.

Looking at the green dots in figure 5.14, it can be seen that, for large x (the lower part of the frontal volume), there are few jumps in the z-velocity along this line. This plot has been isolated in figure 5.20.

The presence of regions of both positive and negative z-velocities, especially for large x, indicates the possibility of vortex regions in the lower part of the cell. This may be caused by the same mechanism that causes the negative y-velocity in figure 5.12. The flow coming into the frontal volume at the bottom of the cell is stopped by the front wall and disperses in all directions along this wall (i.e. x and z). Small asymmetries then cause vortices, rotating in the x,z-plane, which is the plane of the front and back walls of the frontal volume. In order for these vortices to exist, the x-velocity must also become positive (fluid moving downwards), which is shown to be the case in figure 5.21. The average x-velocity, however, remains negative, so the fluid as a whole will keep moving upwards, transporting the vortices. This implies transient flow, as the vortices move through the flow domain. This could pose problems, because the flow is assumed stationary in the simulations performed in this thesis.

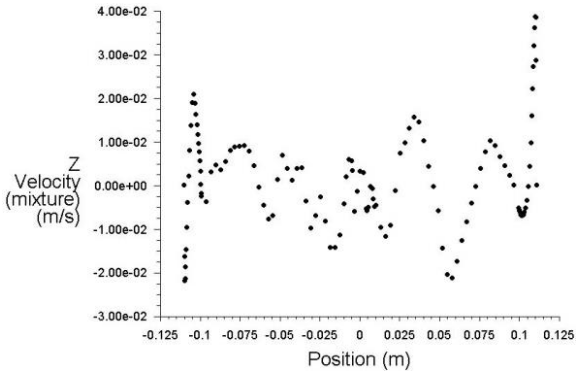

Figure 5.20: z- velocity in the frontal volume at z=0 for the line from figure 5.14 which is closest to the reactor core. Note that there are identifiable regions of positive and negative values.

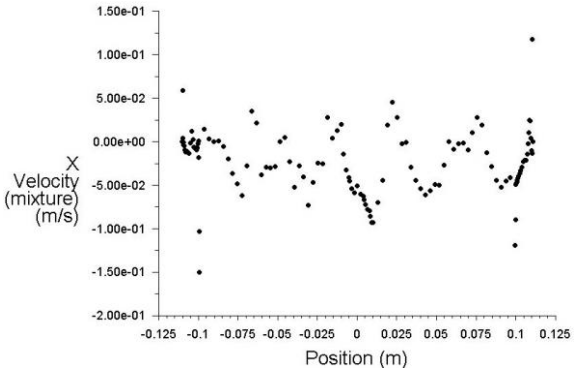

Figure 5.21: x- velocity in the frontal volume at z=0 for the line from figure 5.16. Note that the average x-velocity is negative (upward flow), but that regions of downward flow are also present.

To get a clearer image of the flow, figures 5.22 and 5.23 show contour plots of the y- and x-velocity, respectively, on the x,z-plane that contains the line used to plot figures 5.20 and 5.21. The position and orientation of this plane is shown in figure 5.24.

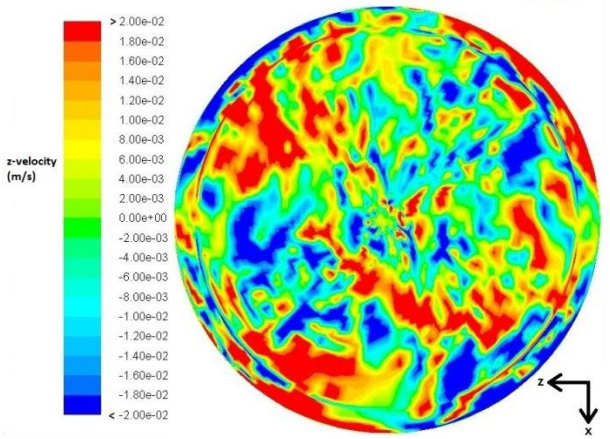

Figure 5.22: contour plot of the z-velocity on the plane shown in figure 5.20. The positive z-direction is to the left. Note that there are many small regions of positive and negative z-velocity. This indicates an irregular flow field.

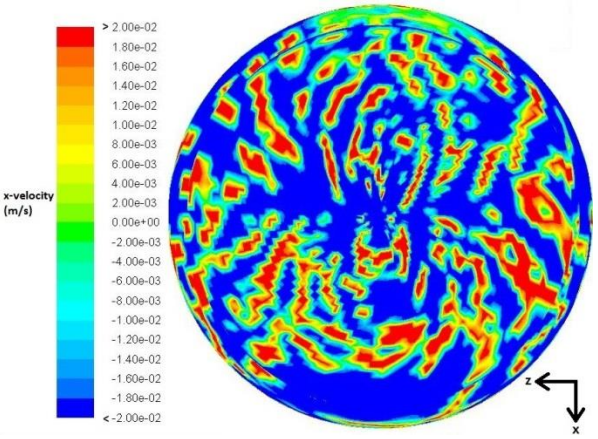

Figure 5.23: contour plot of the x-velocity on the plane shown in figure 5.20. The positive x-direction is downwards. Note that there are many regions of upward flow (red areas), even though the general flow direction in the frontal volume is upwards.

Figure 5.22 shows that many small areas of positive and negative z-velocities (fluid moving to the left and to the right, respectively) exist. Furthermore, figure 5.23 shows many areas of downward flow (the red areas), even though the fluid in the frontal volume moves upward on average as it is heated by neutron moderation and heat transfer from the front and back walls of the frontal volume. The irregular distribution of x- and z-velocities seem to indicate that the flow is not fully converged, since the situation shown in figures 5.22 and 5.23 is not expected to be stable.

To verify whether the solution obtained is converged, the program is set to run another 30 iterations before making the same plot as in figure 5.20. This plot is shown in figure 5.25. During these 30 iterations, the residuals and other convergence criteria did not change significantly nor with a trend.

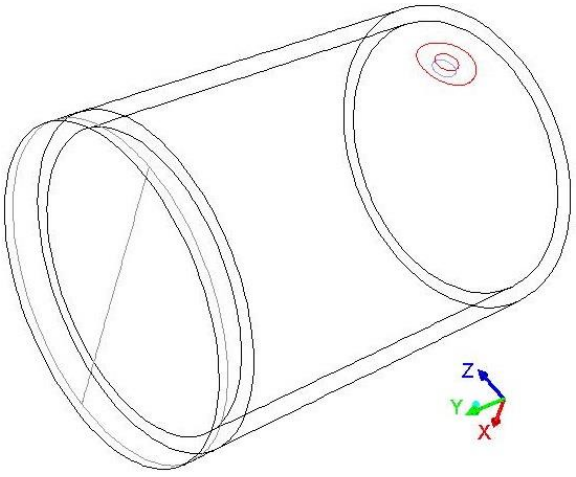

Figure 5.24: location of the plane used in figures 5.22 and 5.23. The line used in figures 5.20 and 5.21 is shown as well. The reactor core would be on the lower left, the neutron beam tube would start in the upper right corner.

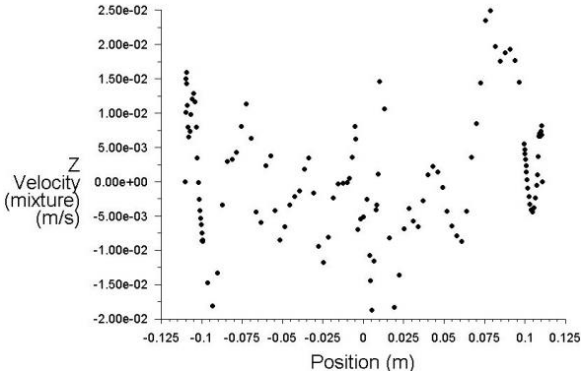

Figure5.25: z- velocity at the front at z=0, after 30 more iterations. Note that this plot differs from the plot given in figure 5.20, even though they should be the same for a converged, steady state solution. This shows that the solution is not converged.

Comparing figures 5.20 and 5.25 immediately shows they are not the same, although they should be, (approximately) identical in a converged solution. This means the flow changed in 30 iterations, although the convergence criteria and residuals did not change significantly. This means the solution obtained is not converged; i.e. the solution changes with additional iterations. In fact, this could already be seen when looking at the convergence criteria more closely; they never quite reach a constant value but keep oscillating around some fixed value. In effect, figures 5.20 and 5.25 demonstrate that a converged solution for two phase flow is not achieved in this simulation (TP2 with 2 g/s mass flow rate). Plots for the convergence criteria and the residuals for this simulation can be found in Appendix C.1.

To check whether the lack of a converged solution is caused by the fact that the problem is highly symmetrical with a relatively coarse mesh, the symmetry is broken by imposing a z-component to the inlet velocity of two thirds the x-component. This way, the flow is no longer symmetric with respect to the x,y-plane. This, however, did not make a significant change in the iterative development of the convergence criteria, as can be seen in the plots in Appendix C.2. The only noticable effect is that the average void fraction in the frontal volume decreases by about 0.2 percentage points (figure C.8).

It is possible that convergence is not achieved, because the program assumes the flow to be time-independent, while in physical reality, a time-independent physical solution might not actually exist because of the moving vortices decscribed above. Another possible explanation is that the mesh quality is insufficient.

5.2.2 Mass Flow Rate Influence on Average Void Fraction (TP2)

Reynolds Number Analysis

In TP2, the mass flow rate is varied between 1 g/s and 6 g/s. As the velocity in the frontal volume is expected to be highest in the 6 g/s case, this simulation is chosen to calculate the Reynolds number in the frontal volume. The other simulations are expected to have lower Reynolds numbers. The calculation for the Reynolds number is done by taking the average values of the flow variables in the frontal volume, which can be calculated by Fluent. The relevant values are summarized in table 5.2.

average density (kg/m^3)	34
average viscosity (kg/ms)	$6.6*10^{-6}$
length (m)	0.025
average velocity (m/s)	0.075
Re	$9.7*10^3$

Table 5.2: Reynolds number calculation for TP2 with a mass flow rate of 6 g/s, which is the highest mass flow rate that is used. The same method as in table 5.1 is used for the calculation of the Reynolds number, using mass averaged values of the flow variables.

The calculated Reynolds number for the 6 g/s simulation is too high for a laminar flow to occur, so higher flow rates can certainly not be described accurately with the laminar solver. Although the flow should be turbulent for this flow rate and other high flow rates, this simulation is incorporated in the results in order to gain a better understanding of the trend of the void fraction when the mass flow is varied.

To check the size of the smallest eddies, the Kolmogorov length scale can be used. This scale is determined by the following equation [23]

$$\eta = \frac{D}{\mathrm{Re}^{3/4}} \tag{5.5}$$

Where D is the scale of the flow which is used in the Reynolds number and η is the Kolmogorov length scale. In TP1 and TP2, D is 2.5 cm, which is the width of the frontal volume. The Kolmogorov length scale describes the size of the smallest eddies. Is the size of the mesh grid cells is below this scale, the flow can be fully resolved and turbulence modeling is not necessary for turbulent flows. If the mesh grid cells are too big, turbulence modeling is required.

Equation 5.5 leads to a Kolmogorov length scale of 26 µm, which means the smallest turbulent eddy in the frontal volume is on the order of 26 µm. To fully resolve the flow, the mesh grid cells need to be at or below this size. This is well below the size of the numerical cells in the frontal volume, since there are 15 layers of mesh grid cells between the front and back walls of the frontal volume, which are 2.5 cm apart (see figure 3.5). This makes for an average cell width of 1.7 mm in the y-direction, which is the direction of the neutron beam. As this is a factor 65 larger than the Kolmogorov length scale calculated above, the flow is not fully resolved. Note that, since the cells near the walls are smaller than the cells further from the walls, as can be seen in figure 3.4, the largest cells in the frontal volume are significantly larger than the average size.

For the TP2 simulation with a mass flow rate of 1 g/s, which is the lowest mass flow rate that is used in the simulations performed in this thesis, the Reynolds number in the frontal volume is $5.6*10^3$, calculated in the same way as for the 6 g/s simulation above. This results in a Kolmogorov length scale of 39 µm, which is still well below the average cell width in the frontal volume. As the single phase simulations all have Reynolds numbers of similar or larger size, it can be concluded that none of the simulations performed in this thesis have a sufficiently fine mesh to fully resolve the flow.

Average Void Fraction

Table 5.3 and figure 5.26 show the volume averaged void fraction in the frontal volume as a function of the mass flow rate. In Figure 5.26, α denotes the volume averaged void fraction in the frontal volume and φ denotes the mass flow rate in units g/s. The equation derived is forced to yield α=1 at φ=0, since the void fraction would go to 1 if the mass flow rate would go to zero. The given equation is only valid in the given domain, since it is empirically derived. An exponential function is chosen to fit the data points, because it is expected the void fraction goes to zero as the mass flow rate goes to infinity. The fitted equation shows that the volume averaged void fraction in the moderator cell varies nearly linearly with the mass flow rate in the given domain; in fact, a linear fit can also be applied, which is still fairly good with an R^2 value of 0.99. the amount of data points, however, is too little to arrive at solid conclusions with regard to the actual correlation between φ and α.

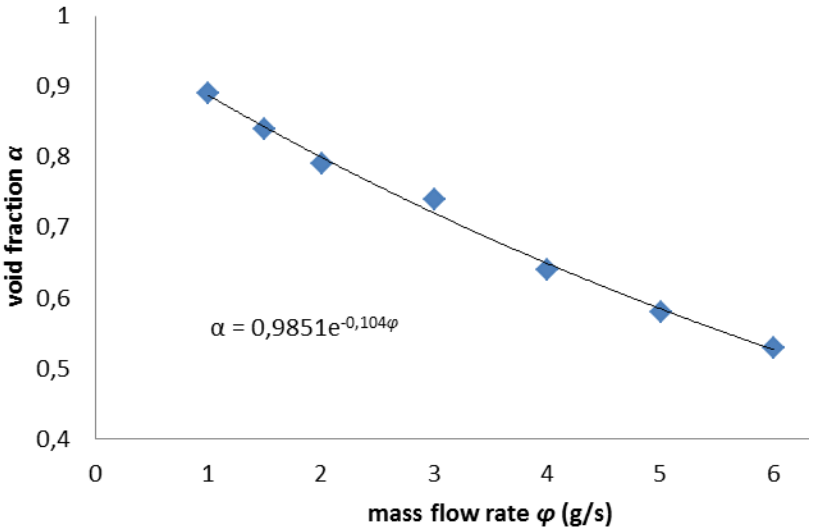

Figure 5.26: volume averaged void fraction as a function of mass flow rate. This figure is a plot of the data from table 5.3.

flow rate (g/s)	void fraction
1	0.89
1.5	0.84
2	0.79
3	0.74
4	0.64
5	0.58
6	0.53

Table 5.3: average void fraction in the frontal volume for different mass flow rates.

It is obvious from the figure that the average void fraction declines as the mass flow rate rises. This is due to the fact that the vapor production cannot rise with the mass flow, because the supplied heat remains the same.

A higher mass flow implies higher fluid velocities, decreasing the vapor retention time, which is the time a hydrogen molecule spends inside the moderator cell. If the vapor production is not raised but the retention time is decreased, the amount of vapor in the moderator cell at any time is decreased, because all hydrogen molecules, including the evaporated ones, spend less time in the moderator cell. This decreases the average void fraction in the moderator cell. The same goes for the frontal volume, which is what explains the trend that α drops with increasing φ.

5.2.3 Void Fraction Distribution in TP2

The plots of the void fraction along the same lines as those used in section 5.1 are given in figures 5.27 to 5.33. Appendix D includes similar plots, plotted along lines that are side by side in the frontal volume (with varying z instead of y). These show a similar trend, without much deviation from one line to another.

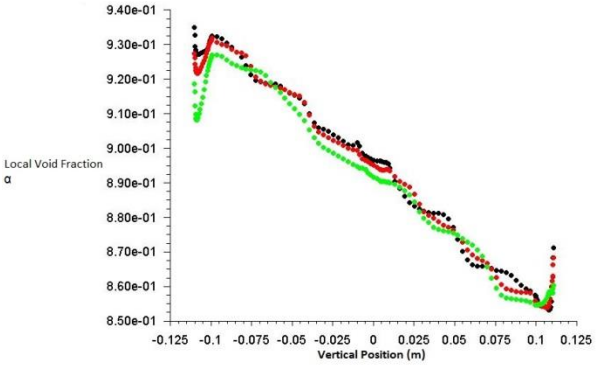

Figure 5.27: 1 g/s void fraction distribution along vertical lines running through the frontal volume. The green dots represent the line at the front, the red dots represent the line in the center and the black dots represent the line at the back of the frontal volume, which is furthest from the reactor core. These lines are shown in figure 5.1.

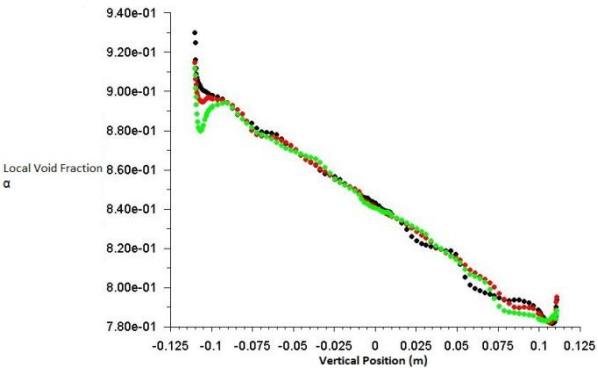

Figure 5.28: 1.5 g/s void fraction distribution. Note that downwards is again the positive direction, so the top of the moderator cell is on the left hand side while the bottom is on the right hand side in figures 5.27 to 5.33.

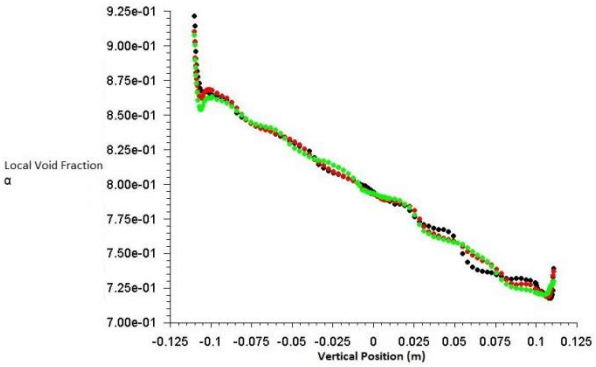

Figure 5.29: 2 g/s void fraction distribution.

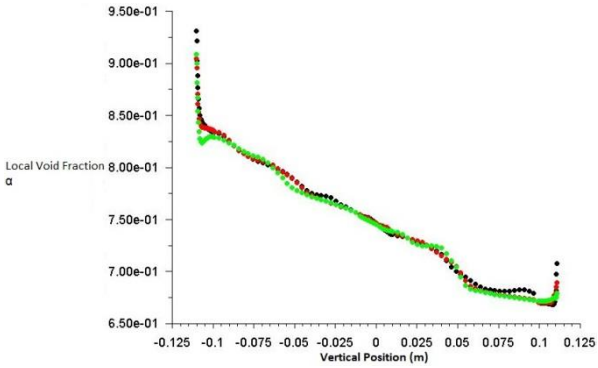

Figure 5.30: 3 g/s void fraction distribution.

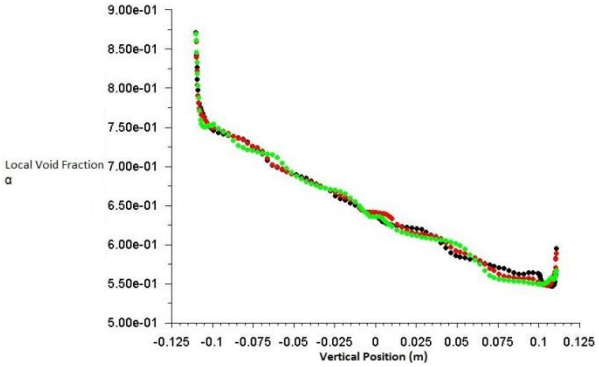

Figure 5.31: 4 g/s void fraction distribution.

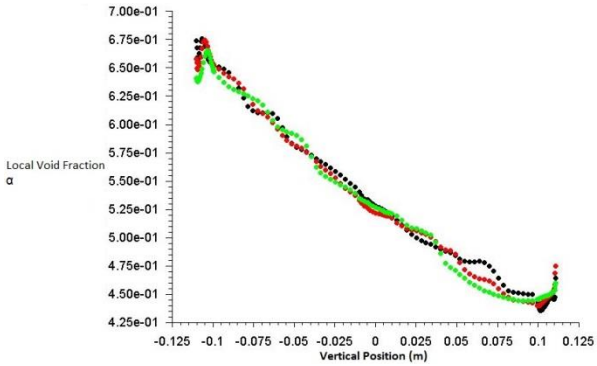

Figure 5.32: 5 g/s void fraction distribution.

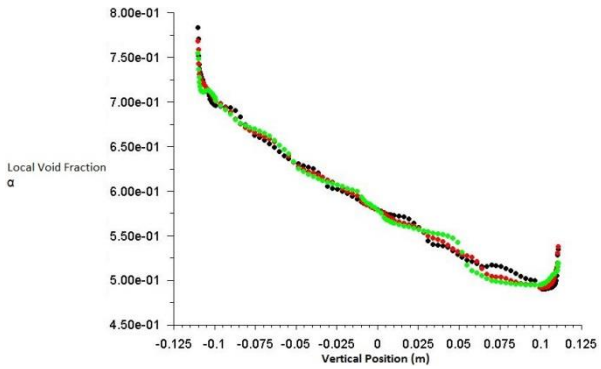

Figure 5.33: 6 g/s void fraction distribution.

Figures 5.27 to 5.33 show that the void fraction in the frontal volume follows a similar pattern for all simulated mass flow rates; the void fraction rises fairly linearly with height, albeit with some end effects which vary. Furthermore, the void fraction does not significantly vary with the color of the dots, which represents along which line from figure 5.1 the plot is made. The three different lines lie in a x,y-plane and run in the x-direction (the vertical direction), as can be seen in figure 5.1. The variation in the y-coordinate, which is the coordinate parallel to the neutron beam, is what sets the lines apart. Thus, the void fraction in the frontal volume does not vary significantly with the y-coordinate. The figures in Appendix D show that the void fraction does not vary significantly with the z-coordinate either, which implies that the local void fraction in the frontal volume only depends on the x-coordinate (the height).

Furthermore, all of the figures shown above show a fairly high void fraction in the frontal volume; the lowest value observed is 43% void at the bottom of the frontal volume for a flow rate of 6 g/s, triple the mass flow rate that was specified by KHC. At 2 g/s, the void fraction is above 70% in the entire frontal volume. As high void fractions are undesirable with respect to neutron moderation, this is an issue that needs to be addressed in the design process.

When looking at the vertical axes of these plots, it can be seen that the range over which the void fraction varies increases greatly with the mass flow rate; whereas the void fraction varies between 85% and 94% for a mass flow rate of 1 g/s, it varies between 43% and 68% for a mass flow rate of 6 g/s. this is the main difference between the void fraction distribution plots shown in figures 5.27 to 5.33.

5.2.4 Vapor Production

This subsection is devoted to presenting a hypothesis on the mechanisms responsible for the vapor production in the simulations performed in this thesis.

Superheated Gas

In the evaporation-condensation model, superheated gas is allowed to exist alongside the liquid phase. The large increase of the variation in the local void fraction with height is possibly caused by the gas absorbing energy, becoming superheated. The volumetric heat source used to model the neutron heat load on the hydrogen does not take into account that physical hydrogen gas absorbs less heat from neutron moderation than liquid hydrogen.

Rather, there is a constant volumetric heat source applied to the entire frontal volume, which deposits a specified heat power per unit volume into the frontal volume of the moderator cell (units Wm^{-3}, see table 4.1).

The simulations indicate that superheated gas is present, since the average mixture temperature in the moderator cell is 26 K for TP2 with 1 g/s mass flow rate and 22.5 K for TP2 with 6 g/s mass flow rate. Both values are well above the saturation temperature, which is 21.7 K.

If much gas is present in a certain area of the frontal volume, much heat will be absorbed by the gas, leaving little heat available to evaporate liquid hydrogen. Equations 5.6 and 5.7 describe this effect, where Q_{total}''' is the total volumetric heat load as specified in the model, Q_{liquid}''' is the volumetric heat load absorbed in the liquid phase and Q_{gas}''' is the volumetric heat load absorbed in the gaseous phase, all in units Wm^{-3}. The local void fraction is denoted as α.

$$Q_{total}''' = Q_{liquid}''' + Q_{gas}''' = (1-\alpha)Q_{total}''' + \alpha Q_{total}''' \quad (5.6)$$

$$Q_{liquid}''' = (1-\alpha)Q_{total}''' \quad (5.7)$$

Equation 5.6 shows how the volumetric heat load is distributed between the phases within each grid cell, while equation 5.7 shows the volumetric heat load absorbed into the liquid phase. This equation shows that an increase in the void fraction α results in a decrease in Q_{liquid}'''. This situation is physically incorrect, since the heat load on the hydrogen stems from neutron moderation and thus should be a function of the hydrogen density. Therefore, the physical total volumetric heat load depends on the density as well, rather than being constant as is the case in the model used in this simulation.

Both equations 5.6 and 5.7 retain their validity with respect to the model when they are averaged over a volume. The liquid phase will, however, absorb heat transferred from superheated gas. This heat can in turn be used to evaporate the liquid. This process takes time, because of the nonzero heat resistance in heat transfer between the phases. Therefore, production of superheated vapor moves evaporation downstream from the frontal volume, which is where the heat is absorbed into the flow domain.

Vapor Production Distribution

Because of heat absorption by superheating gas, the vapor production in high void areas is less, because there is less heat available for evaporation; part of the heat is used to superheat the gas. If, as argued above, less gas is produced in high void areas, it follows that the vapor production in the frontal volume will be less for low mass flow rates. The reason is that simulations with lower mass flow rates have larger average void fractions in the frontal volume (see table 5.3 and figure 5.26).

Since the inlet and outlet of the moderator cell are very close to each other, the superheated outflowing gas meets the inflowing liquid hydrogen near the cell outlet. Here, the superheated gas heats the inflowing fluid. Because the incoming liquid is at near saturation condition, it starts to boil almost instantly upon entering the moderator cell.

If more superheated gas is produced, more liquid hydrogen will start to boil immediately upon entering the moderator cell. This increases vapor production outside the frontal volume. However, the vapor production inside the frontal volume is diminished by the production of superheated gas, as has been outlined above.

Because the mass flow is changed while the heat source is not, the temperature gradient around the inlet and exit is lower for larger mass flow rates, decreasing the transfer of heat from outgoing fluid to incoming fluid. Note that, if the system is fully saturated, the temperature in the moderator cell is equal to the saturation temperature everywhere. In the evaporation/condensation model, however, superheated gas and liquid are allowed to exist, so the temperature can deviate from the saturation temperature, even at a void fraction between 0 and 1.

Also, the velocity magnitudes around inlet and outlet are higher because of the higher mass flow rate, further diminishing the increase in specific enthalpy in the incoming fluid, as the incoming fluid spends less time in thermal contact with the outgoing fluid. Therefore, vapor production near the

inlet of the moderator cell by thermal contact of the incoming liquid with the outflowing fluid is diminished with an increase in mass flow rate.

The hypothesis given above explains why the void fraction at the bottom of the frontal volume is so high for low mass flow rates and drops off as the mass flow rate is increased; for low mass flow rates, much of the hydrogen has already evaporated by thermal contact with outflowing fluid before it even enters the frontal volume.

Superheated Liquid

From the above, it might be concluded that, when lowering the mass flow rate, less vapor is produced in the frontal volume but more vapor is produced in the rest of the moderator cell. Figure 3.4 highlights the frontal volume, the other visible parts of the moderator cell are denoted as 'the rest of the moderator cell'.

However, the described effect is weakened by the effect that superheated liquid hydrogen may exist in to the evaporation-condensation model, due to the finite value of K_{evap}. Thus, upon absorption of heat by the liquid phase, not all of the liquid that reaches the saturation temperature will evaporate immediately. Rather, part of the liquid will evaporate while the rest is superheated. Evaporation of this superheated liquid may ensue further downstream, governed by equation 4.23.

Because liquid hydrogen has a much higher specific heat than gaseous hydrogen (Appendix A), it can absorb a lot more heat at a given rise in temperature. This tends to lower the local vapor production rate as the local void fraction drops, because a lower void fraction means more superheating liquid hydrogen is present, absorbing heat which is not directly used for evaporation. Equation 5.8 describes this effect, while assuming the liquid is already at saturation temperature. Q_{evap}''' is the volumetric heat load used to evaporate hydrogen while $Q_{superheat}'''$ is the volumetric heat load used to superheat liquid hydrogen. If the liquid is below saturation temperature, an extra term would appear on the right hand side of equation 5.8 to account for heating the liquid up to saturation temperature.

$$Q_{liquid}''' = Q_{evap}''' + Q_{superheat}''' \tag{5.8}$$

With

$$Q_{evap}''' = \dot{m}_{l\to g} * h_{evap} = K_{evap} * (1-\alpha)\rho_l \frac{T_l - T_{sat}}{T_{sat}} * h_{evap} \tag{5.9}$$

where equation 4.23 is used. The evaporation enthalpy (or latent heat) is denoted as h_{evap}. In equation 5.8, the ratio between Q_{evap}''' and $Q_{superheat}'''$ is governed by the evaporation frequency K_{evap}, where a larger K_{evap} decreases $Q_{superheat}'''$ with respect to Q_{evap}'''. Lowering K_{evap} lowers the evaporative mass transfer, as can be seen in equation 4.23. This 'slows down' evaporation, moving part of the evaporation downstream. This is analogous to the effect of the superheated vapor, as discussed above.

In short, superheating of any of the phases moves vapor production downstream from the area of heat absorption, since this process stores heat which can later be used in the evaporation process. Superheating also reduces the total vapor production, since the fluid leaving the moderator cell can still contain superheated gas and/or liquid.

Inlet Temperature

In the model, the liquid hydrogen enters the moderator cell slightly under saturation temperature (0.2 K), which has not been taken into account yet in equations 5.8 and 5.9. The hydrogen needs to be heated up to saturation temperature before it can possibly evaporate. Increasing the flow rate increases this requirement for heat. In other words, the increased influx of liquid hydrogen cools the moderator cell. This further decreases the vapor production, since it takes away heat which is not available for evaporation.

Net Effect

The effects discussed above would theoretically tend to lower the vapor production rate when increasing the mass flow rate. According to table 5.4, the combination of all effects discussed in this section result in a local maximum in the total vapor production as a function of the mass flow rate, which lies around a mass flow rate of 2 g/s. Note that the vapor production is significantly smaller than the mass flow rate in all cases and also much lower than the maximum vapor production calculated in section 3.1.

mass flow rate (g/s)	vapor production rate (g/s)		
	frontal volume	rest of moderator cell	total
1	0.20	0.17	0.37
1.5	0.21	0.13	0.38
2	0.21	0.17	0.39
3	0.21	0.17	0.38
4	0.20	0.17	0.37
5	0.19	0.17	0.36
6	0.18	0.17	0.35

Table 5.4: vapor production in the moderator cell for TP2, as calculated by Fluent after running the simulations. The frontal volume is highlighted in figure 3.4, while the other visible parts in that figure are denoted as 'the rest of the moderator cell. Note that the vapor production rate is significantly smaller than the mass flow rate and much lower than the maximum value which was calculated in equation 3.5 for the RID heat load estimate. The latter observation indicates that a large portion of the heat is removed from the moderator cell in the form of superheated liquid and gas.

It should be noted once more that equations 5.6 and 5.7 are not physically accurate. The effect of the mass flow rate on the vapor production as presented in table 5.4 is therefore not expected to agree with data found in physical systems.

5.2.5 Evaporation/Condensation Frequency Influence on Vapor Production (TP1)

The simulations in TP1 were done for the advanced geometry with vacuum inner cavity, with the KHC heat load estimates, since the RID heat load estimates were not available at the time of the simulations. Therefore, the absolute values of the void fraction do not coincide with those found in simulation TP2. The relation between the void fraction and the evaporation/condensation frequency, however, should not be affected by this.

The mass flow specified is 2 g/s, the values for the evaporation and condensation frequency are kept equal and are chosen at $10s^{-1}$, $1s^{-1}$, $0.1s^{-1}$ (default) and $0.01s^{-1}$. Values outside this range were found to result in numerical instability.

Increasing the values of the evaporation- and condensation frequency (the *K* values from equations 4.23 and 4.24) decreases the amount of superheated liquid and subcooled gas. Since more superheated liquid than subcooled gas is present in the flow studies in this thesis, raising the *K* values should increase vapor production, increasing the void fraction. The average fluid temperature should decrease as well, since more heat is used to evaporate hydrogen. This dependence is visible in equations 4.23 and 4.24, where a higher K_{evap} value gives more evaporation. In this case, the increased evaporation dominates over the increased condensation, because the flow investigated in this thesis includes more evaporation than condensation.

Figure 5.34 shows the average void fraction in the frontal volume as a function of the *K* values. As expected, the void fraction rises with rising *K* values. The reason is that higher *K* values increase evaporation (see equation 4.23) and reduce the amount of superheated liquid (see equation 5.9), while the increased condensation plays a minor role (equation 4.24). Therefore, increasing the *K* values increases the vapor production rate.

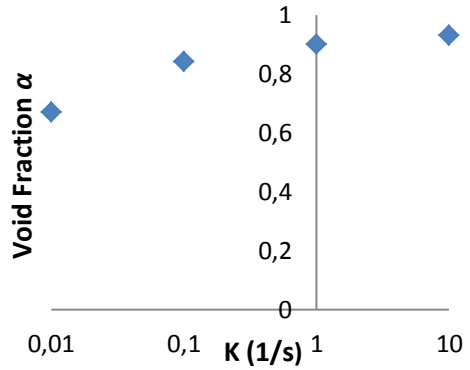

Figure 5.34: average void fraction in the frontal volume for different K values.

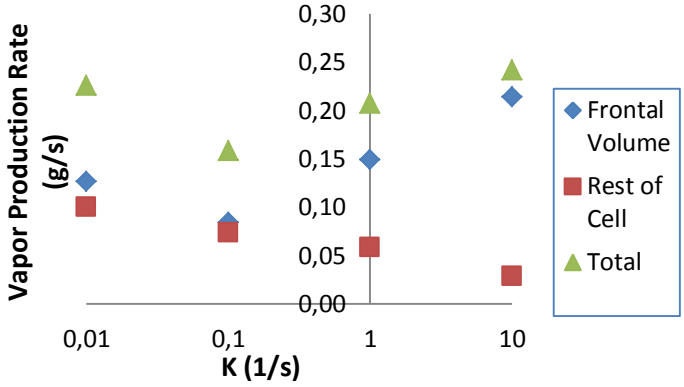

Figure 5.35: vapor production for different evaporation/condensation frequencies. Note the minimum in the vapor production in the frontal volume.

The dependence is not very strong, but a wide range of *K* values is possible [23], which makes it a variable of high significance to the result.

Looking at the vapor production rate in figure 5.35 shows that a minimum exists between the *K* values of $0.01s^{-1}$ and $1s^{-1}$ for the total vapor production in the moderator cell, as a result of a minimum in vapor production in the frontal volume.

Vapor production in the rest of the cell drops as *K* is increased. It is speculated that the following is an explanation for this trend. A lower *K* value induces a lower evaporation rate in the frontal volume (which is where the heat is absorbed into the flow domain), as can be seen in equations 4.23 and 5.7. Less evaporation induces more superheated gas and liquid, since the total heat load in the frontal volume is fixed. This superheated gas and liquid then cause liquid to evaporate in the rest of the moderator cell; the superheated gas by transferring heat to the liquid phase and the superheated liquid by evaporating itself. This assumed to cause the trend of the red squares in figure 5.35.

The minimum in the vapor production in the frontal volume is likely due to competition between two effects. Increasing K_{evap} tends to increase the evaporation rate, as equation 4.23 shows. However, decreasing the K value also decreases the average void fraction in the frontal volume, as figure 5.34 demonstrates; the figure shows a fairly large decrease in the average void fraction if the K values are lowered from $0.1s^{-1}$ to $0.01s^{-1}$.

A decrease in the void fraction increases the heat load from neutron moderation on the liquid hydrogen, as can be seen from equation 5.7. This increase in the heat load on liquid hydrogen tends to increase evaporation. Furthermore, equation 4.23 also shows that the evaporative mass transfer increases with an increase in the liquid volume fraction. It is hypothesized that these effects dominate over the effect of a decrease in K_{evap} at very low K values. Since this argument depends on equation 5.7, which is not physically accurate, the relation shown in figure 5.35 is not expected to represent physical reality.

5.3 Comparison with another Cold Neutron Source

To check whether the obtained results are reasonable, they are compared to results obtained in an experimental study at NIST [24]. This study showed a mass flow rate that was six times higher than the vapor production rate, which is comparable to what is achieved in the simulations in this thesis. The mass flow in their design turns out much higher than 2 g/s, at about 10 g/s at the heat load estimate done by RID (325 W).

For the KHC heat load estimate, the mass flow would be about the same, since a maximum exists in the mass flow as a function of the heat load in the NIST calculations (see figure 5.36) [24]. These calculations were performed for the geometry shown in figure 5.37, which shows a cross section of the entire system. The moderator cell itself is a spherical annulus, with an inner cavity, which is filled by hydrogen gas in steady state. The difference in radius between the inner and outer spherical shells in the NIST design is 20 mm (140 mm and 160 mm inner and outer radius, respectively). The curvature of the spherical chamber makes the average hydrogen thickness to be traversed by the neutrons somewhat larger than 20 mm, which makes it of comparable size to the thickness of the hydrogen layer in the KHC design, which is 25 mm thick.

A difference between this setup and the KHC design is that the condenser is 2.0 meters above the moderator cell, rather than 3.0 meters. This decreases the hydrostatic pressure difference between inlet and outlet at a given density difference between the riser and down comer, reducing the force that drives the flow. Another difference is that the NIST setup is smaller than the KHC design; where the KHC design has an almost cylindrical slab as a frontal volume that is 22.1 cm in diameter (Appendix A), the diameter of the outer sphere in the NIST setup is only 16 cm [25].

An interesting observation that is made, is that thermosiphons often exhibit oscillatory behavior, dependent on operating conditions and geometry [26]. The cause for these oscillations is that effects which balance each other in steady state do not necessarily react to flow changes within the same timeframe. Furthermore, overshooting may occur. This induces oscillations from by small perturbations, possibly increasing in amplitude [27]. For instance, an increase in the mass flow rate would increase friction immediately but reduce the hydrostatic pressure difference only after the riser is fully refreshed with lower void fluid. A temporary increase in cooling capacity could induce this, as more hydrogen is condensed per second in the condenser, increasing the mass flow rate.

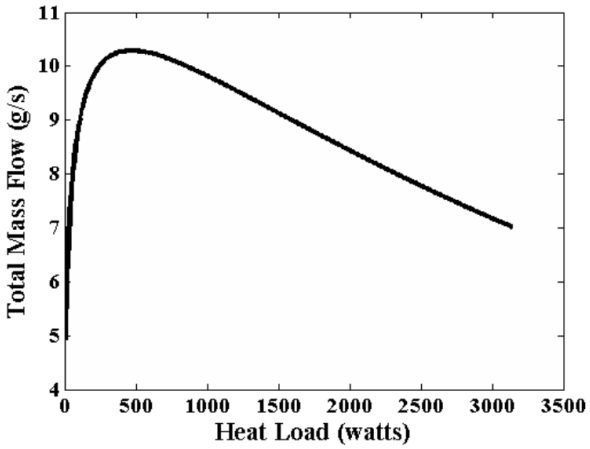

Figure 5.36: NIST mass flow dependence on the total heat load [24]. Note the maximum at around 400 W, which would imply that the mass flow rate is about the same for the RID and KHC heat load estimates. This relation, however, is only validated for the geometry used by NIST, so it may not be concluded that the choice of heat load estimate does not influence the equilibrium mass flux in the CNS design as proposed by KHC.

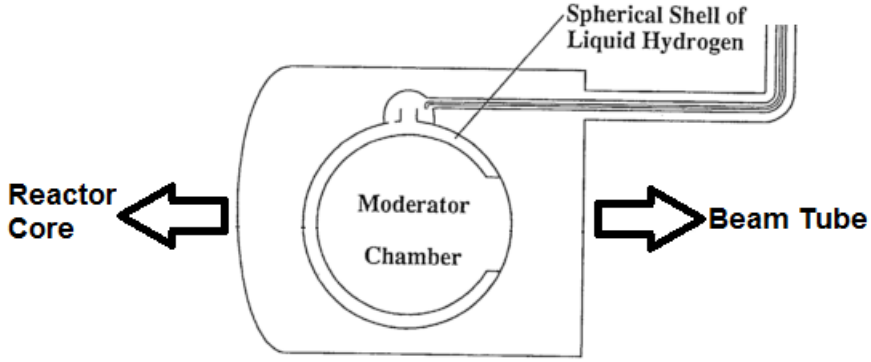

Figure 5.37: NIST Cold moderator cell cross section. The moderator cell is a spherical annulus with a gas filled inner cavity. The hydrogen supply and removal is also done by a pair of concentric tubes. The small dome that can be seen on the top of the moderator cell serves as a gas-liquid separator, to decrease the liquid fraction in the outflow [25].

The NIST setup proved to be difficult to operate stably [25]. Flow instability is a possible explanation for the lack of a converged solution in this thesis, since the steady state solving approach might not work properly for a flow which is unstable. The latter study also recommends that the inlet tube is placed at the bottom of the cell, rather than at the top near the exit. This way, the power can increase further without boiling the cell dry. Experiments showed that, for high heat loads, an interface developed, above which only gas was present. Extending the inlet tube to the bottom of the cell shifted this phenomenon to higher heat loads, enhancing stability. During normal operation, no interface is observed, meaning there is two phase flow in the entire cell [14].

6 Conclusion and Recommendations

The first conclusion that can be drawn from the simulations, is that the average void fraction in the cell is fairly large; the average void fraction in the frontal volume is above 50% in all of the two phase simulations. Increasing the mass flow rate proves to be an effective way of reducing the average void fraction in the moderator cell, so in the final design, overall flow resistance is to be reduced to the absolute minimum in order to achieve the highest performance. For example, the velocity plots showed some vortices in the frontal volume. Adapting the design in order to remove these could lower the flow resistance as well.

In the frontal volume, which is where the neutron beam passes through, the void fraction distribution shows to vary almost linearly with the vertical position. Only at the upper and lower extremities, deviation from this trend occurs.

It is observed that increasing mass flow rate decreases the average void fraction in the frontal volume but decreases homogeneity of the void fraction in the frontal volume. Decreasing the mass flow rate has the adverse effect. A low average void fraction is desirable, as this improves neutron moderation, but homogeneity of the void fraction in the frontal volume is desirable as well, since the entire neutron beam is ideally moderated to the same extent. Appendix D shows that the void fraction in the frontal volume does not vary significantly with the horizontal coordinate (i.e. lateral direction), which is desirable with respect to this last aspect.

Increasing the mass flow rate shows to lead to potentially turbulent flow, limiting the reliability of simulations of higher mass flow rates. It is not certain that the physical flow will be laminar, even with the mass flow at 2 g/s, as specified by KHC.

In the following sections, the simulations performed in this thesis will be discussed with regard to their accuracy and the reliability of the outcomes. A section on design improvement suggestions is also included in this chapter (section 6.5). The last section of this chapter is devoted to recommendations for further research (section 6.6).

6.1 Two Phase Flow Regime

Because the void fractions in all two phase simulations are fairly high, the flow regime cannot be accurately described as dispersed. This negatively influences the reliability of the simulation outcomes as this regime is assumed in the multiphase model used (i.e. the mixture model). Therefore, further research using a more advanced multiphase model (the eulerian-eulerian model in Fluent, for example) is recommended.

6.2 Unknown Variables

6.2.1 Evaporation/Condensation Model

The mass transfer model that was used, being the evaporation-condensation model, includes two parameters that are not known: the evaporation and condensation frequencies and the bubble diameter. The former is shown to impact the results to a relevant extent, the influence of the latter has not been investigated in this thesis. To solve this problem, these parameters can be determined experimentally or a more advanced phase transfer model can be used.

The eulerian-eulerian multiphase model available in Fluent allows for a more advanced boiling model, including three specific wall boiling models. However, these models require significantly more computational resources than the models used in this thesis.

6.2.2 Hydrogen Inlet Temperature

Another unknown parameter is the hydrogen inlet temperature. This parameter influences the amount of vapor in the moderator cell, because a lower inlet temperature would mean the hydrogen needs to absorb more heat in order to reach saturation temperature, lowering vapor production. Because the latent heat is very large in comparison to the specific heat of liquid hydrogen, however, this effect will not be large for small deviations in inlet temperature.

6.3 Model Limitations

6.3.1 Mesh

The program and models used have some limitations, which influences the results. The mesh used was only about 510k cells, because a mesh larger than 512k was not allowed on the available license. A finer mesh generally gives a more accurate solution, and it could have improved the convergence of the solution because the grid cells can be made smaller in a larger mesh.

6.3.2 Slip Velocity

The computational model did not calculate a relative velocity between the liquid and gaseous phases, which is detrimental to the realism of the solution. In reality, the bubbles should rise in the liquid as a result of buoyancy effects.

This effect slows down the gas that is trying to leave the moderator cell, increasing the overall void fraction in the cell and decreasing the gas fraction in the output flow.

Incorporating slip velocity is therefore expected to decrease the average void fraction in the cell and increase the difference in local void fraction between different regions of the cell, as the gas is less restrained from moving upwards. A true phase separation would, given the right flow conditions, be possible.

6.3.4 Turbulence

The Reynolds numbers for all simulations are fairly high (see section 5.2.2), which implies turbulent flow is likely to occur in a physical system. Furthermore, bubbles rising through a liquid may induce turbulence as well, although this effect is not modeled in the simulations in this thesis.

As the Reynolds number analysis in the first part of section 5.2.2 indicates, the flow is not fully resolved; the Kolmogorov length scale is well below the size of the mesh grid cells in all two phase simulations. This shows that turbulence modeling is indeed necessary in order to accurately model the flow.

Enabling turbulence not only influences the flow velocity field, but the heat transfer as well. Turbulence greatly increases heat transport perpendicular to the flow, which especially affects transfer of heat from the walls. This effect would cause the local temperature variations of the mixture to decrease.

6.3.5 Heat Load

In the simulations performed in this thesis, all heat loads were assumed homogenous. This is not entirely realistic, because the local volumetric and surface heat loads depend on local flow conditions.

Volumetric Heat Load

The nuclear heat load density on the hydrogen originates from neutrons colliding with hydrogen nuclei, transferring momentum. Therefore, the volumetric heat load on the hydrogen depends on the (number) density of the hydrogen, which sharply depends on the void fraction.

This is a stabilizing effect, as the volumetric heat load is lowered as the average void fraction in the frontal volume is raised. Incorporating this effect would decrease the volumetric heat source in regions with high void fractions, decreasing the amount of superheated gas produced.

Surface Heat Load

The heat load from the aluminum surface is not modeled fully accurately, since gas bubbles at the wall would cause the local wall temperature to rise as the thermal conductivity of hydrogen vapor is much lower than for liquid hydrogen (see Appendix A). The heat load from the walls is thus a function of the effective thermal conductivity of the two phase mixture and the wall temperature, where the latter is a time-integral function depending on the history of heat removal from the wall, which depends on the history of the hydrogen temperature and the effective thermal conductivity at the wall. Modeling the latter effect would require incorporating the solid wall area into the model, greatly increasing the complexity of the simulation.

Heat Load Distribution

The heat load distribution between the heat load on the front and back walls of the frontal volume is estimated in this thesis. The actual distribution could be different, possibly even depending on operating conditions and wall temperature.

Changing this heat load distribution may influence the vapor production distribution within the frontal volume, as the amount of vapor produced at a wall depends on the heat load of said wall. This is not likely to have an effect on the neutron moderation, since the vapor production only shifts in the direction of the neutron beam as both walls are perpendicular to the neutron beam.

The velocity field in the frontal volume may change as well, because the density of fluid along a wall decreases as it absorbs more heat. If the heat load on one of the walls is much greater than on the other, the difference in buoyancy along the walls might become large enough to induce additional vortices, as the fluid rises much faster along one wall than along the other. This effect might increase the flow resistance.

6.3.6 Geometry

As outlined in chapter 3, the geometry is simplified in the simulations performed in this thesis. This simplification shows in the lack of rounding of the edges, especially in the frontal volume. This can be seen when comparing figures 2.1 and 3.2.

Rounding of the edges could remove the vortices discussed in section 5.2.1 (figures 5.11 to 5.16), which changes the velocity field, possibly decreasing flow resistance in the moderator cell.

6.4 Numerical Convergence

It is observed that no converged solution is achieved in the simulations performed in this thesis. This is seen in the oscillating residuals and other convergence criteria, as well as the comparison of figures 5.20 and 5.25. these figures show that the flow changes with additional iterations, indicating that the solution is not converged. This has a negative influence on the reliability of the simulation results.

6.4.1 Flow Stability

It is not certain that a stable physical solution is available, even though the flow is assumed to be stationary in the simulations performed in this thesis. This could explain why the residuals keep oscillating, as the system constantly vibrates between two solutions.

6.4.2 Mesh

Another possibility for the lack of a converged solution is the relatively coarse mesh in combination with the fairly complex geometry. A finer mesh can more accurately describe the flow as the flow variables change less within each mesh grid cell, rendering a smoother solution. It is possible that the mesh is too coarse to describe a physically accurate solution.

6.4.3 Physics

Convergence can also be limited by the physical models used. If these do not accurately describe the flow, a physical solution cannot be achieved and numerical instability may ensue. As has been mentioned above, a flow with the void fractions observed is not accurately modeled by the mixture model.

6.5 Design Improvement Suggestions

6.5.1 Inlet Position

As suggested by NIST [25], the inlet could be moved towards the bottom of the cell in order to enhance flow stability and decrease the risk of boiling the cell dry. This would, however, increase the complexity of the construction itself, especially with regard to the vacuum shell and the cooling requirement of the whole system.

6.5.2 System Pressure

An ongoing discussion at RID is the possibility to increase the system pressure from 1.5 bar to 2.0 bar. This increases the boiling point of hydrogen by about 1 K [9], slightly lowering the required cooling effort as it is easier to cool at higher temperatures. With the same condenser setup, more cooling power can be delivered at this higher temperature, so the difference between the inlet temperature and the saturation temperature and/or the mass flow rate can be increased. This could decrease the void fraction throughout the cell.

The vapor density at saturation is also increased by this measure, from about 1.9 kgm^{-3} to about 2.5 kgm^{-3}. The liquid hydrogen density decreases from about 69 kgm^{-3} to about 68 kgm^{-3}[9]. This tends to decrease the driving force, since the density difference between liquid and gaseous hydrogen is reduced. This effects tends to reduce the mass flow rate, but it is expected this effect will be smaller than the cooling advantages.

A higher pressure also needs a stronger container to contain the pressure. Since the moderator cell in enclosed by a vacuum layer and the inner cavity is vacuum as well, the inner and outer moderator

cell shells both need to withstand the full hydrogen pressure. This pressure is increased by a factor of one third.

A stronger moderator cell will likely contain more aluminum, increasing the total nuclear heat load on said aluminum. As all of this heat needs to be removed by the hydrogen flow, the total heat source to the hydrogen will increase as a result. This effect tends to increase the average void fraction in the moderator cell.

Taking all effects of an increase in the system pressure into account, further research to determine the advantage of such a measure is recommended. It is quite possible that an optimum pressure can be found, where the combination of the effects discussed above gives the most favorable result, which is the lowest possible average void fraction in the moderator cell, especially in the frontal volume.

Increasing the pressure even further could permit the use of supercritical hydrogen, which has no phase change between gaseous and liquid. This would require a significantly higher pressure and temperature, however (12.8 bar and 33.3 K, [9]) greatly increasing the required strength of the moderator cell.

6.5.3 Gamma Shielding

Including a radiation shield between the reactor core and the moderator cell could reduce the heat load on the hydrogen, lowering the vapor generation rate and presumably the average void fraction in the moderator cell. It is important that this shield allows neutrons to pass while stopping gamma radiation, so the intensity of the neutron beam is not diminished. This measure reduces the heat load on the aluminum of the moderator cell, reducing the surface heat load on the hydrogen. Note that the heat load absorbed by the aluminum is about half of the total heat load (see table 3.1), so the implementation of such a measure could be very favorable.

The shielding material should have a low neutron absorption cross section with a large gamma absorption cross section. Lead is fairly common in radiation shielding and it would be a good, cheap material to use in such a barrier. It has a neutron absorption cross section of 0.171 barn at a neutron velocity of 2.2 km/s (the velocity of thermal neutrons), which is averaged over all known isotopes. The most abundant isotope, 208-Pb (which is also the heaviest), has a neutron cross section of only 0.00048 barn at this neutron velocity [28].

6.6 Further Research

6.6.1 Numerical Research

Model Limitations

Further numerical research should be aimed at reducing the model limitations as discussed in section 6.3. More advanced simulations could include performing simulations including turbulence and slip velocity and using a finer mesh with more grid cells. This is expected to make a large difference in the physical realism of the solution. If, in this simulation, the void fractions achieved remain high, a more advanced multiphase model that can handle this better than the mixture model can be used. Adding the curvature of the frontal volume into the simulation is expected to influence the velocity field, but the void fraction distribution is not expected to vary greatly as a result.

The volumetric heat load may be modeled as a density dependent function, in order to correct for the lower neutron moderation in hydrogen gas. To get a more accurate modeling of the wall heat flux would require more effort, as this would require incorporating the wall itself into the simulation (see section 6.3.5). the impact of modeling the surface heat load to more detail is not expected to be very large.

Flow Domain

To gain most insight in the flow, the entire flow domain can be modeled, including the riser, the down comer, and the condenser. This way, the mass flow rate does not need to be specified and the natural convection itself can be simulated. This would require a substantially larger flow domain to be modeled, however, dramatically increasing the demand for computational resources.

6.6.2 Experimental Research

Because computational resources quickly become a limiting factor when performing two phase flow simulations in complex geometries, experimental research may be a viable option. Experiments involving the entire flow domain can be performed to validate the mass flow rate and check the void fraction distribution in the cell. Also, additional measures such as installing pumps or increasing the cooling power can be investigated.

7 References

[1] IAEA, Power Reactor Information System – Reactor Details – Borssele (2015), consulted on 08-07-2015 http://www.iaea.org/PRIS/CountryStatistics/ReactorDetails.aspx?current=423

[2] Groenhof, A.R., TU Delft: Reactorhal en Prof. Marcel de Bruin hal (2015), consulted on 08-07-2015 http://www.tnw.tudelft.nl/samenwerken/faciliteiten/reactor-instituut-delft/oyster/de-techniek/reactorhal

[3] Groenhof, A.R., TU Delft: De techniek en aanpassingen in OYSTER (2015), consulted on 08-07-2015 http://www.tnw.tudelft.nl/samenwerken/faciliteiten/reactor-instituut-delft/oyster/de-techniek/

[4] Hook, J. R., Hall, H. E., *Solid State Physics,* Wiley, Chinchester, 2010

[5] Furrer, A., *Cold Neutron Sources: Prospects and Applications,* Physica Scripta, 93 (1996)

[6] Nowak, E., *On the refractive index for neutrons,* Zeitschrift für Physik B Condensed Matter 49, 1 (1982)

[7] Shultis, J. K., Faw, R. E., *Fundamentals of Nuclear Science and Engineering,* CRC Press, Boca Raton, 2008

[8] Benner, S., Carrigan, M., Ricardo, A.. *Is There a Common Chemical Model for Life in the Universe?,* Elsevier Ltd., Gainesville FL (2004)

[9] National Institute of Standards and Technology (2011): Saturation Properties for Hydrogen, consulted on 08-07-2015 http://webbook.nist.gov/cgi/fluid.cgi?TLow=21&THigh=22&TInc=0.1&Digits=5&ID=C1333740&Action=Load&Type=SatP&TUnit=K&PUnit=MPa&DUnit=kg%2Fm3&HUnit=kJ%2Fmol&WUnit=m%2Fs&VisUnit=Pa*s&STUnit=N%2Fm&RefState=DEF

[10] KAERI Hyundai Consortium, OYSTER Proposal part III Chapter 9, 2014

[11] meeting with KHC at RID, September 25 2014

[12] de Haan, V., email to Goetjaer, R. et al, November 20, 2014

[13] Jansen, L. and Warmoeskerken, M., *Transport Phenomena Data Companion*, VSSD, Delft, 1987

[14] van den Akker, H. and Mudde, R., *Fysische Transportverschijnselen*, VSSD, Delft, 2008

[15] ANSYS Inc., ANSYS 14.5 Help, 2012

[16] Schiller, L., Naumann,Z., *A Drag Coefficient Correlation*, Verein Deutscher Ingenieure 77, 318 (1935)

[17] Manninen, M., Taivassalo, V., Kallo, S., *On the mixture model for multiphase flow*, VTT Publications 288, 1996

[18] Hertz, H., *Ueber die Verdünstung der Flüssigkeiten, insbesondere des Quecksilbers, im Luftleeren Raume*, Ann. Phys. Chem., 17 (1882), pp. 177-200

[19] Knudsen, M., *die maximale Verdämpfungsgeschwindigkeit des Quecksilbers*, Ann. Phys. Chem., 47 (1915), pp. 697-708

[20] Clausius, R. *Ueber die bewegende Kraft der Wärme und die Gesetze, welche sich daraus für die Wármelehre selbst ableiten lassen*, Ann. Phys., 155 (1850), pp. 500-524

[21] Tanasawa., I., *Advances in Condensation Heat Transfer*. Advances in Heat Transfer 21, (1991), pp. 55–139

[22] Todreas, N. E., Kazimi, M. S*., Nuclear Systems I*, Taylor & Francis, New York, (1993), pp. 490

[23] McMurtry, P., The University of Utah: Length and Time Scales in Turbulent Flows (2015) http://www.eng.utah.edu/~mcmurtry/Turbulence/turblt.pdf

[24] Kopetka, P., Williams, R. E. and Rowe, J. M., *NIST Liquid Hydrogen Cold Source*, NIST Internal Report, NISTIR-7352 (2008).

[25] Kopetka, P., Lewis, M., Olson, D., Rowe, J., Siegwarth, J.,Williams, R., *Thermal Hydraulic tests of a liquid hydrogen cold neutron source*, NIST, NISTIR-5026 (1994)

[26] Greif, R., *Natural Circulation Loops*, J. Heat Transfer 110 (1988), pp. 1243-1258

[27] Nayak, A., Vijayan, P., *Flow Instabilities in Boiling Two-Phase Natural Circulation Systems: A Review*, Science and Technology of Nuclear Installations 2008 (2008)

[28] Munter, A., National Institute of Standards and Technology: Neutron Scattering Lengths and Cross Sections (1993), consulted on 08-07-2015 https://www.ncnr.nist.gov/resources/n-lengths/elements/pb.html

Appendix

A Model and Material Properties

The hydrogen material properties are summarized in Table A.1. All material properties used are from the NIST webbook [9].

Table A.2 gives the model properties for the preliminary design and the more advanced design. It should be noted that, for one single phase simulation, the advanced geometry was used with the KHC heat load estimates.

Density liquid hydrogen (kg/m^3)	69,27
Density gaseous hydrogen (kg/m^3)	1,869
Viscosity liquid hydrogen (kg/ms)	0,000012006
Viscosity gaseous hydrogen (kg/ms)	0,000001615
Enthalpy liquid hydrogen (J/mol)	28,098
Enthalpy gaseous hydrogen (J/mol)	917,62
Latent heat (J/mol)	889,522
Standard state enthalpy liquid hydrogen (J/kg)	13937,5
Standard state nthalpy gaseous hydrogen (J/kg)	455168,6508
Specific heat liquid hydrogen (J/molK)	21,315
Specific heat gaseous hydrogen (J/molK)	25,526
Specific heat liquid hydrogen (J/kgK)	10572,91667
Specific heat gaseous hydrogen (J/kgK)	12661,70635
Thermal conductivity liquid hydrogen (W/mK)	0,10505
Thermal conductivity gaseous hydrogen (W/mK)	0,018567
Surface tension (N/m)	0,0017301
Molar mass hydrogen (g/mol)	2,016

Table A.1: material properties for hydrogen.

Design	preliminary	advanced
Inlet tube diameter (m)	0,014	0,016
Outlet tube diameter (m)	0,036	0,04
Pipe length (m)	3	3
Heat load absorbed in hydrogen (W)	250	162,5
Heat load absorbed in moderator cell (W)	291	162,5
Total heat load (W)	541	325
Outer shell length (m)	0,3	0,295
Inner shell length (m)	0,24	0,27
Outer shell diameter (m)	0,221	0,221
Inner shell diameter (m)	0,201	0,199

Table A.2: model properties for the preliminary and advanced designs.

B Momentum Equation Derivation

The momentum equation for two phase flow is the sum of the momentum equations for the phases, weighted for their volume fractions. For single phase flow, the momentum equation for laminar flow has the following form [22]

$$\frac{\partial}{\partial t}(\rho\vec{v}) + \nabla\cdot(\rho\vec{v}\vec{v}) = -\nabla p + \mu\nabla\cdot\left(\nabla\vec{v} + \nabla\left(\vec{v}^{T}\right) - \frac{2}{3}\nabla\cdot\vec{v}I\right) + g\rho$$

Here, ρ is the density of the fluid, $\vec{v}$ is the velocity vector, and g is the gravitational acceleration. The left hand side denotes the momentum change while the right hand side includes the momentum sources. On the left hand side, the first term is the local momentum change, the second term is the convective term. On the right hand side, the first term is the pressure term, the second term is the viscous stress term and the third term is the gravity term. Note that the term $\rho\vec{v}$ equals the mass flux per unit area.

In this Appendix, we will take a closer look at the momentum equation (eq. 4.8)

$$\frac{\partial}{\partial t}(\rho_m\vec{v}_m) + \nabla\cdot(\rho_m\vec{v}_m\vec{v}_m) = -\nabla p + \mu_m\nabla(\overrightarrow{\nabla v}_m + \nabla(\vec{v}_m^{\ T})) + g\rho_m + \vec{F} - \nabla\cdot\left(\sum_{k=1}^{n}\alpha_k\rho_k\overrightarrow{v_{dr,k}}\overrightarrow{v_{dr,k}}\right) \quad \text{(A.1)}$$

In this equations, the following definitions are used

$$\rho_m = \sum_{k=1}^{n}\alpha_k\rho_k \quad \text{(A.2)}$$

For the mixture density and

$$\vec{v}_m = \frac{\sum_{k=1}^{n}\alpha_k\rho_k\vec{v}_k}{\rho_m} \quad \text{(A.3)}$$

For the mixture velocity. The drift velocity of phase k is given as

$$\overrightarrow{v_{dr,k}} = \vec{v}_k - \vec{v}_m \quad \text{(A.4)}$$

When the equations for the mixture density, mixture velocity and drift velocity are inserted in the second term on the left hand side of equation A.1, the expression in the parentheses takes the following form

$$\rho_m\vec{v}_m\vec{v}_m = \rho_m * \frac{\sum_{k=1}^{n}\alpha_k\rho_k\vec{v}_k}{\rho_m} * \frac{\sum_{k=1}^{n}\alpha_k\rho_k\vec{v}_k}{\rho_m} = \frac{\left(\sum_{k=1}^{n}\alpha_k\rho_k\vec{v}_k\right)^2}{\sum_{k=1}^{n}\alpha_k\rho_k} \quad \text{(A.5)}$$

When the same is done for the last term on the right hand side, the following expressions are obtained after various steps of simplification

$$\sum_{k=1}^{n} \alpha_k \rho_k \overrightarrow{v_{dr,k}} \overrightarrow{v_{dr,k}} = \sum_{k=1}^{n} \alpha_k \rho_k \left(\overrightarrow{v_k} - \overrightarrow{v_m} \right)^2 = \sum_{k=1}^{n} \alpha_k \rho_k \left({v_k}^2 + {v_m}^2 - 2 v_k v_m \right) \tag{A.6}$$

$$\sum_{k=1}^{n} \alpha_k \rho_k \overrightarrow{v_{dr,k}} \overrightarrow{v_{dr,k}} = \sum_{k=1}^{n} \alpha_k \rho_k \vec{v}_k^{\,2} + \sum_{k=1}^{n} \alpha_k \rho_k * \left(\frac{\sum_{k=1}^{n} \alpha_k \rho_k \vec{v}_k}{\sum_{k=1}^{n} \alpha_k \rho_k} \right)^2 - 2 \sum_{k=1}^{n} \alpha_k \rho_k v_k * \frac{\sum_{k=1}^{n} \alpha_k \rho_k \vec{v}_k}{\sum_{k=1}^{n} \alpha_k \rho_k} \tag{A.7}$$

$$\sum_{k=1}^{n} \alpha_k \rho_k \overrightarrow{v_{dr,k}} \overrightarrow{v_{dr,k}} = \sum_{k=1}^{n} \alpha_k \rho_k \vec{v}_k^{\,2} + \frac{\left(\sum_{k=1}^{n} \alpha_k \rho_k \vec{v}_k \right)^2}{\sum_{k=1}^{n} \alpha_k \rho_k} - 2 \frac{\left(\sum_{k=1}^{n} \alpha_k \rho_k \vec{v}_k \right)^2}{\sum_{k=1}^{n} \alpha_k \rho_k} \tag{A.8}$$

$$\sum_{k=1}^{n} \alpha_k \rho_k \overrightarrow{v_{dr,k}} \overrightarrow{v_{dr,k}} = \sum_{k=1}^{n} \alpha_k \rho_k \vec{v}_k^{\,2} - \frac{\left(\sum_{k=1}^{n} \alpha_k \rho_k \vec{v}_k \right)^2}{\sum_{k=1}^{n} \alpha_k \rho_k} = \sum_{k=1}^{n} \alpha_k \rho_k \vec{v}_k^{\,2} - \frac{\left(\sum_{k=1}^{n} \alpha_k \rho_k \vec{v}_k \right)^2}{\rho_m} \tag{A.9}$$

It should be noted that the last term of equation A.9 is the same as the last term in equation A.5. Thus, when the values of equations A.5 and A.9 are inserted into equation A.1, and the terms from equation A.9 are moved to the left hand side, equation A.10 is obtained. Note that the nabla operator ∇ is linear, so there is no loss in accuracy because we left it out of equations A.5 to A.9.

$$\frac{\partial}{\partial t} (\rho_m \vec{v}_m) + \nabla \cdot \left(\sum_{k=1}^{n} \alpha_k \rho_k \vec{v}_k^{\,2} \right) = -\nabla p + \mu_m \nabla (\overrightarrow{\nabla v_m} + \nabla (\vec{v}_m^{\,T})) + g \rho_m \tag{A.10}$$

Equation A.10, in turn, is in the same form as in Todreas and Kazimi [22]

In the Fluent theory guide [15], which describes the models underlying the program, the sign of the last term on the right hand side in equations 4.8 and A.1 is reversed; the last term is not subtracted, but added. In the light of the analysis given above, this seems to be a typographical error in the Fluent theory guide. This view is supported by Manninen et al. [17], where derivation of equation A.1, starting from the summation of the momentum balances of the individual phases, can be found.

C Convergence criteria plots

These are the plots for the convergence criteria for TP2 with a flow rate of 2 g/s. They look similar for the other two phase simulations.

C.1 without z-component to inlet velocity

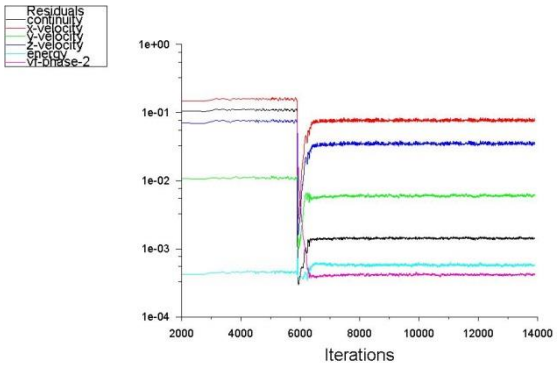

Figure C.1: residual history. The black line is the mass continuity, the red line is the residual of the x-velocity, the green line is the residual of the y-velocity, and the blue line is the residual of the z velocity. The residuals of the energy equation and the void fraction are represented by the light blue and purple lines, respectively.

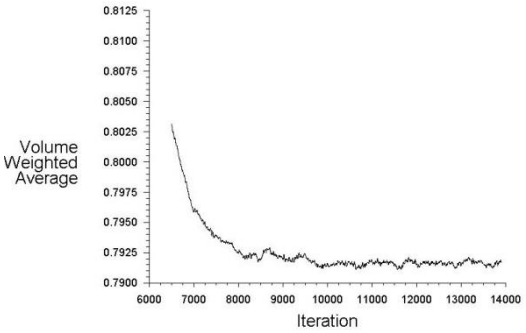

Figure C.2: average void fraction history in the frontal volume.

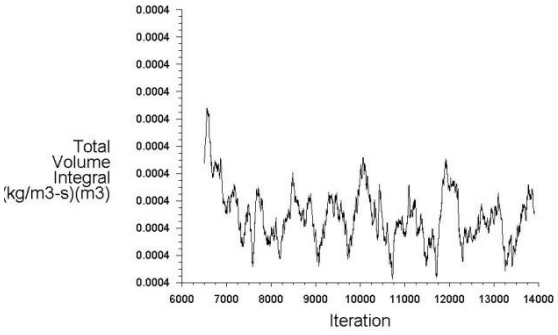

Figure C.3: total vapor production history.

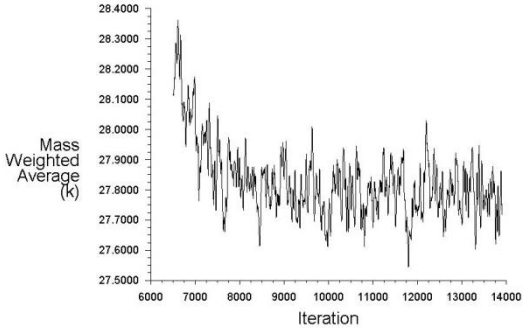

Figure C.4: outlet temperature history.

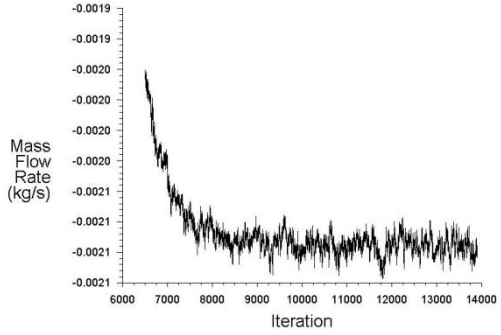

Figure C.5: outlet mass flow history.

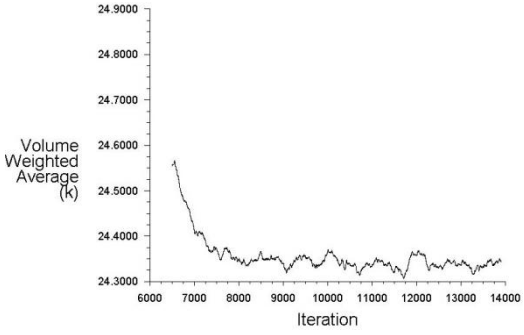

Figure C.6: volume average temperature history of the contents of the moderator cell.

C.2 with z-component to inlet velocity

The plots in this section depict the history of the convergence criteria and the residuals after the inlet velocity was given a z-component in TP2. This is done after iteration 13913 of the 2 g/s case without z-component to the velocity, of which the plots are shown in the previous section. The moment the inlet velocity was changed can be seen as a spike in figure C.7.

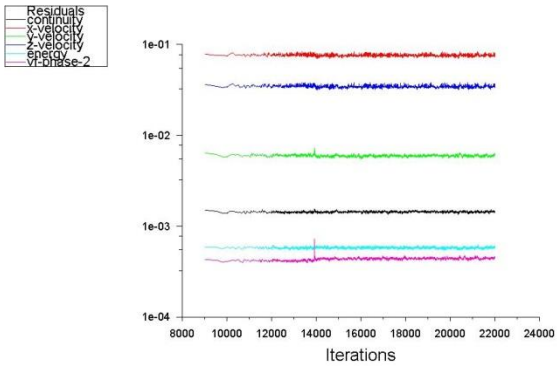

Figure C.7: residual history. The black line is the mass continuity, the red line is the residual of the x-velocity, the green line is the residual of the y-velocity, and the blue line is the residual of the z velocity. The residuals of the energy equation and the void fraction are represented by the light blue and purple lines, respectively.

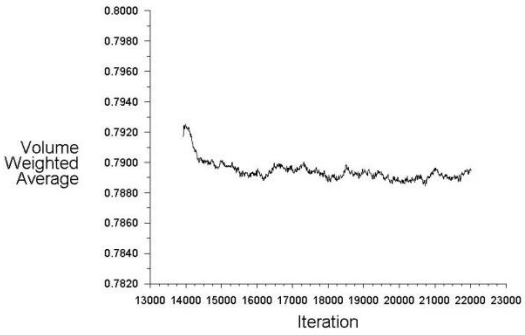

Figure C.8: average void fraction history in the frontal volume.

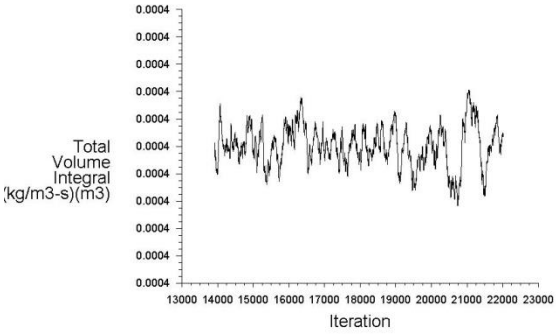

Figure C.9: vapor production history in the moderator cell.

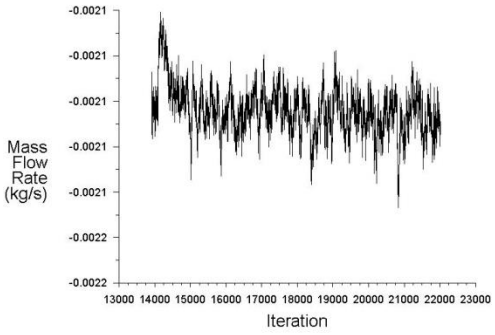

Figure C.10: outlet mass flow history.

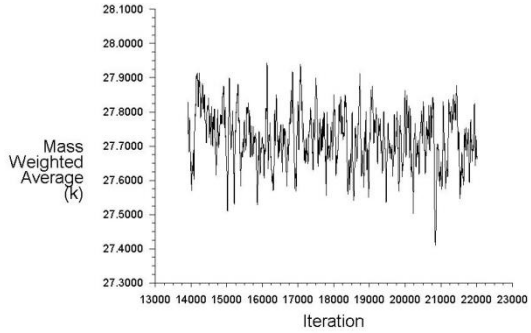

Figure C.11: outlet temperature history.

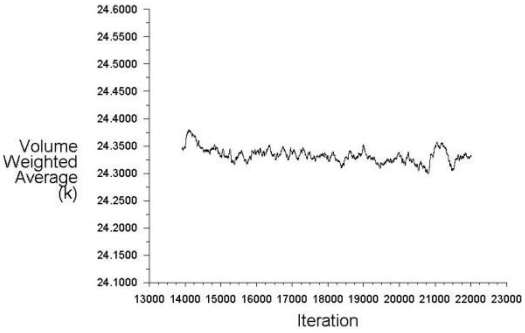

Figure C.12: volume average temperature history of the contents of the moderator cell.

D Void Fraction Distribution for varying z

This Appendix shows the void fraction distributions for the different mass flow inlet conditions used in TP2. The plots are made along lines at fixed y (exactly in the middle between the front and back wall of the frontal volume) and different, equally spaced, z-coordinates.

When looking at the moderator cell from the reactor, the green dots represent the line on the right, the red dots the line through the middle and the black dots represent the line on the left. All lines lie at the same y-coordinate as the middle line of figure 5.1. The horizontal axis shows the position along the line, where the negative extreme is at the top of the moderator cell. The vertical axis shows the local void fraction.

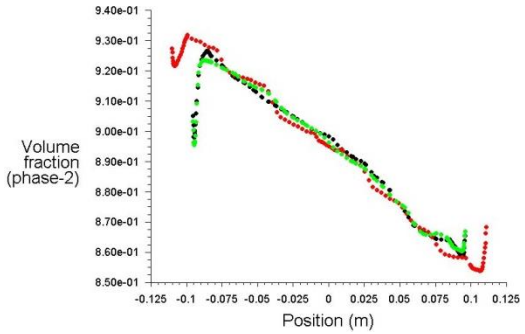

Figure D.1: void fraction distribution for a flow rate of 1 g/s

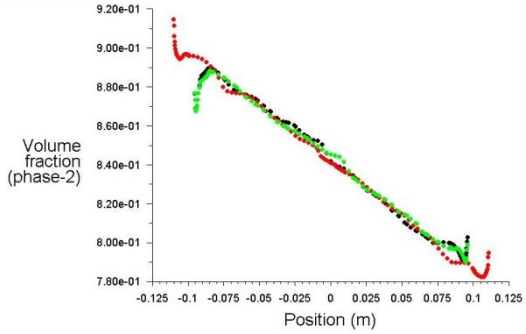

FigureD.2: void fraction distribution for a flow rate of 1.5. g/s.

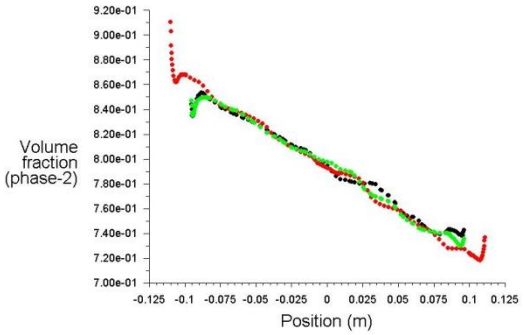

Figure D.3: void fraction distribution for a flow rate of 2 g/s.

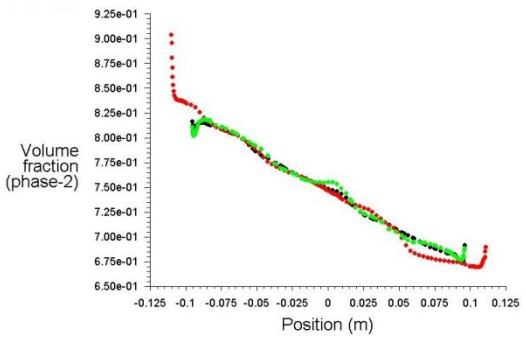

Figure D.4: void fraction distribution for a flow rate of 3 g/s.

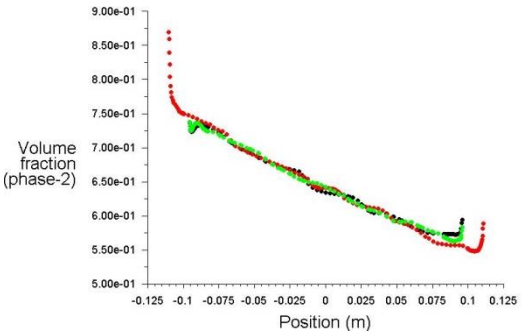

Figure D.5: void fraction distribution for a flow rate of 4 g/s.

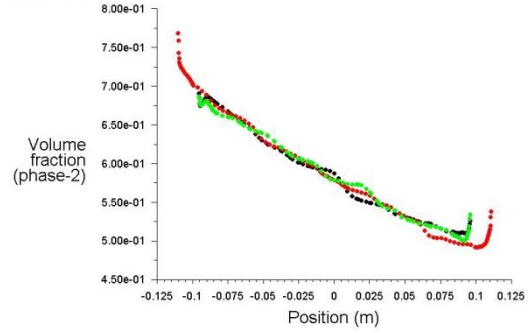

Figure D.6: void fraction distribution for a flow rate of 5 g/s.

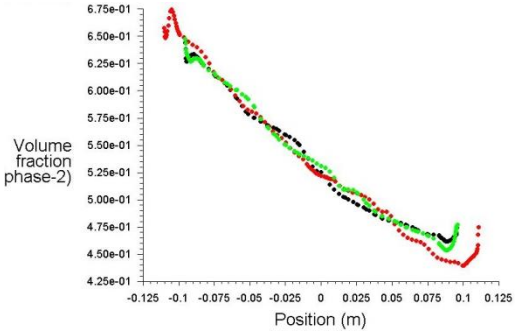

Figure D.7: void fraction distribution for a flow rate of 6 g/s.